

Electron Many-Body Effects in Quantum Point Contacts



**university of
 groningen**

**zernike institute for
 advanced materials**

Zernike Institute PhD thesis series 2012-15

ISSN: 1570-1530

ISBN: 978-90-367-5600-6 (printed version)

ISBN: 978-90-367-5601-3 (electronic version)

The work described in this thesis was performed in the research group Physics of Nanodevices of the Zernike Institute for Advanced Materials at the University of Groningen, the Netherlands. It was supported with funding from a Pakistani HEC-Nuffic scholarship and the Zernike Institute, and did profit from collaboration with projects funded through a Vidi grant from the Netherlands Organization for Scientific Research (NWO) and the national NanoNed and NanoLab NL initiatives.

Thesis front cover: Linear conductance of a Quantum Point Contact as a function of gate voltage, with traces that show a modulation of the 0.7 anomaly as a function of length (186 nm (left trace) to 608 nm (right trace)).

Thesis back cover: Artistic image of a length-tunable Quantum Point Contact (modified from the original SEM image by Thomas Maassen).

Printed by: Ipskamp Drukkers, Enschede

RIJKSUNIVERSITEIT GRONINGEN

Electron Many-Body Effects in Quantum Point Contacts

Proefschrift

ter verkrijging van het doctoraat in de
Wiskunde en Natuurwetenschappen
aan de Rijksuniversiteit Groningen
op gezag van de
Rector Magnificus, dr. E. Sterken,
in het openbaar te verdedigen op
vrijdag 13 juli 2012
om 11:00 uur

door

Muhammad Javaid Iqbal

geboren op 1 januari 1982
te Narowal, Pakistan

Promotor: Prof. dr. ir. C.H. van der Wal

Beoordelingscommissie: Prof. dr. A.D. Wieck
Prof. dr. D.M. Zumbühl
Prof. dr. ir. W.G. van der Wiel

*Dedicated to my (late) father whose memories are still a source of inspiration
for me...*

Contents

1	Introduction	1
1.1	Charge and spin based electronics: from power plants to nanoscience	1
1.2	This work: Quantum Point Contacts	3
1.3	Outline of this thesis	7
2	QPC transport properties, device fabrication and measurement techniques	11
2.1	Introduction	11
2.2	GaAs/AlGaAs heterostructure	11
2.3	Quantum point contact and quantized conductance	12
2.4	The 0.7 anomaly	15
2.5	The Zero-Bias Anomaly (ZBA)	18
2.6	Review of literature on the 0.7 anomaly and ZBA	20
2.7	Device fabrication	29
2.8	Low temperature measurement techniques	34
3	Many-body effects with signs of two-impurity Kondo Physics in QPCs with a fixed length	41
3.1	Introduction	42
3.2	Experimental realization	43
3.3	Part I: Correlations between QPC transport properties and geometry	44
3.4	Part II: Observation of a double-peak ZBA	52
4	Emergent impurity states from many-body physics in clean quantum point contacts	59
4.1	Introduction	60
4.2	Experimental	61
4.3	Results from single split-gate QPCs	61
4.4	Results from length-tunable QPCs	63

4.5	Conclusions	72
4.6	Appendix: Materials and methods	73
4.7	Appendix: Earlier reports showing modulated 0.7 anomalies and double-peak ZBAs	74
4.8	Appendix: Friedel oscillations and Fermi wavelength in the QPC .	76
4.9	Appendix: Analysis of ZBA peak positions at $G = 0.4, 0.6, 0.7$ and $0.85 \cdot (2e^2/h)$	78
5	Split-gate quantum point contacts with tunable channel length	81
5.1	Introduction	82
5.2	Design considerations	84
5.3	Electrostatic simulations	86
5.4	Sample fabrication and measurement techniques	91
5.5	Experimental realization of length-tunable QPCs	92
5.6	Conclusions	95
6	The annealing mechanism of AuGe/Ni/Au ohmic contacts to a two-dimensional electron gas in GaAs/Al_xGa_{1-x}As heterostruc- tures	97
6.1	Introduction	98
6.2	Device fabrication	99
6.3	Electrical measurements	100
6.4	Cross-sectional TEM and EDX imaging	103
6.5	Summary of annealing mechanism	104
6.6	Diffusion model	108
6.7	Contact-shape dependence	110
6.8	Conclusions	113
7	Robust recipe for low-resistance ohmic contacts to a two-dimensional electron gas in a GaAs/AlGaAs heterostructure	117
7.1	Introduction	118
7.2	Experimental details	118
7.3	Device design, measurement schemes and methods	120
7.4	Results and discussions	125
7.5	Conclusions	128
A	Wafer inventory	131
A.1	WSUMI301611	131

A.2	WSUMI301612	131
A.3	WREUT1098	132
A.4	WREUT1588	132
A.5	WREUT12570	133
B	Device fabrication	135
B.1	Alignment markers	135
B.2	Mesa etching	136
B.3	Ohmic contacts	137
B.4	Fine gates	138
B.5	Large gates	139
C	Biased cool down	141
	Summary	145
	Samenvatting	149
	Acknowledgements	153
	Curriculum vitae	157
	List of publications	159

Chapter 1

Introduction

1.1 Charge and spin based electronics: from power plants to nanoscience

The last few decades have been revolutionary for progress in condensed matter physics. The electronic properties of materials revealed very rich and interesting behavior that is fundamental to a wealth of applications in our society. At this stage, there is still a strong interplay between fundamental research in solid state physics and the development of new and improved devices.

Already early in the nineteenth century, scientists discovered how to utilize the electron flow in materials for practical applications. For example, the first commercial electrical power station was opened in San Francisco in 1879, even before the discovery of the electron by J. J. Thomson in 1897. Electrons are fundamental particles that occur as building blocks in atoms. In isolated atoms, the electrons orbit around the nucleus. This can be pictured as having a similarity with the way our home planet Earth and other planets in the solar system revolve around the Sun. For detailed understanding of atoms, however, this analogy breaks down and the states of electrons in atoms can only be understood with quantum mechanical theory where the position of an electron is described by a wavefunction.

The electron is a charged particle. Its charge was first accurately measured by Robert Millikan and Harvey Fletcher in 1909 in their famous oil drop experiments, and has the value -1.602×10^{-19} C. In 1925, the two Dutch physicists George Uhlenbeck and Samuel Goudsmit discovered that the electron also has an intrinsic angular momentum, that has been given the name spin [1]. This can be pictured as having a similarity with the way the Earth revolves around its axis. The

quantum mechanical nature of this spin gives that its value along a particular direction only shows one of two values when it is measured: $+\frac{1}{2}\hbar$ or $-\frac{1}{2}\hbar$ (where \hbar the reduced Planck constant), which are known as spin-up and spin-down, respectively. Since the electron is a charged particle, its spin is directly linked to an intrinsic magnetic moment. This can be viewed as each electron being a tiny magnet with a North and South pole. In a magnetic field this magnetic moment splits the energies of the spin-up and spin-down states, the so-called Zeeman splitting.

The charge and spin properties of the electron are at the heart of nearly all electrically powered devices that we use in our daily life. Most of the devices we are familiar with exploit the charge property of the electron, which causes the electron to move when it is subjected to an external electric field. Amplification and logic operations by cheap and robust electronic devices were made possible by the invention of the transistor by John Bardeen, William Shockley and Walter Brattain at Bell Labs in 1947. This made it possible to build electronic equipment like radio, TV, calculators, computers and is currently of importance for almost all other household and industrial equipment.

The first electronic experiment that was in fact involving the spin of an electron was also carried out before the discovery of the electron and its spin. Already in 1856, William Thomson (more commonly known as Lord Kelvin) discovered the Anisotropic MagnetoResistance (AMR) effect in bulk iron material [2]. The iron material showed a resistance change as a function of the orientation of the material with respect to an external magnetic field. Follow-up research in this direction led many years later, in 1988, to the discovery of the Giant MagnetoResistance (GMR) effect [3, 4]. Also for the GMR effect the spin of the electron has an essential role. This effect appears in the electrical resistance of two adjacent ferromagnetic layers separated by a thin non-magnetic layer. This resistance can be switched to a low (or high) value when the magnetization of the layers is forced in the same (or opposite) direction by an applied external magnetic field. This effect was in recent years applied in the hard-disk read heads of almost all computers [5]. In addition, the discovery of the GMR effect led to the birth of a new research field that is now called spintronics (or spin-electronics) [6, 7]. In 2007, Albert Fert and Peter Grünberg were awarded the Nobel prize for the discovery of the GMR effect.

Many of these developments in electronics became possible thanks to an extremely impressive technological achievement: the ever increasing miniaturization of electronic devices between about 1950 and today (awarded with the Nobel prize

in Physics in the year 2000). This, in turn, allowed for opening up new scientific directions. In particular, between 1980 and 1990 it became possible to investigate electronic devices with very small dimensions, smaller than the length scales of the physical mechanisms that determine the behavior of electron transport. This led to the observation of new physical phenomena with a class of devices known as mesoscopic devices [8]. These devices have properties from which one can directly observe that at these small length scales quantum mechanical effects become important. This research topic is now part of the fields known as nanoscience and nanotechnology, and is still an active area of research with many exciting new developments.

A clear example of this development is the discovery of the quantum dot [9, 10, 11] (for a popular review see [12]), which gave an entirely new dimension to the fields of nano-electronics and spintronics. In this device, also called an artificial atom, a single or a few electrons can be localized and manipulated in a small volume of semiconductor material. With such quantum dots, the electron number can be changed one by one, their interaction to the leads can be tuned via nanoscale tunable openings or tunnel barriers, and the spin of electrons in the dot can be manipulated as well. Since then, physicists are trying to improve the accuracy of spin manipulation in these quantum dots, in order to utilize them as building blocks for a new generation of dream computers known as quantum computers [13, 14, 15, 6].

1.2 This work: Quantum Point Contacts

This PhD thesis presents experimental research on one of the most simple nano-electronic devices: the Quantum Point Contact (QPC). A QPC is nothing more than a nanoscale short and narrow constriction between two large conducting regions (which act as source and drain electron reservoir), see Fig. 1.1. QPCs can be realized (as for this thesis work) as tunable channels in an ultra-clean semiconductor material, where the influence of impurities can be reduced to a very low level and which are materials without magnetic or superconducting interactions. Such QPCs therefore provide the ultimate system for testing the fundamentals of electron transport at the nanoscale. Despite this high level of control over QPCs and its simplicity, it turns out the understanding of its transport properties is far from complete.

In a very large electronic device, where the mean free path of the electrons is much smaller than the length of the device, the electrons move in a random path

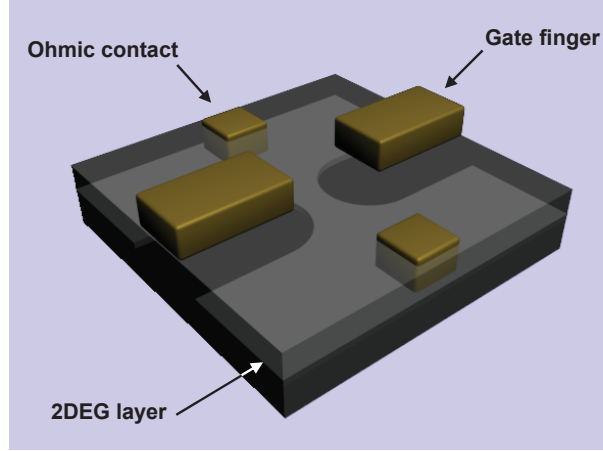


Figure 1.1: Artist impression of a split-gate QPC device. The essential part of the QPC is the tunable narrow constriction in the two-dimensional electron gas (2DEG, light gray layer). This is created by applying a negative voltage to the gate fingers on the wafer surface, which causes depletion of the 2DEG underneath these gates. The device can be connected to measurement electronics by using the ohmic contacts to the 2DEG (picture courtesy of E. J. Koop).

due to many collisions and it is the average motion of electrons that contributes to the current flow. This kind of system is said to have diffusive transport, and the electrical conductance (1/resistance) of a connection is then described by Ohm's law. For QPCs the electron mean free path can be longer than the dimensions of the device and the electrons then pass through the device without any collision. The motion of electrons is then ballistic and the transport properties are different than for diffusive systems. In particular, the transport reflects that QPCs are one-dimensional channels where electrons are in states that behave as propagating waves. These waves can only use a discrete number of modes that fit in the channel, and this results in quantized conductance [16, 17]. Quantized conductance is observed as the tendency of the system to have conductance values G that are an integer N times the conductance quantum, $G = N \cdot G_0$, where the conductance quantum $G_0 = 2e^2/h$ only depends on the fundamental constants e (the electron charge) and h (Planck's constant). In QPCs with a tunable channel width this is observed as a stepwise increase of the conductance when the width of the channel is gradually increased.

QPCs with quantized conductance are thus devices for which a very high level of control and understanding has been achieved, and they are therefore central in many fundamental studies and proposals for future electronic and spintronic

devices. The applications range from charge sensors [18] to electron-spin detectors [19], and QPCs are also considered for quantum information applications [20, 21, 22]. However, QPCs also show features which are generically observed but not yet understood. There is only consensus that these result from electron many-body interactions, and that these effects often have a very significant influence on the QPC conductance. The most famous example is the so-called *0.7 anomaly* [23], which is the tendency of the system to also show a conductance value of $G = 0.7 \cdot G_0$. Despite a large body of work [24] over the last 20 years, there is no complete understanding of these many-body interactions. Better understanding is of importance for a fundamental description of electron quantum transport, and for properly designing the function of QPCs in future nano-electronic devices. The main aim of this thesis work was to further study the basic transport properties of QPCs, with an emphasis on studying the electron many-body effects.

This thesis is divided into two main parts. Part 1 is about the work on transport properties of QPCs. Part 2 is dedicated to research that aimed to improve technological aspects of operating QPCs, and also bears relevance for many similar devices. The focus in this second part is on investigations into so-called ohmic contacts to a two-dimensional electron gas (2DEG) below the surface of a semiconductor. Our QPCs were realized in such a 2DEG layer, and the formation of good quality ohmic contacts is a key step in the fabrication process of all devices based on such a 2DEG.

1.2.1 Research on quantum point contacts

The research with QPCs focussed on the electron many-body effects that occur in these devices. We used devices that were defined in the 2DEG of a GaAs/AlGaAs heterostructure with the so-called split-gate technique (Fig. 1.1). Such QPC devices have two metallic gate fingers on the surface of the wafer (*i.e.* these do not make electrical contact to the 2DEG). Applying a negative voltage to these gate fingers depletes the 2DEG underneath the gates over a range that depends on the gate voltage. Thus, one can induce a narrow constriction in the 2DEG with tunable width.

There are two signatures of many-body effects in the QPC conductance that are often observed, and which were also central in the investigations presented here. These are the *0.7 anomaly* and the *Zero-Bias Anomaly (ZBA)*. It is not yet well established whether they are the result of the same underlying mechanism

[24].

The 0.7 anomaly

As said, the 0.7 anomaly is an extra shoulder that appears in the quantized conductance traces when these are measured as QPC conductance as a function of channel width. A few years after the discovery of quantized conductance in 1988, the work by Thomas *et al.* [23] in 1996 firmly established that the 0.7 anomaly is a conductance feature that is generic and appears in almost all QPCs. This feature is not explainable by the non-interacting electron models for QPC transport, as for example the detailed model for conductance quantization by Büttiker [25].

Thomas *et al.* [23] attributed the anomalous feature to electron many-body physics that gives spontaneous spin polarization. Since then many other theories and experimental efforts have come forward to explain the origin of the anomalous feature but non of these has been conclusive and generally accepted till now. A broadly valid and consistent picture is lacking. A recent extensive scientific review on these developments since 1996 can be found in Ref. [24], while more popular reviews can be found in Refs. [26, 27]. As motivated above here, this puzzle is for several reasons still a highly relevant challenge. In the popular review Ref. [26] prof. Carlo Beenakker is cited characterizing this challenge as the single most important problem in the field of quantum ballistic transport.

The Zero Bias Anomaly (ZBA)

The second intriguing feature associated with the QPC transport properties is called Zero-Bias Anomaly (ZBA). It is an enhanced conductance peak [28] around zero voltage that appears in the QPC conductance as a function of the d.c. source-drain bias voltage across the channel. Also for the ZBA there is consensus that it results from electron many-body interactions [24]. Many properties of the ZBA in QPCs [28] resemble the properties of ZBAs that are observed with quantum dots that have a net single spin [29, 30, 31]. For quantum dots, it is established that such ZBAs are a signature of the Kondo effect (for a good popular review see Ref. [32]). The Kondo effect for quantum dots is the tendency of a localized electron spin near an electron reservoir to get somewhat delocalized (via a mechanism where a dot and reservoir electron with opposite spins get exchanged). This enhances the quantum dot conductance, which appears as the ZBA.

The analogy between ZBAs in QPCs and quantum dots triggered theoretical

investigations into the question whether the many-body effects in QPCs could be related to the formation of localized states in the QPC channel. Detailed numerical calculations that account for all electrostatic screening effects in the QPC channel and for the most relevant electron-electron interactions gave results that showed that such localization is indeed possible [33]. Notably, this localization is purely the result of many-body electron interactions, since the electrostatic potential as felt by individual electrons gives an open system. Such states are therefore called self-consistent localized states or emergent impurity states.

1.2.2 Research on ohmic contacts

All the QPC devices studied in this thesis work were made in the two-dimensional electron gas (2DEG) of a GaAs/AlGaAs heterostructure. Such a 2DEG can be pictured as a two-dimensional sheet with high electrical conductivity (in behavior similar to metals), in a clean semiconductor environment that behaves as an electrical insulator. In these systems the 2DEG is at a depth of typically 100 nm below the wafer surface. For studying the transport properties of devices based on such a 2DEG material, this 2DEG needs to be connected to macroscopic measurement leads via metallic contact pads on the wafer surface. This only becomes functional after a contact pad on the surface gets a low-resistance connection with ohmic properties to the 2DEG below the surface. This part is called the ohmic contact (see Fig. 1.1). Realizing such contacts can be accomplished by depositing a AuGe/Ni/Au stack on the surface (~ 100 nm thick) and then annealing the device structure for a certain time and at some high temperature, such that part of the deposited material diffuses into the wafer. The research on this topic aimed at improving the ability to predict the optimal duration and temperatures for the annealing step, and at obtaining insight in the material changes that occur during annealing. Optimal insight in, and control over ohmic contact fabrication is important because high-quality heterostructures are often only available in a limited quantity. In addition, it is useful that one can select a recipe that minimizes the heating that is needed for annealing the contacts, to avoid damage due to heating at other places in the device structure.

1.3 Outline of this thesis

We thus present work on quantum point contacts and ohmic contacts in this thesis. A chapter-wise description of the work is as follows:

Chapter 2 provides a theoretical background on QPCs. This includes a review of earlier theoretical and experimental work that was carried out in the field, aimed at explaining the origin of the anomalous conductance features of QPCs (0.7 anomaly and ZBA). We also present here the basics of the device fabrication and the measurement techniques that were used for this thesis work.

In *Chapter 3* we review experimental results from studies of the 0.7 anomaly and the ZBAs, that were obtained by our team just before and during the initial phase of this thesis work. The focus is here on comparing different QPC devices for which the length and width of the QPC channel was varied by fabricating them with different dimensions. This presentation includes a report on the initial observations of ZBAs with double-peak character, with an analysis of their temperature and magnetic-field dependence. This work was essential for initiating the later studies of this thesis work with QPCs that have an *in-situ* length-tunable channel for each individual device.

In *Chapter 4*, we report a study of the 0.7 anomaly and ZBA in this new type of QPC with a tunable effective length for the channel. These QPCs were implemented with split-gate QPCs with 6 gate fingers instead of the conventional layout with only 2 gate fingers. Having such *in-situ* length tuning for the QPC channel turned out to be crucial for dealing with, and ruling out an essential role for device imperfections for the observed signatures of electron many-body physics. Such imperfections can exist in the form of atomic impurities, material defects, or small nanofabrication errors. With these devices we discovered that the 0.7 anomaly and the ZBA show periodic behavior as a function of QPC channel length. In addition, this work established that ZBAs with a double peak can occur for clean QPCs (instead of only ZBAs with a single peak), and that the QPC conductance is at such points similar to that of the two-impurity Kondo model. These intriguing results shed new light on the origin of these two highly debated features. These results are interpreted as signatures of Friedel oscillations in the QPC channel, which can develop into the predicted self-consistent localized states in QPCs. The results are analyzed in this framework, with collaboration on new theory work for this topic.

In *Chapter 5*, we present the technological and design aspects of the newly developed QPCs with tunable channel length, and report on the initial characterization.

Part 2 of this thesis on ohmic contacts starts with *Chapter 6*. Ohmic contacts to a two-dimensional electron gas (2DEG) in GaAs/AlGaAs heterostructures were realized by annealing of AuGe/Ni/Au that is deposited on its surface. We

studied how the quality of this type of ohmic contact depends on the annealing time and temperature. For this work annealing took place in a hot nitrogen gas flow in a glass tube furnace. We focussed on the question how the optimal annealing time and temperature change for a different depth of the 2DEG. Combined with transmission electron microscopy and energy-dispersive X-ray spectroscopy studies of the annealed contacts, our results allow for identifying the annealing mechanism and describing a model that can predict optimal annealing parameters for a certain heterostructure.

In the last chapter of this thesis, *Chapter 7*, we report on work aimed at extending the results on ohmic contacts of Chapter 6, while also further improving the ohmic contacts. We had analyzed that measurement of the change in 2DEG resistance under an ohmic contact could provide important additional information. We designed a dedicated device structure for such measurements. These devices were annealed in a rapid thermal annealer (RTA). The results showed that our recipe based on RTA annealing was very robust and nearly always giving very low resistance values for the ohmic contacts. The downside of this was that the resistance values were so low that accurate measurement of their values was not possible, and this prohibited further testing of the model of Chapter 6 and obtaining detailed insight in the change of 2DEG resistance under an ohmic contact. The results are, nevertheless, important for work where low-resistance ohmic contacts are critical, and the analysis of the results was suited for getting insight in the role of spreading resistance inside low-resistance contacts.

Bibliography

- [1] G. Uhlenbeck, and S. Goudsmit, *Nature* **117**, 264 (1926).
- [2] W. Thomson, *Proc. R. Soc.* **8**, 546 (1857).
- [3] M. Baibich *et al.*, *Phys. Rev. Lett.* **61**, 2472 (1988).
- [4] J. Barnas *et al.*, *Phys. Rev. B* **39**, 4828 (1989).
- [5] B. Dieny *et al.*, *Phys. Rev. B* **43**, 1297 (1991).
- [6] D. D. Awschalom, N. Samarth, and D. Loss (eds.), *Semiconductor Spintronics and Quantum Computation* (Springer, Heidelberg, 2002).
- [7] D. D. Awschalom and M. E. Flatté, *Nature Phys.* **3**, 153 (2007).
- [8] For an extensive review with references to the most significant phenomena see: L. I. Glazman, *Am. J. Phys.* **70**, 376 (2002).

- [9] M. A. Reed, J. N. Randall, R. J. Aggarwal, R. J. Matyi, T. M. Moore, and A. E. Wetsel Phys. Rev. Lett. **60**, 535 (1988).
- [10] U. Meirav, M. A. Kastner, and S. J. Wind Phys. Rev. Lett. **65**, 771 (1990).
- [11] For a review see R. Hanson *et al.*, Rev. Mod. Phys. **79**, 1217 (2007); Erratum in Rev. Mod. Phys. **79**, 1455 (2007).
- [12] L. Kouwenhoven and C. M. Marcus, Physics World **11**, 35 (June 1998).
- [13] P. W. Shor, SIAM J. Comput. **26**, 1484 (1997).
- [14] D. P. DiVincenzo, Science **270**, 255 (1995).
- [15] D. Loss *et al.*, Phys. Rev. A **57**, 120 (1998).
- [16] B. J. van Wees *et al.*, Phys. Rev. Lett. **60**, 848 (1988).
- [17] D. A. Wharam *et al.*, J. Phys. C **21**, L209 (1988).
- [18] J. M. Elzerman *et al.*, Phys. Rev. B **67**, 161308 (2003).
- [19] E. J. Koop *et al.*, Phys. Rev. Lett. **101**, 056602 (2008).
- [20] A. Bertoni, P. Bordone, R. Brunetti, C. Jacoboni, and S. Reggiani, Phys. Rev. Lett. **84**, 5912 (2000).
- [21] R. Ioniciou, G. Amaratunga, and F. Udrea, Int. J. Mod. Phys. B **15**, 125 (2001).
- [22] M. Blaauboer and D. P. DiVincenzo, Phys. Rev. Lett. **95**, 160402 (2005).
- [23] K. J. Thomas *et al.*, Phys. Rev. Lett. **77**, 135 (1996).
- [24] A. P. Micolich, J. Phys.: Condens. Matter **23**, 443201 (2011).
- [25] M. Büttiker, Phys. Rev. B **41**, 7906 (1989).
- [26] R. Fitzgerald, Phys. Today **55**, 21 (May 2002).
- [27] K. Ensslin, Nature Phys. **2**, 587 (2006).
- [28] S. M. Cronenwett *et al.*, Phys. Rev. Lett. **88**, 226805 (2002).
- [29] D. Goldhaber-Gordon *et al.*, Nature **391**, 156 (1998).
- [30] S. M. Cronenwett *et al.*, Science **281**, 540 (1998).
- [31] W. G. van der Wiel *et al.*, Science **289**, 2105 (2000).
- [32] L. P. Kouwenhoven and L. Glazman, Physics World **14**, 33 (January 2001).
- [33] T. Rejec and Y. Meir, Nature **442**, 900 (2006).

Chapter 2

QPC transport properties, device fabrication and measurement techniques

2.1 Introduction

This chapter discusses the Quantum Point Contact (QPC) and its transport properties. In particular, it introduces quantized conductance [1, 2] and the electron many-body effects known as 0.7 anomaly and Zero-Bias Anomaly (ZBA). The device fabrication process and measurement techniques are also discussed at the end of this chapter.

2.2 GaAs/AlGaAs heterostructure

All experimental work presented in this thesis was carried out with devices fabricated from GaAs/AlGaAs heterostructures that have a 2DEG in a quantum well below the wafer surface. A schematic of the GaAs/AlGaAs heterostructure material is shown in Fig. 2.1. The different layers of this material are grown by molecular beam epitaxy (MBE). The n-AlGaAs layer is modulation doped with Si. A heterojunction quantum well that contains a 2DEG forms at the interface between the GaAs and the undoped AlGaAs spacer layer because electrons from the Si dopants can lower their energy by transferring into this quantum well. The AlGaAs spacer layer ensures that the ionized dopants do not act as strong scattering potentials for electrons in the 2DEG, and this layer sequence thus allows for realizing 2DEGs with very high mobilities. The confinement along the z -direction (growth direction) for the 2DEG electrons is a very tight triangular potential well (Fig. 2.1c) which yields an energy spacing of about 20 meV between the quantized energy levels for confinement in this direction. In our materials only

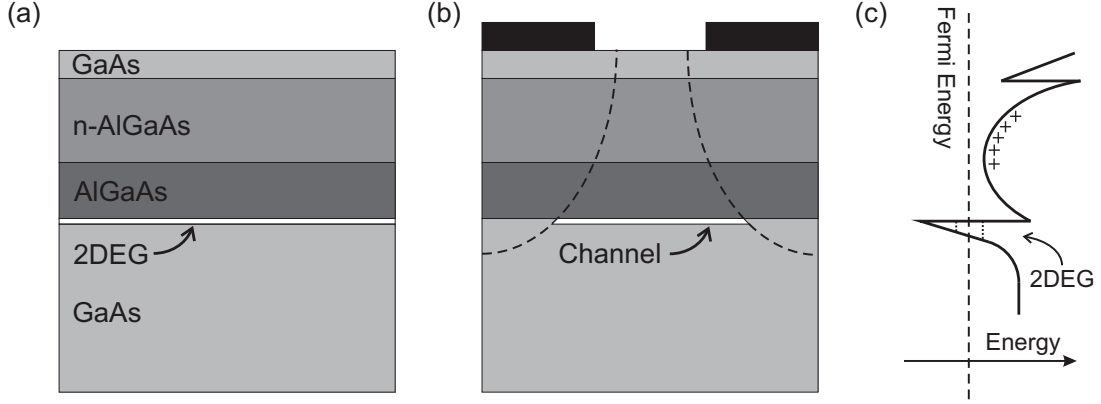


Figure 2.1: (a) Schematic of the GaAs/AlGaAs heterostructure. Different deposited layers and the 2DEG layer are labeled. (b) Metal gates (black) are deposited on a heterostructure surface. A QPC channel is formed by the electrostatic potential that results from applying a negative voltage on the gate electrodes (with respect to the 2DEG) which depletes the 2DEG below and around the gate structure. (c) Energy diagram for the GaAs/AlGaAs heterostructure with a 2DEG. The black trace is the bottom of the conduction band along the growth direction. Figure courtesy of E. J. Koop Ref. [29].

the lowest level (two-dimensional subband) is below the Fermi energy. At low temperature and bias voltage the second subband remains unoccupied and as a result electrons can only move in a two-dimensional plane, thus forming a 2DEG. The Al to Ga ratio for AlGaAs, the doping concentration of Si and the layer thicknesses can be controlled during the growth of a sample, and this allows for realizing different values for the mobility (μ_{2D}) and electron density (n_{2D}) of the 2DEG. The wafer materials used in this study were provided by our collaborators D. Reuter and A. D. Wieck from the Ruhr-Universität in Bochum, Germany. For a detailed specification of the wafers used in this research refer to Appendix A.

2.3 Quantum point contact and quantized conductance

A quantum point contact (QPC) is the simplest mesoscopic device where electron transport is ballistic. This means that the Fermi wavelength and the size of the device are smaller than the elastic and inelastic mean free path of the electrons. Experimentally, a conventional QPC is realized either by local etch-

ing of heterostructure material or by a split-gate technique. For the split-gate technique two metal gates are deposited on the surface of the 2DEG material as shown in Fig. 1.1 and Fig. 2.2a. Upon applying a negative gate voltage on the two metal gates the 2DEG under the gates is depleted and this also leads to a confining electrostatic potential between the two electrodes. The potential felt by the electrons in this region is in the shape of a saddle-point potential, as shown in the Fig. 2.2b. Similar to the case of a quantum particle in a box, the transverse confinement in this QPC channel gives quantized energy levels.

In the experiments we study the differential conductance $G = dI/dV_{sd}$ of the QPC devices with lock-in techniques. When measuring the differential conductance as a function of the applied gate voltage (which corresponds to tuning the width of the QPC channel), quantized conductance in units of $2e^2/h$ is observed, where e is electron charge and h is the Planck constant (Fig. 2.2d). The physics that underlies the quantized conductance is as follows. Electrons in the QPC channel are free to move in the longitudinal direction, but confined in the transverse directions and this results in quantized energy levels and one-dimensional subbands that carry the transport. Along the width of the channel (y -direction) the confinement is close to a parabolic potential (harmonic oscillator) [3] $\frac{1}{2}m^*\omega_0^2y^2$, where ω_0 is the characteristic frequency and m^* the effective mass. The eigenstates for the time-independent Schrödinger equation for this system have energies

$$E_n(k_x) = \frac{\hbar^2 k_x^2}{2m^*} + E_{n,y} + E_z, \quad (2.1)$$

where $\frac{\hbar^2 k_x^2}{2m^*}$ is the single-particle kinetic energy for motion along the longitudinal direction, E_z is the energy associated with confinement in z -direction and

$$E_{n,y} = (n - \frac{1}{2})\hbar\omega_0, \quad n = 1, 2, 3... \quad (2.2)$$

represents the quantized energy levels from the confinement in y -direction (n is the one-dimensional subband index). The confinement in the z -direction is very strong such that at low temperature only the lowest level is filled, and electrons only move in the x - y plane. In the above equation E_z thus only acts as a constant and it can be reduced to

$$E_n(k_x) = \frac{\hbar^2 k_x^2}{2m^*} + (n - \frac{1}{2})\hbar\omega_0, \quad (2.3)$$

Here $\hbar\omega_0$ is the subband energy separation.

Next we will derive the differential conductance for such a system (simple case of zero temperature). For studying transport one applies a voltage V_{sd} across the channel and the chemical potential in the source and drain are then related by $eV_{sd} = \mu_s - \mu_d$. The current that will flow due to the chemical potential difference is then

$$I = 2e \sum_{n=1}^{N_c} \int_{\mu_d}^{\mu_s} N_n(E) v_n(E) T_n(E) dE, \quad (2.4)$$

where the factor 2 comes from spin degeneracy, $N_n(E)$ is the 1D density of states, $v_n(E)$ is the electron-wave group velocity and $T_n(E)$ is the transmission probability through the QPC channel, and these are for the mode (subband) with index n . The number N_c is the number of occupied subbands with propagating electrons through the QPC, and it is determined by the difference between the Fermi energy and potential level in the middle of the QPC saddle-point potential (see also Fig. 2.2c). Since

$$N_n(E) = \frac{1}{2\pi} [dE_n(k_x)/dk_x]^{-1} \quad (2.5)$$

and

$$v_n(E) = \frac{1}{\hbar} [dE_n(k_x)/dk_x] \quad (2.6)$$

one gets after substituting Eq. 2.5 and Eq. 2.6 into Eq. 2.4

$$I = \frac{2e}{h} \sum_{n=1}^{N_c} \int_{\mu_d}^{\mu_s} T_n(E) dE. \quad (2.7)$$

For small V_{sd} , $T_n(E) \approx T_n(E_F)$. With $G = dI/dV_{sd}$ and substituting I and V_{sd} this yields (see also Fig. 2.2c)

$$G = \sum_{n=1}^{N_c} \frac{2e^2}{h} T_n(E_F). \quad (2.8)$$

The conductance of each mode n depends on the transmission probability. For complete transmission Eq. 2.8 can be written as

$$G = \frac{2e^2}{h} N_c. \quad (2.9)$$

This is the formula for the quantized conductance through a mesoscopic ballistic system with N_c fully open modes. Each subband contributes a conductance of $2e^2/h$. Note that this expression only contains fundamental constants, which shows that conductance quantization is a universal phenomenon. A measurement of the conductance as a function of the gate voltage that controls the width of the QPC channel is shown in Fig. 2.2d. The origin of extra small shoulder in the conductance at about $0.7 \times 2e^2/h$ (called the 0.7 anomaly) cannot be explained with the above formula, and needs a description that goes beyond this single-particle non-interacting electron model.

The result derived above here is for the linear differential conductance where only a small ac excitation voltage V_{sd} is applied across the device for a lock-in measurement of G (with $eV_{sd} < 4k_B T$, where T is temperature and k_B is the Boltzmann constant). For the QPC studies we also measure the nonlinear differential conductance where a dc source-drain voltage is applied (with $eV_{sd} > k_B T$) in addition to the small ac excitation voltage that is used for probing the value of G .

2.4 The 0.7 anomaly

Besides the physics of quantized conductance as described in the previous section, there are few phenomena associated to the transport properties of a QPC that are still under debate after more than two decades since their discovery. The most important of these phenomena is the 0.7 anomaly. The 0.7 anomaly appears in the linear conductance of a QPC and it is a deviation in the perfect quantization of QPC conductance. It is observed as an extra shoulder in quantized conductance traces at about $0.7 \times 2e^2/h$ (Fig. 2.3) but it has been reported that it can appear anywhere between $\sim 0.5 \times 2e^2/h$ and $\sim 0.9 \times 2e^2/h$ [61]. The 0.7 structure has been overlooked or ignored in the initial papers (1988-1996) as it was thought to be due to imperfections in the device structures. For example, in the very first paper on the discovery of the quantized conductance steps in QPCs there was an anomaly for the first conductance step (hence only partly shown) [1], that has in fact strong similarity with the 0.7 anomaly. The first systematic study of the 0.7 anomaly was reported by Thomas *et al.* [4] in 1996 and they showed that this feature is generic and not caused by imperfections in the device structures, and that it also appears for QPCs made with the cleanest 2DEG systems that show otherwise a near-perfect manifestation of quantized conductance. Now it is recognized that the 0.7 anomaly is a very generic phe-

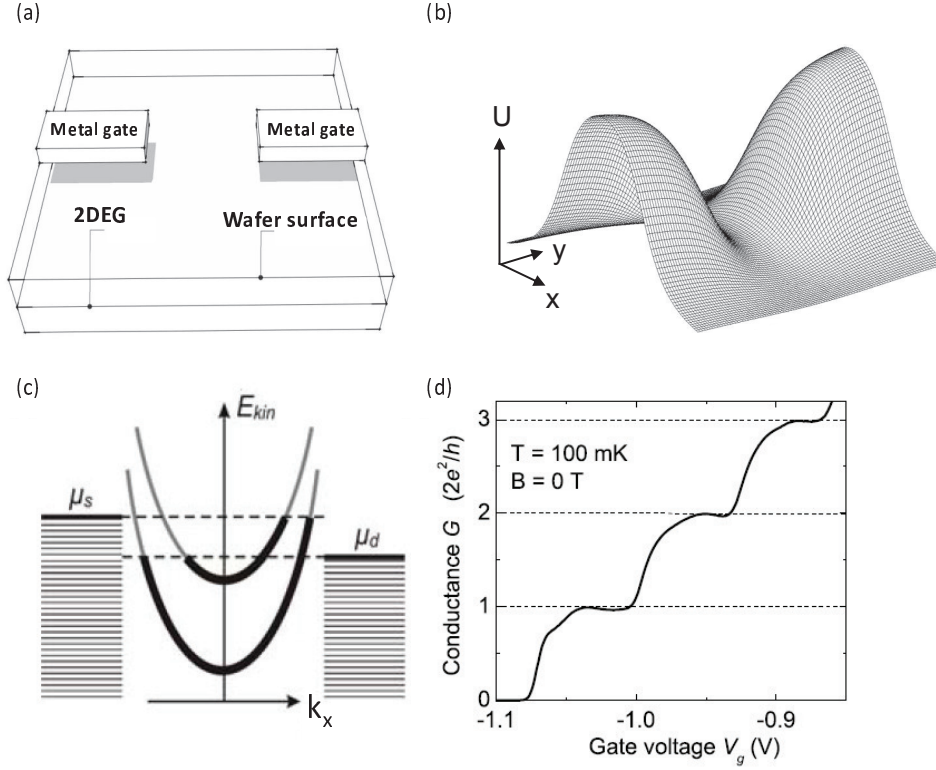


Figure 2.2: (a) Schematic of a quantum point contact (QPC). Metal gates are deposited on a wafer with a 2DEG below its surface. (b) The saddle-point potential formed in the QPC region due to applying a negative gate voltage. (c) Energy and dispersion of the 1D subbands in the QPC channel as a function longitudinal wavevector k_x for the case of a small applied bias voltage between the source and drain electron reservoirs (at chemical potentials μ_s and μ_d , respectively). Each subband results from a quantized energy level from transverse confinement. For the depicted case there are 2 subbands contributing to electron transport, which gives a QPC conductance of $2 \times 2e^2/h$. (d) Measurement result for the conductance G of a QPC, quantized in steps of $2e^2/h$, as a function of gate voltage V_g in zero magnetic field (measured on the device of Fig. 3.1).

nomenon for short 1D transport systems and it has been observed with QPCs in various material systems which include GaAs/AlGaAs-based 2DEG [4], 2D hole systems [43], cleaved-edge overgrown wires [42], Si systems [7] and graphene [40]. The most common transport properties of the 0.7 feature and their dependence on temperature and magnetic field are described below.

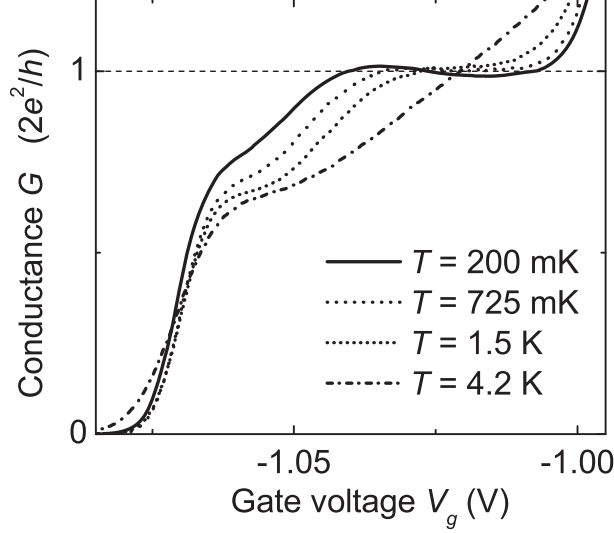


Figure 2.3: Evolution of 0.7 anomaly as a function of temperature (measured on the device of Fig. 3.1). Figure courtesy of E. J. Koop Ref. [29].

2.4.1 Temperature dependence of the 0.7 anomaly

A trademark feature of the 0.7 anomaly is that it appears more pronounced with increasing temperature and that it even remains present at temperatures where quantized conductance plateaus start to disappear due to the fact that $k_B T$ becomes larger than the 1D subband spacing. Fig. 2.3 shows the temperature dependence of the 0.7 anomaly for one of our devices. It becomes more pronounced with increasing temperature. The 0.7 anomaly is the only feature that survives in the trace for the temperature of 4.2 K.

2.4.2 Magnetic field dependence of the 0.7 anomaly

Upon applying a magnetic field in the plane of the 2DEG (a perpendicular magnetic field would bring the 2DEG in the quantum Hall regime) the small plateau of the 0.7 anomaly smoothly evolves into the lowest spin-resolved quantized conductance plateau at $0.5 \times 2e^2/h$ (see Fig. 2.4). These spin-resolved quantized conductance plateaus appear due to Zeeman splitting of the 1D subbands in the QPC, and appear as quantized conductance with steps of e^2/h instead of the zero-field steps of $2e^2/h$. The Zeeman splitting is $\Delta E_z = g^* \mu_B B$ where g^* is the effective g-factor, μ_B is the Bohr magneton and B is the magnitude of the

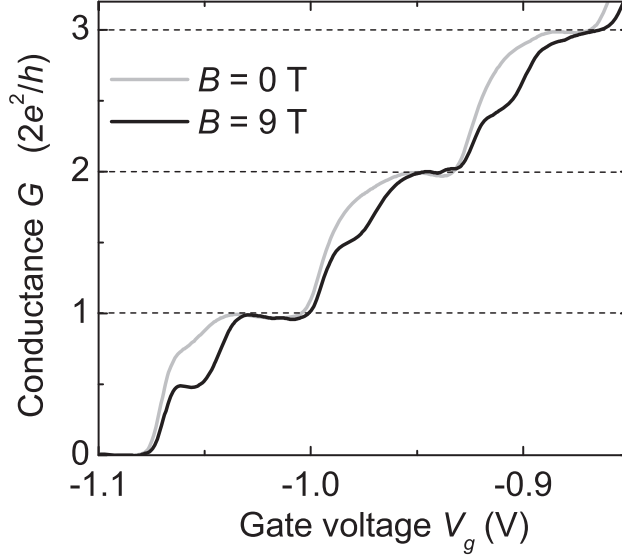


Figure 2.4: The linear conductance G of a QPC for zero magnetic field and for the case of a strong magnetic field applied in the plane of the 2DEG. In a strong field the number of plateaus doubles (with steps of e^2/h instead of $2e^2/h$) because of a significant Zeeman splitting between 1D subbands for the spin-up and spin-down electrons (measured on the device of Fig. 3.1). Figure courtesy of E. J. Koop Ref. [29].

applied magnetic field. Thomas *et al.* [4] who first studied the gradual evolution of the 0.7 plateau into the 0.5 plateau interpreted this observation as a hint that the 0.7 anomaly (in zero magnetic field) could be the result of interactions that cause a spontaneous spin splitting for the lowest 1D subband.

2.5 The Zero-Bias Anomaly (ZBA)

The Zero-Bias Anomaly (ZBA) of QPCs is the enhancement of conductance around zero bias voltage that can be observed in measurements of the nonlinear conductance. For the data in Fig. 2.5a the ZBA signature can be recognized at conductance levels between $\sim 0.2 \times (2e^2/h)$ and $\sim 0.95 \times (2e^2/h)$ inside the window $V_{sd} \approx \pm 0.2$ mV (in this figure labeled as V_{DC}). (The structure on the traces for larger V_{sd} has been partially interpreted as half-integer quantized conductance plateaus that appear when the bias voltage equals the 1D subband spacing [13, 14], but peaked deviations from this picture possibly also concern many-body effects, now for a situation that is strongly out of equilibrium. These

have not been investigated much till now in the QPC literature.)

Like the 0.7 anomaly, the origin of the ZBA is not understood, and there are different models and theories that aim at explaining this feature. Since both the ZBA and the 0.7 anomaly occur around $V_{sd} = 0$ at conductance levels around $0.7 \times (2e^2/h)$ they are possibly related, so it is important to study these two phenomena together. However, whether the 0.7 anomaly and the ZBA are intrinsically related is under debate [61]. The reported behavior of the ZBA as a function of temperature and magnetic field is described below.

2.5.1 Temperature dependence of the ZBA

The height of the ZBA decreases as the temperature of the system is increased [21, 28]. It is well established that the appearance of a ZBA for transport through quantum dots and its temperature dependence are the signature of Kondo physics for a net single electron spin in a quantum dot that is coupled to a reservoir [38, 39]. This aspect of the ZBA and its relation with the ZBA for QPCs will be discussed in detail in the next section.

2.5.2 Magnetic field dependence of ZBA

The ZBA behaves differently at different conductance levels when an in-plane magnetic field is applied [14, 21]. Fig. 2.5 shows how the ZBA appears in zero magnetic field and corresponding measurements recorded with a 9 T in-plane magnetic field. At 9 T an additional accumulation of traces (compared to zero field) is seen at $0.5 \times 2e^2/h$ and $1.5 \times 2e^2/h$ because each spin-degenerate quantized conductance plateau develops into two separate plateaus (see also Fig. 2.4). In addition, for most conductance levels the ZBA is no longer present (except for conductance directly below the 1 and $2 \times 2e^2/h$ plateaus). For intermediate values of the applied magnetic field (~ 1 T) the ZBA splits into two peaks due to Zeeman splitting (data not shown). This splitting is not observed at all conductance levels. Within a Kondo interpretation of the ZBA this is attributed to having a different ratio between the Zeeman energy and the Kondo temperature at different conductance levels [14, 21, 56]. In many studies the ZBA is found to collapse (as for the 9 T data) without showing any splitting in its field dependence [28].

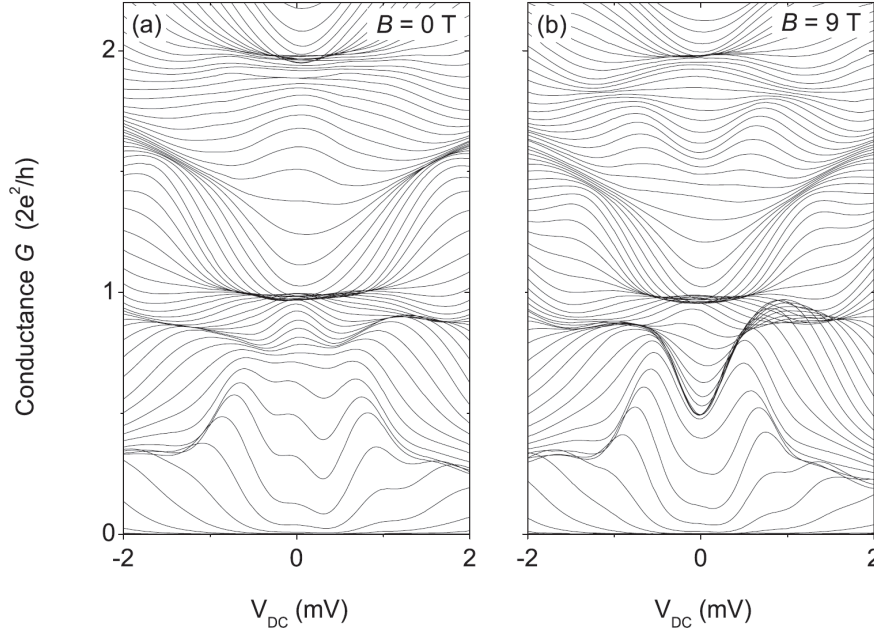


Figure 2.5: Differential conductance as a function of dc component V_{DC} in the bias voltage V_{sd} for zero magnetic field (a) and 9 T field (b). The enhanced conductance around zero bias voltage in (a) is called the Zero-Bias Anomaly (ZBA). Figure courtesy of E. J. Koop Ref. [29].

2.6 Review of literature on the 0.7 anomaly and ZBA

This section reviews publications by others about experimental and theoretical efforts that aimed at explaining the origins of the 0.7 anomaly and the ZBA. The main theories and interpretations for the origins of the 0.7 anomaly and ZBA are spontaneous spin polarization, self-consistent localized states with Kondo physics, Wigner crystal formation, subband pinning, electron-phonon interaction, singlet-triplet transitions and charge density oscillations (for a review see Ref. [61]). The first two are the most widely considered scenarios.

2.6.1 Spontaneous spin splitting

The very first systematic study of the 0.7 anomaly by Thomas *et al.* [4] proposed that it was due to spontaneous spin polarization. They observed as a function of magnetic field a smooth evolution of the 0.7 feature into the spin-resolved

plateau at $0.5 \times 2e^2/h$ and interpreted this as a signature that the 0.7 anomaly appears because of spontaneous spin polarization in zero magnetic field due to the many-body interactions.

Further support for a role for spin in the origins of the 0.7 anomaly and ZBA comes from observations of enhanced g-factor values for electrons in the QPC channel [5] (see also our data [28] in *Chapter 3*). While for 2DEG electrons the g-factor is close to $g = -0.44$, the g-factor in the QPC channel can take on values near $|g| \approx 1$. This g-factor enhancement is strongest for transport with only the lowest 1D subband occupied (low electron density in the QPC channel) and reduces for the higher subbands that contribute to transport when further opening the QPC. This g-factor enhancement is also assumed to result from electron many-body interactions. A first theoretical paper that showed exchange-enhanced spontaneous spin polarization in long 1D wires was published in 1996 by Wang *et al.* [9]. They observed strong enhancement of the g-factor for low electron densities, where interaction effects are strongest. In 1998 Wang *et al.* [10] reported calculations of spontaneous spin polarization for a QPC system and showed that a 0.7-anomaly-like feature can appear in the conductance if interaction effects are taken into account.

The phenomenological model by Reilly *et al.* [11, 12] is also based on the assumption that there is a zero-field spin splitting for electrons in a QPC. The model is successful in the sense that it produces the experimentally observed dependence of the 0.7 anomaly on temperature, magnetic field and bias voltage. This model assumes a density dependent spin gap in the channel. In particular, the assumptions are: (i) the energy of spin bands is density dependent; (ii) a spin gap opens up when a spin-up subband is at the level of the Fermi energy E_F , as is shown in Fig. 2.6. This figure shows the spin-gap opening for different 1D subbands as a function of gate voltage (here labeled as V_s) or density (n). The dashed line shows the nonlinear Fermi-energy dependence on the density. The subbands remain non-split until they get populated. After one spin mode moves above the Fermi level a spin gap starts to open up and it grows with increasing density. The spin splitting gets weaker for the higher subbands.

Several research groups [18, 19, 20] worked on obtaining experimental evidence for spontaneous spin polarization in QPC channels. Derby *et al.* [19] suggested a Hanle-precession measurement scheme to measure the claimed spontaneous spin polarization in their supplementary information. Frolov *et al.* [8] tried to measure the Hanle precession of spontaneous spin polarization but did not find any signature of it. Attempts to study spontaneous spin polarization in QPCs

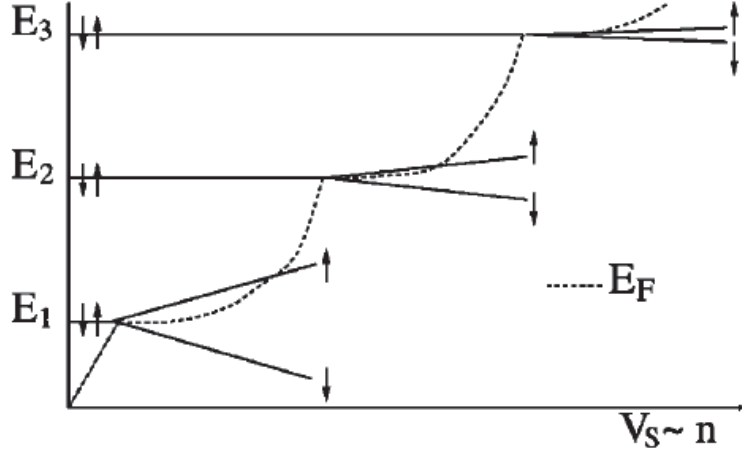


Figure 2.6: Spin-gap opening with increasing 2DEG density (Figure adopted from Ref. [11]).

with a magnetic focussing technique did yield some signatures for a static spin polarization in QPC channels, but the full body of work with this technique did till now not yield a convincing and consistent picture [15, 16, 17].

In the models with spontaneous spin polarization or spontaneous opening of a spin gap, the direction of this spin polarization is generally not discussed. In addition, for the phenomenological models the physics that causes the spin-gap opening or spin polarization remains unclear. In experiments, the 0.7 anomaly becomes stronger with increasing temperature and this is not consistent with most of the models that assume spontaneous spin polarization. The signatures in QPC transport that have strong similarity with transport through a Kondo impurity (discussed in the next section) can only be the result of Kondo physics in QPCs if there is no static spin polarization in the QPC channel (as claimed in [17]). All together, the theories and experiments that focus on a role for static spin polarization do not provide a complete and consistent description at this stage.

2.6.2 Spontaneous self-consistent localized states and the Kondo effect

In this section we will discuss scenarios that assume that the 0.7 anomaly and the ZBA have their origin in the formation of one or more self-consistent localized electron states in the QPC channel and experimental results that point to

this scenario. This research direction was inspired by QPC transport results that showed similarities with Kondo transport [14, 21]. For a Kondo effect to arise in a system, a localized spin state is required since the Kondo effect is the interaction between a localized spin and the spins in a nearby electron reservoir. Below we first review the theories that predict the localization due to many-body interactions. Subsequently, we introduce the Kondo effect in general and review the signatures of Kondo physics found in the QPC transport properties.

Self-consistent localized states in an open system

There have been several theoretical efforts [30, 31, 32, 33, 37] with calculations that show that one or more self-consistent localized states can form in the center of the QPC channel, despite the fact that the QPC saddle-point potential is an open quantum system. The self-consistent localized state formation has its origin in a Friedel oscillation [41] that occurs in the QPC channel. In the QPC case electrons in the channel screen the saddle-point potential barrier and this gives an oscillatory pattern in the electron density that extends from the center of the QPC into the reservoirs [30, 31, 36]. The Friedel oscillation mechanism has been observed to play a role in the transport properties of QPCs [44]. Calculations that yield such Friedel oscillations, and which also account for Coulomb and exchange interactions between electrons, show that the Friedel oscillations develop into self-consistent localized state due to the electron-electron interactions.

From this research direction, Fig. 2.7 shows results of Spin-Density Functional Theory (SDFT) calculations for a conductance level close to the first quantized plateau [32]. Figure 2.7a,b show the spin density for spin-up and spin-down, respectively, in the 2DEG plane around the QPC channel. A single electron with spin-up appears in a self-consistent localized state in the center of the channel, while for spin-down a pair of weakly localized states appear on either side of the QPC. The spin direction of a SDFT solution is here pinned in one particular direction for the purpose of the calculation, but this should not be interpreted as a static spin polarization. Instead, the result should be interpreted as having a localized state with about one electron of charge and a net spin of about $\frac{1}{2}\hbar$ that is a dynamic spin polarization which can point in any direction while maintaining correlations with the spin direction of other electrons that are nearby (due to exchange).

This localization due to electron-electron interactions can be visualized by calculating the self-consistent (so-called Kohn-Sham) potential for an electron (the white dashed lines in Figs. 2.7c,d). For the spin-up solution (left plots)

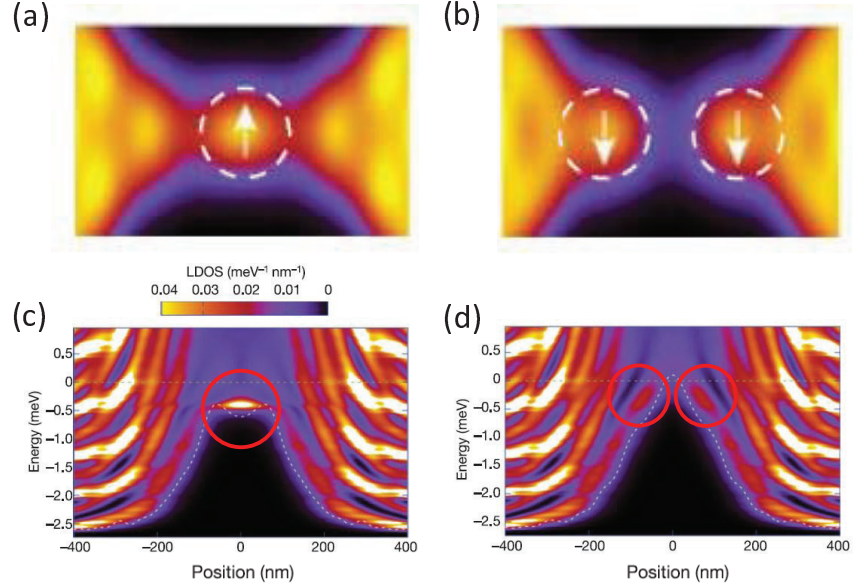


Figure 2.7: Self-consistent localized states calculated with Spin-Density Functional Theory (SDFT) for a conduction level just below the first plateau. The results in (a),(b) show the charge density for spin-up (a) and spin-down (b) in a QPC channel (top view on 2DEG plane) on a color scale from zero (black) to $0.35 \cdot 10^{11} \text{ cm}^{-2}$ (yellow). In (a) a single localized state with a net spin and about one electron of charge is localized in the center of the QPC, while two states for the opposite spin appear away from the center on either side of the QPC. (c),(d) SDFT calculations of the local density of states (LDOS) for the same settings as in (a) and (b) show the same localized states (highlighted by circles on the plots). The Kohn-Sham potentials that account for many-body interactions are also shown by the white dashed lines and these cause the localization of spins (figure adopted and modified from Ref. [32]).

the white dashed lines show a double-barrier in the center of the QPC. These same figures show the calculated local density of states (LDOS) which give more insight in the localization phenomenon. In these plots the Fermi energy is at zero energy. The localized states (encircled) act as trapping sites just below the Fermi energy. The formation of such a localized state appeared in these calculations for a wide range of device dimensions and material parameters. Calculations for longer QPC channels showed for some cases solutions with a pair of localized states in the center of the channel instead of a single state [32] (further discussed in the section below on Kondo physics).

The self-consistent localized state scenarios [30, 31, 32, 33, 37] have been questioned by other authors [34, 35] who claimed to find contradicting results

while setting up similar calculations. The DFT or SDFT calculation results differ from group to group, which indicates that obtaining reliable results requires a high level of dedicated expertise, and that expert knowledge is required for evaluating the reliability. The results for the spin-resolved local density of states (LSDA) of Ref. [35] found rich charge and spin structure at the two ends of the QPC, but no signs of a localized single spin state in the center of the QPC. There are several reports of experimental results that are interpreted as signatures of a single self-consistent localized state [21, 50, 51, 52, 53, 54, 55]. However, till now there is no experimental report that demonstrated the presence of self-consistent localized states in all its aspects and which was convincing enough to end the debate on the question whether they occur in QPCs.

Kondo effect arising from localized spins

The Kondo effect arises when a single electron spin is localized but still has a weak interaction with an electron reservoir (the effect can also occur for a few coupled localized electron spins). The spins in the reservoirs then screen the localized spin, effectively quenching the net spin at the localized site by (in a semi-classical picture) frequently exchanging it with a reservoir spin of opposite direction (for a review see Ref. [48]). This gives in fact localization for a small cloud of electrons, and this has influence on the transport properties of the system. In the case of bulk normal metals with a low concentration of Kondo impurities (magnetic atoms) this gives an *increase* in their resistivity when cooling to the lowest temperatures. This anomalous resistivity behavior was a puzzle for a very long time until Jun Kondo finally explained it in 1964 [47]. He showed that this effect only takes place below a particular low temperature, now called the Kondo temperature T_K . Around and below T_K , the resistivity increases logarithmically when lowering the temperature. Later studies solved the puzzle of observing finite resistivity values when the temperature approaches absolute zero by showing that at low enough temperature the localized spin and the spins surrounding it form a correlated state, with the result that the net spin is quenched and this gives a deviation from the logarithmic divergence.

The Kondo effect is a very general phenomenon and is observed in many condensed matter systems. For a Kondo phenomena to appear at a specific low temperature, a net localized spin is required. The interest in the Kondo effect has attained renewed interest since its discovery in quantum dots [38, 39, 23, 24, 25, 48]. A quantum dot is a small conducting island in a semiconductor, also known as artificial atom. It is a nano-electronic device that contains one or a few

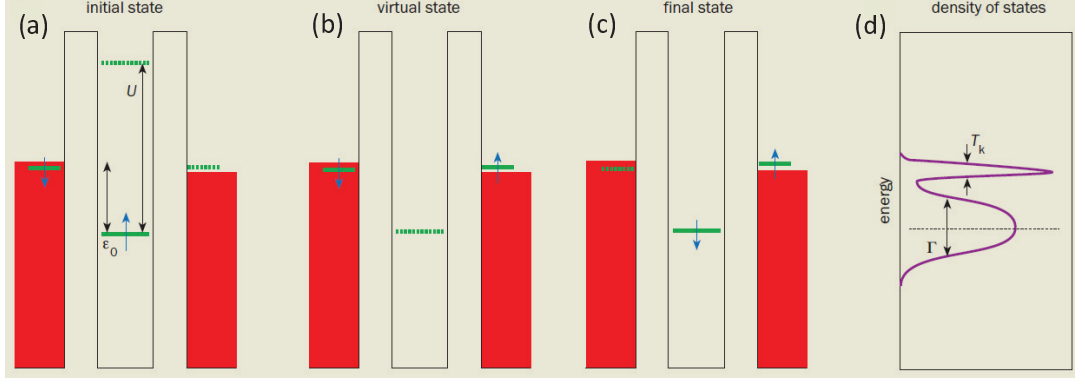


Figure 2.8: Schematic explaining the formation of a Kondo resonance in quantum dots (Figure adopted and modified from Ref. [48]).

localized electrons, with properties that can be tuned with gate electrodes as for the QPC. Notably, for mesoscopic systems like quantum dots the Kondo electron cloud tends to delocalize a confined electron, such that the Kondo effect gives a *lower* resistance (higher conductance) for transport through a quantum dot. The review Ref. [48] includes a discussion of the Kondo effect for quantum dots.

Figure 2.8 shows a schematic for the formation of the so-called Kondo resonance for a quantum dot. In a quantum dot, the number of electrons can be changed one by one and the electrons are in discrete energy levels. For the case of an odd number of electrons a quantum dot behaves as a Kondo impurity. In the figure the red bars depict filled states up to the chemical potential for the source (left) and drain (right) reservoirs. In Fig. 2.8(a) the dot contains a single spin, at an energy ϵ_0 below the chemical potential of the leads. The two high bars adjacent to the source and drain regions represent tunnel barriers. The single electron cannot tunnel out as its energy is lower than the chemical potential of the leads. Adding another electron to the dot requires an addition energy equal to $U - \epsilon_0$ where $U = e^2/C$ is the on-site Coulomb repulsion energy with C for the capacitance of the dot. For very low temperature where $k_B T$ is less than both $U - \epsilon_0$ and $\mu - \epsilon_0$ (μ is the average chemical potential of the leads), electron transport is blocked (known as Coulomb blockade [22]). In the Coulomb blockade regime at low temperature the current from first order tunnel events is zero.

Quantum mechanically, as allowed by Heisenberg's uncertainty principle, the electron on the dot can tunnel to one of the leads for a very short time given by $\hbar/|U - \epsilon_0|$. This situation is called a virtual state and is shown in Fig. 2.8b. During this short time interval another electron from one of the leads can fill the empty

state in the dot. The end result of this process is that the electron in the dot can be in a state with opposite spin (Fig. 2.8c). A long sequence of such spin-flip events results in an increase of the conductance of the otherwise blocked quantum dot system. This can be described as an enhancement of the density of states for the dot at the chemical potential of the leads (so-called Kondo resonance, Fig. 2.8d). This gives rise to an enhanced conductance around zero bias voltage, which is observed as a peak in the nonlinear conductance of the dot [38, 39]. With an in-plane magnetic field this peak splits into two peaks [38, 39] at $\pm g^* \mu_B B / e$ (a splitting that is twice the Zeeman energy [26], which is a key characteristic of the Kondo effect).

The temperature at which the Kondo resonance starts to form is called the Kondo temperature and is given by $T_K \approx \sqrt{U\Gamma} \exp[-\pi(\mu - \epsilon_0)/2\Gamma]$, where $\Gamma = \Gamma_L + \Gamma_R$ is the lifetime broadening of the dot and controlled by the left and right tunnel barrier. Due to the exponential dependence T_K is very sensitive to little changes in the parameters on which it depends. Another feature of the Kondo systems is that they obey universal Kondo scaling. This means that ratio between the conductance $G(T)$ at a given temperature T and the saturation conductance at zero temperature $2e^2/h$ only depends on the ratio T/T_K . It is given by (using notation $G_0 = 2e^2/h$)

$$G(T)/G_0 = f(T/T_K) \approx [1 + (2^{1/s} - 1)(T/T_K)^2]^{-s} \quad (2.10)$$

where $s = 0.22$ for the case of spin- $\frac{1}{2}$. Note that T_K is here a single fitting parameter. Curves of $G(T)/G_0$ for different systems or system settings all fall on top of each other when plotted as a function of T/T_K [27, 23, 24, 25, 48].

The Kondo effect in QPCs

We now turn to discussing signatures in QPC transport that have been interpreted as Kondo physics. Cronenwett *et al.* [21] first pointed out the similarities between the transport properties of QPCs and quantum dots containing a net single spin and its relation with the appearance of the 0.7 anomaly and the ZBA. The similarities are the following:

(i) The temperature dependence of the linear conductance of a QPC could be scaled as Eq. 2.10 for quantum dots, but with a slightly modified form given by

$$G(T)/G_0 \approx \frac{1}{2}[f(T/T_K) + 1] = \frac{1}{2}[1 + (2^{1/s} - 1)(T/T_K)^2]^{-s} + \frac{1}{2}. \quad (2.11)$$

This equation differs from (Eq. 2.10) for the high temperature limit for G which is e^2/h rather than zero. The motivation for using this modified scaling law was purely empirical [14, 21], and is till now not followed up by a theoretical explanation.

(ii) The ZBA of QPCs splits into two peaks in a parallel magnetic field due to Zeeman splitting, in a similar way as for quantum dots [39]. The splitting of the ZBA does not appear for all conductance levels $0 < G < 2e^2/h$, which is attributed to the fact that Kondo temperature is different at different conductance values [21]. Ren *et al.* [56] claimed a change in the splitting from time to time in a single cool down, which was attributed to a minor rearrangement of charged states in the QPC environment.

(iii) The Full-Width at Half-Maximum (FWHM) of the ZBA matched with the with the Kondo temperature that was estimated from fitting the temperature dependence of G to Eq. 2.11 [21]. For $G > 0.7 \times 2e^2/h$ the width of the ZBA agreed with $\sim 2k_B T_K/e$. However, the width of the ZBA for $G < 0.7$ was found to be the constant while T_K from scaling is here on a trend to much lower values.

Several features of Kondo physics are convincingly present in the QPC transport properties. Still, the observed Kondo signatures are not completely understood. For example, the ZBA is observed for $0 < G < 2e^2/h$ but the width only agrees with the Kondo scaling for $G > 0.7 \times 2e^2/h$. In addition, the Kondo scaling needs to assume an unexplained offset of $0.5 \times 2e^2/h$ from zero. There is not much information available on what exactly causes a ZBA even to appear below $0.5 \times e^2/h$. It was suggested [56] that two asymmetrically coupled localized states on either side of the QPC can cause the ZBA at low conductance values.

The occurrence of Kondo physics indeed needs an explanation why localized states are present in QPCs, and this was till now only supported by the theoretical work that we discussed above here. From this work it is interesting to note it was also predicted that a pair of self-consistent localized states can form in a QPC channels with a certain length. This would realize a two-impurity Kondo system [46, 45], which has as its fingerprint a double-peak ZBA and nonmonotonic scaling of $G(T)/G_0$. This thesis work observed such signatures for the first time, and this will be presented in *Chapter 4*.

2.6.3 Wigner crystal and other theories

Despite the fact that QPCs are very short 1D channels, several theoretical efforts aimed to explain the 0.7 anomaly with physics of 1D systems. In 1D systems

electron-electron interactions are more important than for 2D or 3D system and the transport properties are then described by a Luttinger liquid model rather than Fermi-liquid theory. Transport is suppressed for Luttinger liquid behavior and this appears as a ZBA with a dip at zero source-drain bias. This ZBA shows power law dependence on both temperature and bias voltage. With QPCs this not observed, so the need for Luttinger-liquid theory for explaining the 0.7 anomaly is not obvious.

At a very low electron density, interactions becomes even more important. Here the potential energy dominates over the kinetic energy and in order to minimize the potential energy an ordered chain of electrons called Wigner crystal was predicted [57]. It was observed experimentally in carbon nanotubes [58]. This Wigner crystal formation is also considered for explaining the 0.7 anomaly [60, 59]. It was shown theoretically [60] that in a strong interaction regime electrons form a Wigner crystal with a small anti-ferromagnetic spin exchange J . Two situations can arise in that case: (i) For $k_B T \ll J$ the conductance almost remains $2e^2/h$. (ii) For $J \ll k_B T$ the conductance drops to e^2/h . In experiments with long wires the 0.7 feature has been observed to move to e^2/h [6]. In a recent study [37] it was shown that the number of localized electrons that constitute the lattice depends on the length of the wires. The electron lattice is separated from the liquid phase in the leads by a gap. For a sharp barrier the electron lattice is isolated very well from the liquid phase electrons in the leads and the lattice electrons are in a Coulomb blockade regime.

However, these models are calculations for extended 1D systems while QPCs are rather short wires ranging from 100 nm to 1 μm length, and the 0.7 anomaly is almost always observed in short as well as in long QPCs. A more realistic approach where these 1D theories are worked out for 1D systems of rather short length would need to rely of heavy numerics, and one could envision that the results then coincide with the SDFT calculations on localization. Note that these can also be described as Friedel oscillations that develop into a very short Wigner crystal when accounting for electron-electron interactions.

2.7 Device fabrication

2.7.1 Electron-beam lithography

Electron-beam lithography (EBL) is a patterning technique for making devices of any design with a resolution of few nanometers. For our research we used the

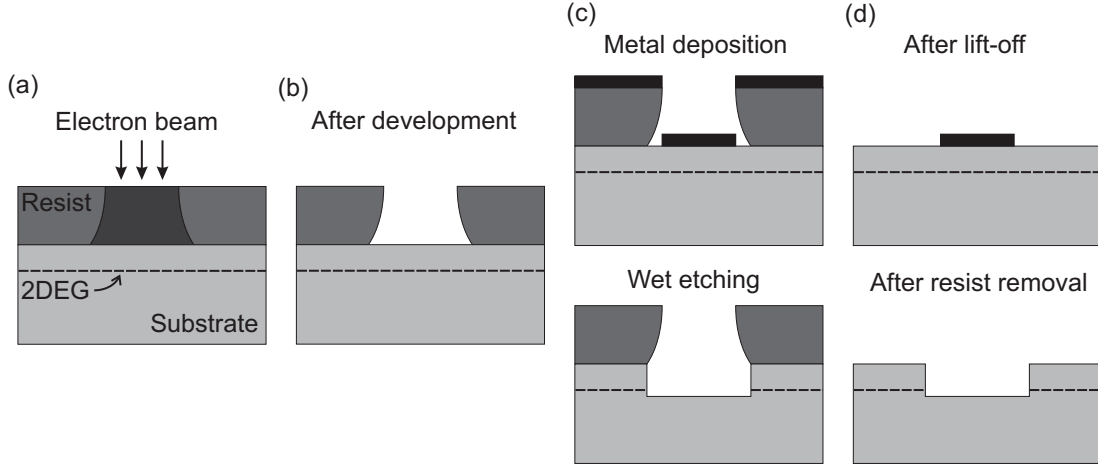


Figure 2.9: Schematic representation of a single fabrication step that uses electron-beam lithography to either define metal structures or to etch the surface of a heterostructure wafer. **(a)** Writing a pattern in the resist by local electron-beam exposure. **(b)** The e-beam exposed area of the PMMA is dissolved in a developer. **(c)** On the exposed part either a metal is evaporated (top figure) or it is subject to wet etching (bottom figure) with a acidic solution. **(d)** The remaining resist (PMMA) and metal (lift-off step) on the wafer is removed in an acetone solution. Figure courtesy of E. J. Koop Ref. [29].

Raith E-line system. EBL design software allows to make any kind of design that is then transferred to a resist layer (polymethyl methacrylate, PMMA) on the sample by local electron beam (e-beam) exposure. The PMMA is an e-beam sensitive [49] material with long polymer chains that break at a certain dose of e-beam exposure. PMMA comes with different molecular weights and can be dissolved in different solvents. It can be spin coated easily on a sample surface. The e-beam dose needed to break the PMMA chains depends on its molecular weight: PMMA with low molecular weight is more sensitive to e-beam exposure than one with higher molecular weight. After spinning PMMA it is baked at 180 °C in an oven for 15 minutes to evaporate all the solvents. Baking on a hot plate is faster and requires only a few minutes.

For our fabrication we have used two types of PMMA. One is 950K PMMA dissolved in ethyl-L-lactate (2%). The second type is 50K PMMA dissolved in chlorobenzene (9%). For deposition of thick metal layers or large structures it is useful to use PMMA double layers, where the PMMA 950K is deposited on top of the 50K layer. The clearing dose for the top layer is then higher than for the bottom layer and this gives an undercut in the developed PMMA. This is

important for easy lift-off. The PMMA 50K has about 20% higher sensitivity than PMMA 950K. For high-resolution patterns (*e.g.* QPC gates) a single layer of PMMA 950K with a thickness of ~ 70 nm is used. The thickness of a PMMA layer can be controlled by the PMMA content in its solvent and via the spin coating rotation speed. A speed of 4000 rpm gives a layer thickness of 400 nm and 70 nm for our PMMA 950K (2%) and PMMA 50K (9%), respectively.

A single step of EBL processing is illustrated in Fig. 2.9. The PMMA resist is exposed to the e-beam at predefined positions as shown in Fig. 2.9a. The molecular chains of the PMMA break in the exposed parts and can easily be removed by a developer (Fig. 2.9b). For developer we use a 1:3 solution of methyl-isobutyl-ketone (MIBK) and isopropanol (IPA). For single and double layers of PMMA we develop for 35 and 60 seconds, respectively. To avoid overdeveloping the process is stopped by rinsing the sample in an IPA solution for about 30 seconds. The unexposed PMMA remains unaffected in the developing step. For our fabrication the next processing step with the exposed (uncovered now) parts of the sample is one of the following: Either a thin metal layer is deposited or it is etched in an acidic solution (Fig. 2.9c). The PMMA covered part remains unaffected in the etching process. In both the cases the remaining resist and any metal on top of it (lift-off, Fig. 2.9d) is removed in an acetone solution, and further cleaned by rinsing in IPA.

2.7.2 Fabrication steps

For the fabrication of a QPC device 5 EBL steps are required and these are shown in Fig. 2.10. Appendix B describes the fabrication steps in more detail.

Alignment markers

For a fabrication process with many steps one needs alignment markers to align the structures of the various steps. Making markers for this is the first fabrication step (Fig. 2.10a). We used 4 markers (in cross shapes) on each corner of the device. The length of each marker line is $50\text{ }\mu\text{m}$, with a width of $5\text{ }\mu\text{m}$. A uniquely positioned small square is added to the marker on each corner such they can be distinguish. A 45 nm Au layer with 5 nm Ti sticking layer is deposited for the markers.

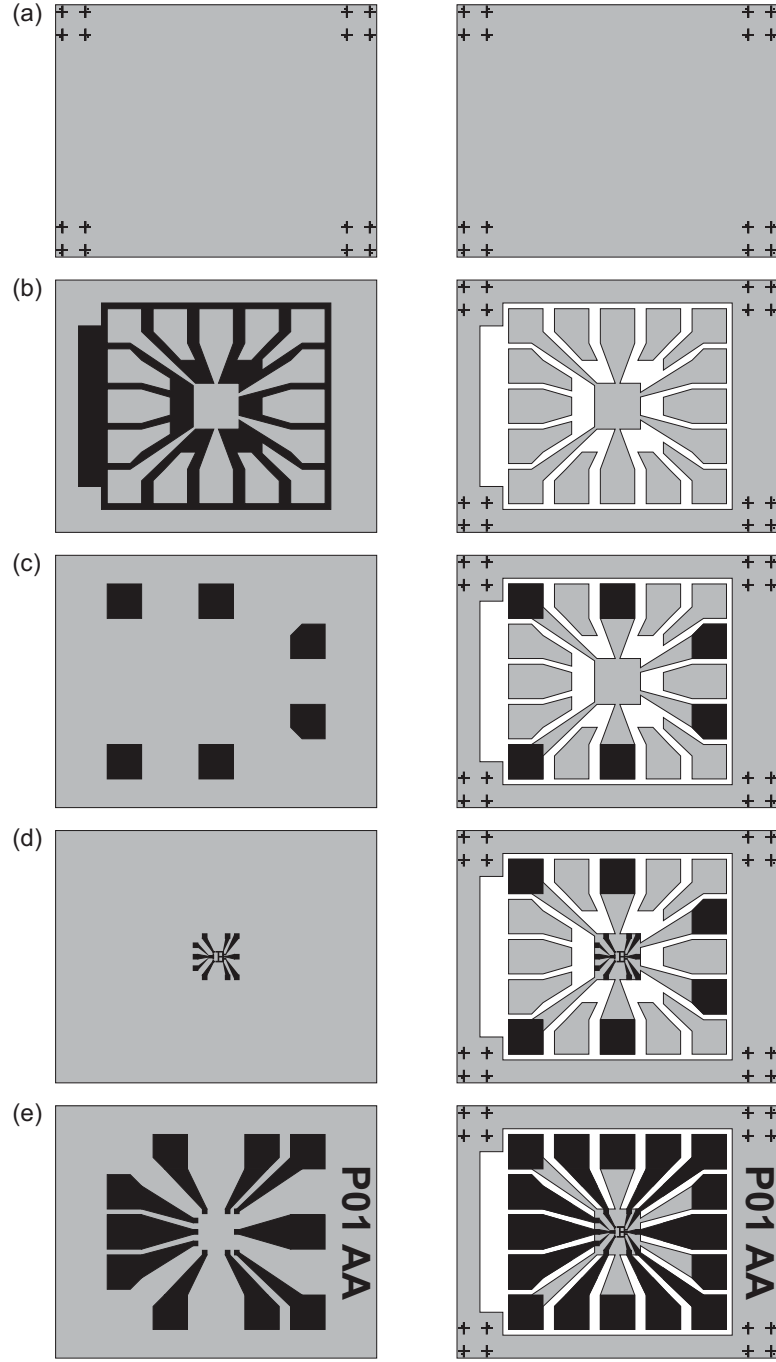


Figure 2.10: Electron-beam lithography steps for the fabrication of Quantum Point Contact devices. The e-beam exposure (black) for each step is shown in the left column, while the right column shows the subsequent result after further processing of (a) alignment markers, (b) mesa etching, (c) ohmic contacts, (d) small gates (not to scale), and (e) large gates. The black color in the right column represents deposition of metal and the white color represents area that has been subject to wet etching for locally removing the 2DEG. Figure courtesy of E. J. Koop Ref. [29].

Mesa etching

The fabrication of a mesa concerns the etching of the heterostructure parts where the 2DEG needs to be removed. This is needed for creating well-defined boundaries to 2DEG regions, such that current only flows in these designated regions. We etch the sample down to the depth of the 2DEG (Fig. 2.10b). For wet etching we use $\text{H}_2\text{SO}_4:\text{H}_2\text{O}_2:\text{H}_2\text{O}$ with a composition of 1:1:50. The etching rate is approximately 2 nm/sec. After etching the sample is rinsed in 3 beakers with de-ionized water for 1 min each to stop the reaction. At the end resist is removed in acetone, with further cleaning in IPA.

Sample preparation and resist spinning needs careful attention for the etching step. The used pre-baking time of the resist is different than for other fabrication steps. In this case it is one and half hour at 180 °C to make sure that the resist sticks very well to the substrate and that all the solvents are evaporated. A post-bake of 15 min after developing is also very helpful for getting good etching results. If there is dirt on the sample, the resist can contain bubbles that will upon etching cause pin holes in active 2DEG regions. To avoid this we always cover our samples with resist before cutting a piece for fabrication. Small debris pieces from cutting then stick to the resist layer and can be removed easily in an acetone bath (with ultrasound for thorough cleaning). As GaAs/AlGaAs sample are very brittle a low ultrasonic power is used.

Ohmic contacts

Proper ohmic contacts to the 2DEG are important for measuring QPCs and similar devices. Their fabrication is depicted in Fig. 2.10c. We use 200 by 200 μm^2 contacts. To avoid edge currents around the ohmic contacts in magnetic field we make sure that the metallization for each ohmic contact crosses over a mesa boundary. For the Ohmic contacts we deposit 150 nm AuGe in the eutectic mixture of 88:12 wt%, 30 nm Ni and then a 20 nm layer of Au. We anneal these contacts at 450 °C either in a quartz tube oven or in a rapid thermal annealer (RTA) for an optimal time in a N_2 atmosphere to prevent oxidation. During the annealing process the Ge atoms diffuse towards the 2DEG and thus create a highly doped AlGaAs region between the metals on the surface and the 2DEG. Good ohmic contacts have a low resistance of only a few Ω (but contacts up to ~ 1 k Ω can be applied without problem) with a linear IV characteristic. A detailed study of ohmic contact formation can be found in *Chapter 6* and *Chapter 7*.

Fine gates

The fine gates are the actual QPC gates (Fig. 2.10d). This is the core of the device since the QPC properties will depend on the dimensions of these fine gates. Any error in the gate structure (or irregular metal-grain edges of the gates) will cause deviating transport properties. Optimal EBL resolution is therefore important for this step and we use here an e-beam acceleration voltage of 30 keV (other steps can be written at 10 keV). A 15 nm Au layer with a 5 nm Ti sticking layer is deposited for the fine gate structure at a slow deposition rate to make sure that layer is very smooth and that there are no abrupt grain boundaries. For sharp gate structures lift-off has to work out good, so a careful approach is adopted where the sample is left in heated acetone for several hours.

Large gates

The final step in our fabrication process is the deposition of the large gate structures (which connect to the fine gates) together with large bonding pads (positioned outside the QPC mesa). This step is shown in Fig. 2.10e. Here a 300 nm Au layer with 5 nm Ti sticking layer is used. The thick Au layer is required to overcome the step-edge at the mesa boundaries.

After this step the sample is cut into smaller pieces and each piece is glued on a chip carrier. Wire bonding is used for connecting the bonding pads to the metallization and pins of the chip carrier. The chip carrier can be mounted onto a sample holder on a dip stick (for use in a helium bath) or on the cold finger of a dilution refrigerator.

2.8 Low temperature measurement techniques

2.8.1 Low temperature measurements in a helium bath or dilution refrigerator

The research on ohmic contact formation used measurements at 4.2 K in a liquid ^4He vessel with a dip stick. The dip stick is first evacuated to about 10^{-3} mbar to avoid freezing upon cooling. The dip stick is then pre-cooled slowly to 77 K in liquid N_2 before further cooling in the liquid ^4He vessel.

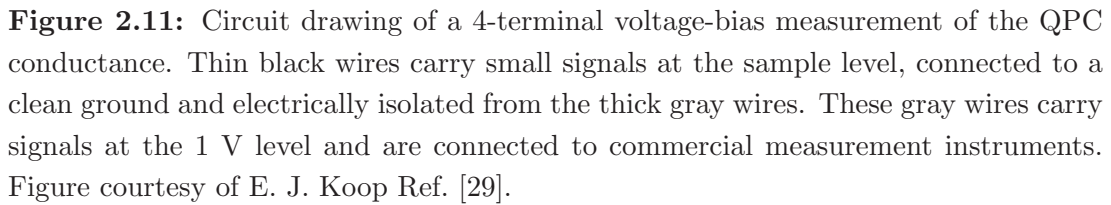
The measurement on QPCs were performed at temperatures ranging from 5 mK to 4.2 K. We used a $^3\text{He}/^4\text{He}$ dilution refrigerator with a cooling power of about 1 mW at 100 mK. With the combination of the $^3\text{He}/^4\text{He}$ mixture flow

and the heating power on the mixing chamber, the temperature of the cold finger could be stabilized at any desired value between 5 mK and 4.2 K. The dilution refrigerator was equipped with a 9 T superconducting magnet for the measurements in magnetic field. The setup had four sample holders anchored to the cold finger (mixing chamber) with 24 manganin wires (in twisted pairs) per sample holder. This allows for cooling down many devices at the same time. All 96 manganin wires run from the top of the insert to the cold finger. At the top of the insert all the wires are accessible via four 24-pin Fisher connectors. From these Fisher connectors all the devices on the samples are grounded (via a sample selection box) except for the one that is to be measured. The device that is to be measured is connected to a switch box from the sample selection box. To minimize the heat load from room temperature to the cold finger, the wires are thermally anchored at the 1K pot (~ 1.5 K), the still (~ 500 mK), at the cold plate (~ 50 mK) plate and at the mixing chamber. For filtering different frequencies, filters are installed at different positions along the wires. Wires are connected to the switch box through pi-filters that act as low-pass RFI feed through filters. Inside the dilution fridge the wires are passed through copper powder filters at the temperature of the mixing chamber. The stray capacitance and the resistance of the wires act as an RC filter that cuts off high-frequency noise. The cold finger that contains the samples is closed with three concentric copper cans that act as radiation shields.

2.8.2 Measurement scheme and electronics

The electrical transport properties described in this thesis are determined by applying a voltage and the measuring current through the device, or vice versa. For devices that are defined by surface gates like our QPCs, an additional dc voltage source is available for setting the gate voltages.

For the voltage-biased measurement we used an effective 4-probe scheme as shown in Fig. 2.11. Two additional probes are used to locally measure the actual voltage drop across the device so that the influence of series resistance contributions from the wiring, ohmic contacts, etc. can be circumvented. We still need to account for series resistance contributions from the 2DEG. This can be estimated given that we know the 2DEG square resistance, and we can check that the quantized conductance plateaus for QPCs appear at the integer values. The IV converter, V-source and Amplifier (A) as shown in the figure are part of the so-called *IVVI meetkast* which is a homemade measurement instrument. The



Two types of measurements are performed in our work. One is the linear conductance (or resistance) measurement, where we apply an ac excitation voltage V_{sd} such that $eV_{sd} < 4k_B T$. We used $V_{sd} = 10 \mu\text{V}$ (corresponding to $k_B T \approx 100 \text{ mK}$), close to the lowest effective electron temperature that could be realized with our measurement setup (80 mK). For nonlinear conductance measurements we applied a dc source-drain voltage in addition to the ac voltage. Both the resulting ac and dc current and voltage are recorded. The ac current and voltage are measured with two phase-locked SR830 lock-in amplifiers, typically at a frequency of 387 Hz for the QPC experiments. All our equipment is connected to a computer via a USB or GPIB interface for fast and automated measurements. Measurement programs are written in LabVIEW software.

Bibliography

- [1] B. J. van Wees *et al.*, Phys. Rev. Lett. **60**, 848 (1988).
- [2] D. A. Wharam *et al.*, J. Phys. C **21**, L209 (1988).
- [3] K.-F. Berggren, *et al.*, Phys. Rev. Lett. **57**, 1769 (1986).
- [4] K. J. Thomas *et al.*, Phys. Rev. Lett. **77**, 135 (1996).
- [5] K. J. Thomas *et al.*, Phys. Rev. B **58**, 4846 (1998).
- [6] K. J. Thomas *et al.*, Phys. Rev. B **61**, R13365 (2000).
- [7] N. T. Bagraev *et al.*, Phys. Rev. B **70**, 155315 (2004).
- [8] S. M. Frolov *et al.*, Phys. Rev. Lett. **102**, 116802 (2009).
- [9] Chuan-Kui Wang *et al.*, Phys. Rev. B. **54**, 14257 (1996).
- [10] Chuan-Kui Wang *et al.*, Phys. Rev. B. **57**, 4552 (1998).
- [11] D. J. Reilly *et al.*, Phys. Rev. Lett. **89**, 246801 (2002).
- [12] D. J. Reilly, Phys. Rev. B. **72**, 033309 (2005).
- [13] L. I. Glazman and A. V. Khaetskii, Europhys. Lett. **9**, 263 (1989).
- [14] S. M. Cronenwett, Ph.D. Thesis, Stanford University (2001).
- [15] R.M. Potok *et al.*, Phys. Rev. Lett. **89**, 266602 (2002).
- [16] L. P. Rokhinson *et al.*, Phys. Rev. Lett. **93**, 146601 (2004).
- [17] L. P. Rokhinson *et al.*, J. Phys.: Cond. Mat. **20**, 164212 (2008).
- [18] R. Crook *et al.*, Science **312** 1359 (2006).
- [19] P. Debray *et al.*, Nature Nanotechnology **4**, 759 (2009).
- [20] P. P. Das *et al.*, Appl. Phys. Lett. **99**, 122105 (2011).
- [21] S. M. Cronenwett *et al.*, Phys. Rev. Lett. **88**, 226805 (2002).
- [22] U. Meirav *et al.*, Phys. Rev. Lett. **65**, 771 (1990).
- [23] D. Goldhaber-Gordon *et al.*, Phys. Rev. Lett. **81**, 5225 (1998).
- [24] W. G. van der Wiel *et al.*, Science **289**, 2105 (2000).
- [25] J. Nygård *et al.*, Nature **408**, 342 (2000).
- [26] Y. Meir *et al.*, Phys. Rev. Lett. **70**, 2601 (1993).
- [27] T. A. Costi *et al.*, J. Phys.: Condens. Matter **6**, 2519 (1994).
- [28] E. J. Koop *et al.*, J. Supercond. Novel Magn. **20**, 433 (2007).

- [29] E. J. Koop, Ph. D. Thesis, University of Groningen (2008).
- [30] Y. Meir *et al.*, Phys. Rev. Lett. **89**, 196802 (2002).
- [31] K. Hirose *et al.*, Phys. Rev. Lett. **90**, 026804 (2003).
- [32] T. Rejec *et al.*, Nature **442**, 900 (2006).
- [33] S. Ihnatsenka *et al.*, Phys. Rev. B **76**, 045338 (2007).
- [34] A. A. Starikov *et al.*, Phys. Rev. B **67**, 235319 (2003).
- [35] K. F. Berggren *et al.*, J. Phys.: Condens. Matter **20**, 164203 (2008).
- [36] B. S. Shchamkhalova *et al.*, J. Phys.: Condens. Matter **19**, 156221 (2007).
- [37] A. D. Güçlü *et al.*, Phys. Rev. B **80**, R201302 (2009).
- [38] D. Goldhaber-Gordon *et al.*, Nature **391**, 156 (1998).
- [39] Sara M. Cronenwett *et al.*, Science **281**, 540 (1998).
- [40] N. Tombros *et al.*, Nat. Phys. **7**, 697 (2011).
- [41] J. Friedel, Adv. Phys. **3**, 446 (1954).
- [42] L. N. Pfeiffer *et al.*, Appl. Phys. Lett. **87**, 073111 (2004).
- [43] R. Danneau *et al.*, Appl. Phys. Lett. **88**, 012107 (2006).
- [44] V. T. Renard *et al.*, Phys. Rev. Lett. **100**, 186801 (2008).
- [45] R. Aguado *et al.*, Phys. Rev. Lett. **85**, 1946 (2000).
- [46] J. Bork *et al.*, Nat. Phys. **7**, 901 (2011).
- [47] J. Kondo, Prog. Theor. Phys. **32**, 37 (1964).
- [48] L. Kouwenhoven and L. Glazman, Physics World **14**, 33 (January 2001).
- [49] M. Hatzakis, J. Electrochem. Soc. **116**, 1033 (1969).
- [50] Y. Yoon *et al.*, Phys. Rev. Lett. **99**, 136805 (2007).
- [51] Y. Yoon *et al.*, J. Phys.: Condens. Matter **20**, 164216 (2008).
- [52] Y. Yoon *et al.*, Phys. Rev. B **79**, R121304 (2009).
- [53] Y. Yoon *et al.*, Appl. Phys. Lett. **94**, 213103 (2009).
- [54] K. M. Liu *et al.*, J. Phys. Conference Series **150**, 022052 (2009).
- [55] Y. Komijani *et al.*, Europhys. Lett. **91**, 67010 (2010).
- [56] Y. Ren *et al.*, Phys. Rev. B **82**, 045313 (2010).
- [57] E. Wigner *et al.*, Phys. Rev. **46**, 1002 (1934).

-
- [58] V. V. Deshpande *et al.*, Nat. Phys. **4**, 314 (2008).
 - [59] J. S. Meyer *et al.*, J. Phys. Condens. Matter **21**, 023203 (2009).
 - [60] K. A. Matveev *et al.*, Phys. Rev. Lett. **92**, 106801 (2004).
 - [61] For a recent review on the 0.7 anomaly see: A. P. Micolich, J. Phys.: Condens. Matter **22**, 443201 (2011).

Chapter 3

Many-body effects with signs of two-impurity Kondo Physics in QPCs with a fixed length

Abstract

This chapter presents results of measurements that studied how signatures of electron many-body effects in quantum point contacts (QPCs) behave as function of device geometry. Devices with fixed but different geometries were compared. The focus is on results from our team, and we review recently published data and new observations. The second part of this chapter presents experimental results from a QPC with a fixed device geometry, where the signatures of many-body effects showed similarities with the conductance for a two-impurity Kondo system. These results provide a first hint that many-body effects in QPCs can cause both single and paired self-consistent localized states. Such signatures were predicted but never reported till now.

This chapter is based on a reproduction and extension of work that was published as E. J. Koop *et al.*, J. Supercond. Novel Magn. **20**, 433 (2007). The new results will be published as Ref. 1 on p. 159.

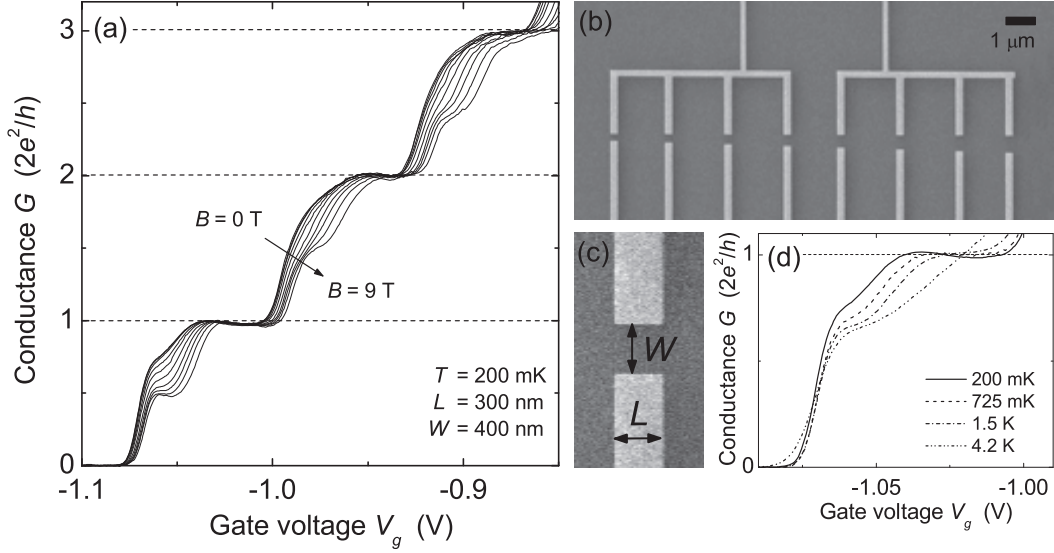


Figure 3.1: (a) Quantized conductance traces for different values of an in-plane magnetic field. (b) SEM image of a set of QPCs with a fixed length and variable width. (c) SEM image of a QPC with labels that define the length L and width W . (d) The evolution of the 0.7 anomaly with increasing temperature. Figure courtesy of E. J. Koop.

3.1 Introduction

In the previous chapter we discussed the two anomalous conductance features associated with the transport properties of a QPC, the 0.7 anomaly and the ZBA, and discussed the lack of consensus on the origin of these features (for a recent review see also Ref. [1]). We report in this chapter our experimental study of the dependence of these many-body phenomena on the QPC geometry. We measured many QPCs with fixed but different lengths and widths values for the QPC channel by varying the lithographic dimensions of the split-gates that define the QPC.

We found for our set of devices that quantized conductance is a robust property that shows a clean expression in nearly all devices, while the associated parameters like the pinch-off gate voltage V_{po} , subband spacing $\hbar\omega_{12}$ (the energy between the first and second 1D subband, which is a measure for the strength of the transverse confinement in the QPC channel), but also the effective g-factor $|g^*|$ show a regular dependence on device geometry. The pinch-off voltage is the value of the gate voltage V_g where the conductance starts to increase from zero.

The subband spacing is derived from transconductance data as in Fig. 3.2c (discussed later). These results show that our devices can be considered clean in the sense that most small device imperfections are too small for influencing the manifestation of the non-interacting electron physics that underlies the quantized conductance.

On the other hand, the parameters that characterize the many-body physics show a seemingly random dependence on the dimensions of the QPC, and strongly fluctuating values in a set of nominally identical QPCs. These parameters include the peak width and height of the ZBA, the behavior of the ZBA in magnetic field and as a function of temperature, and an apparent energy splitting for the 0.7 anomaly. Apparently, the many-body physics is very sensitive to small device imperfections like the weak influence of remote impurities and defects in the QPC environment and small lithographical errors. Previously, the g-factor enhancement was also attributed to many-body effects [7, 8]. Our studies of the sensitivity of these effects to small device imperfections thus show in fact that the many-body effects that underlie the g-factor enhancement and those of the 0.7 anomaly and the ZBA have different origins.

We report in the second half of this chapter on the observation of a double-peak ZBA in a QPC device with fixed length and width. While we present such results from many QPCs in *Chapter 4*, we present here a detailed analysis of the behavior of the double-peak ZBA as a function of various control parameters for one particular QPC. The control parameters are temperature, magnetic field and a sideways shift of the QPC channel in the material. The double-peak ZBA in QPCs can be interpreted as a signature of the predicted two-impurity Kondo physics for QPCs [13]. Such signatures were sometimes observed by other groups as well (see for example Ref. [3]) but further studies of it were not carried out since they were assumed to result from defects in the device structure [4].

3.2 Experimental realization

We fabricated our devices on two types of GaAs/AlGaAs heterostructures (see also p. 73). One was a GaAs/Al_{0.32}Ga_{0.68}As system with the 2DEG at 114 nm depth. The other was a GaAs/Al_{0.35}Ga_{0.65}As material with the 2DEG at 110 nm depth. At 4.2 K the mobility of the 2DEG for the two materials was $\mu = 159 \text{ m}^2/\text{Vs}$ and $\mu = 118 \text{ m}^2/\text{Vs}$, respectively, and the density was $n_{2D} = 1.5 \cdot 10^{15} \text{ m}^{-2}$ and $n_{2D} = 1.6 \cdot 10^{15} \text{ m}^{-2}$, respectively. For an overview of the experimental techniques see the general introduction in *Chapter 2* and the de-

Device 1								
L (nm)	100	150	200	250	300	350	400	450
W (nm)	350	350	350	350	350	350	350	350
Device 2								
L (nm)	300	300	300	300	300	300	300	300
W (nm)	200	250	300	350	400	450	500	550

Table 3.1: Dimensions of the QPCs that were measured. For the definitions of length L and width W see Fig. 3.1c.

tailed description on p. 73.

Table 3.1 shows the nominal dimensions of the QPCs that were used in this study. In order to make the comparison valid all QPCs were fabricated on a single piece of wafer material in close proximity of each other. The device set with fixed width W and variable length L , and the set with fixed length and variable width are labeled as devices 1 and devices 2 respectively. Post-measurement SEM inspection of the devices confirmed that dimensions of all the devices were within 10 nm of the nominal values for length and width.

3.3 Part I: Correlations between QPC transport properties and geometry

In this section we present the dependence of the QPC transport properties on the QPC geometry (see Table 3.1). These properties include the pinch-off voltage V_{po} , the subband spacing $\hbar\omega_{12}$ (between the first and second 1D subband) and the effective g-factor $|g^*|$. Parameters for characterizing the 0.7 anomaly and the ZBA are the high-field offset ΔE_{hfo} , the *apparent* energy splitting for the 0.7 anomaly $\Delta E_{0.7}$, the peak width and height of the ZBA, and the magnetic field and temperature dependence of the ZBA. These are further introduced below.

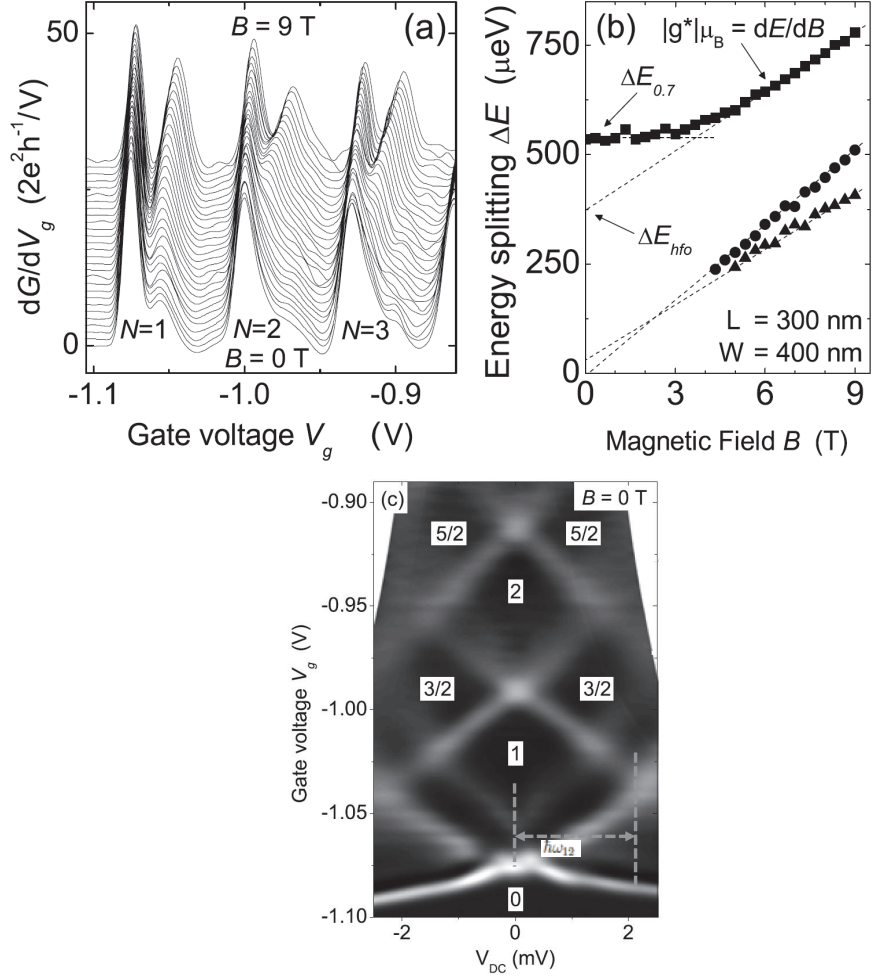


Figure 3.2: (a) Transconductance dG/dV_g traces for three subbands for increasing magnetic field, obtained by differentiating the traces in Fig. 3.1a. The traces are offset vertically for clarity. The 0.7 anomaly can be seen as a small side peak for the $N = 1$ subband at zero magnetic field. (b) Intra-subband energy splittings ΔE for the subbands $N = 1$ (squares), $N = 2$ (circles) and $N = 3$ (triangles) as a function of magnetic field for the data shown in (a). Three parameters, namely the effective g-factor $|g^*|$, the high-field offset ΔE_{hfo} and the apparent energy splitting for the 0.7 anomaly $\Delta E_{0.7}$ are extracted from this kind of plot for characterizing the many-body effects. (c) Gray-scale transconductance (dG/dV_g) plot as a function of gate voltage V_g and source-drain voltage V_{DC} at zero magnetic field. Bright spots at zero source-drain voltage are the transconductance peaks of (a). The crossings of these peaks at higher source-drain voltage give values for the subband spacings (see main text). Figure courtesy of E. J. Koop.

3.3.1 Correlations found for pinch-off voltage, subband splitting and effective g-factor

Here we first discuss how various parameters for quantitatively characterizing the quantized-conductance traces and the many-body effects are derived from experimental data. This is used for showing a clear correlation between the device geometry and the pinch-off voltage, the subband splitting and the effective g-factor.

Figure 3.2a shows transconductance (dG/dV_g) traces for a QPC with $L = 300$ nm, $W = 400$ nm at different magnetic field values, obtained from the traces in Fig. 3.1a. For zero magnetic field, the peaks in the transconductance as a function of increasing V_g reflect the onset of a next spin-degenerate subband. At high magnetic field, each peak reflects the onset of a next spin-polarized subband. The transconductance is zero (or very low) where quantized conductance plateaus appear. At zero magnetic field a small side peak for the first subband ($N = 1$) appears due to the 0.7 feature. This small peak splits further and grows in strength with the increasing magnetic field. Figure 3.2b shows the intra-subband energy splittings between the spin-up and spin-down subbands as a function of magnetic field, for the three lowest (spin-degenerate) subbands (as labeled with N). For the first $N = 1$ subband the 0.7 anomaly thus appears as an apparent energy splitting for zero field, that remains constant for low field values and then splits linearly with further increasing the magnetic field. For the analysis in this chapter, this zero-field splitting is discussed as an *apparent* energy splitting for the first subband (labeled as $\Delta E_{0.7}$) because we are not certain whether the underlying physics concerns indeed an actual energy splitting. Another parameter that is extracted from such plots is the high-field offset ΔE_{hfo} . This quantifies a deviation from a purely linear Zeeman splitting at high field (see Fig. 3.2b). The *slope* of the Zeeman splitting at high field is used for extracting an effective g-factor as $|g^*| = \frac{1}{\mu_B} \frac{d\Delta E}{dB}$.

Figure 3.2c shows in gray-scale the transconductance dG/dV_g as a function of both gate voltage and source-drain voltage (in this plot labeled as V_{DC} instead of V_{sd}). We used this type of plots for deriving the subband spacing $\hbar\omega_{12}$ [3, 11]. The dark regions (low transconductance) here reflect the quantized conductance plateaus and the bright lines (high transconductance) reflect the transitions (steps) between plateaus. The bright spots at zero source-drain voltage correspond to the transconductance peaks in Fig. 3.2a for zero magnetic field. At crossings of two consecutive bright transconductance lines, the source-drain volt-

age equals the energy spacing between two subsequent 1D subband, as indicated in the plot for $\hbar\omega_{12}$.

Figure 3.3 shows the dependence of the pinch-off voltage V_{po} , subband energy splitting $\hbar\omega_{12}$ and effective g-factor $|g^*|$ on device geometry. A clear correlation is found for these properties. Figures 3.3a,b show the pinch-off voltage V_{po} as a function of QPC length (for fixed width) and QPC width (for fixed length), respectively. For shorter and wider QPCs, the pinch-off voltage V_{po} is more negative and vice versa. For wider QPCs the center of the channel is farther away from the ends of the gate electrodes, so a more negative voltage is required to pinch the channel off. Similarly, shorter QPCs require a more negative voltage for fully closing the QPC.

Figures 3.3c,d show the subband energy splittings $\hbar\omega_{12}$ as a function of length and width. For shorter and narrower QPCs the subband spacing $\hbar\omega_{12}$ is higher and vice versa, provided that $W \gtrsim 3d$, where W is the width of the QPC and d is the depth of the 2DEG. For smaller W this relation breaks down, in agreement with electrostatics (discussed below). In our case the 2DEG depth is 114 nm so the general trend should hold for $W \gtrsim 350$ nm, in agreement with the observations.

Figures 3.3e,f show the subband spacing $\hbar\omega_{12}$ as a function of length and width, as calculated with the electrostatic model developed by Davies *et al.* [9] (see also *Chapter 5*). The trend observed for the subband spacing $\hbar\omega_{12}$ in Figs. 3.3e,f qualitatively agrees with the experimental values in Figs. 3.3c,d. The calculated subband spacing $\hbar\omega_{12}$ (Fig. 3.3f) shows a maximum at $W \approx 2d$ whereas for the experimental data (Fig. 3.3d) the maximum is observed at $W \approx 3d$. Davies *et al.* [9] showed that a maximum in $\hbar\omega_{12}$ shifts from $W \approx 2d$ to $W \approx 3d$ when a more advanced method for the boundary conditions on the wafer surface is applied. We thus conclude that we obtain good agreement between the calculations and the experimental observations [5].

Figures 3.3g,f show the variation of the effective g-factor with the device geometry for the first subband (the effective g-factor $|g^*|$ is different for different subbands [8]). The effective g-factor $|g^*|$ shows a regular variation in its dependence on the QPC geometry, with a trend that is very similar to that of $\hbar\omega_{12}$ in Figs. 3.3c,d, which shows that the effective g-factor $|g^*|$ is more enhanced for stronger transverse confinement. The enhancement in g-factor is attributed to many-body effects [7, 8]. For the data in Fig. 3.3 only the g-factor $|g^*|$ enhancement concerns a many-body effect, and it turns out to be the only signature of many-body physics that shows a regular dependence on QPC geometry.

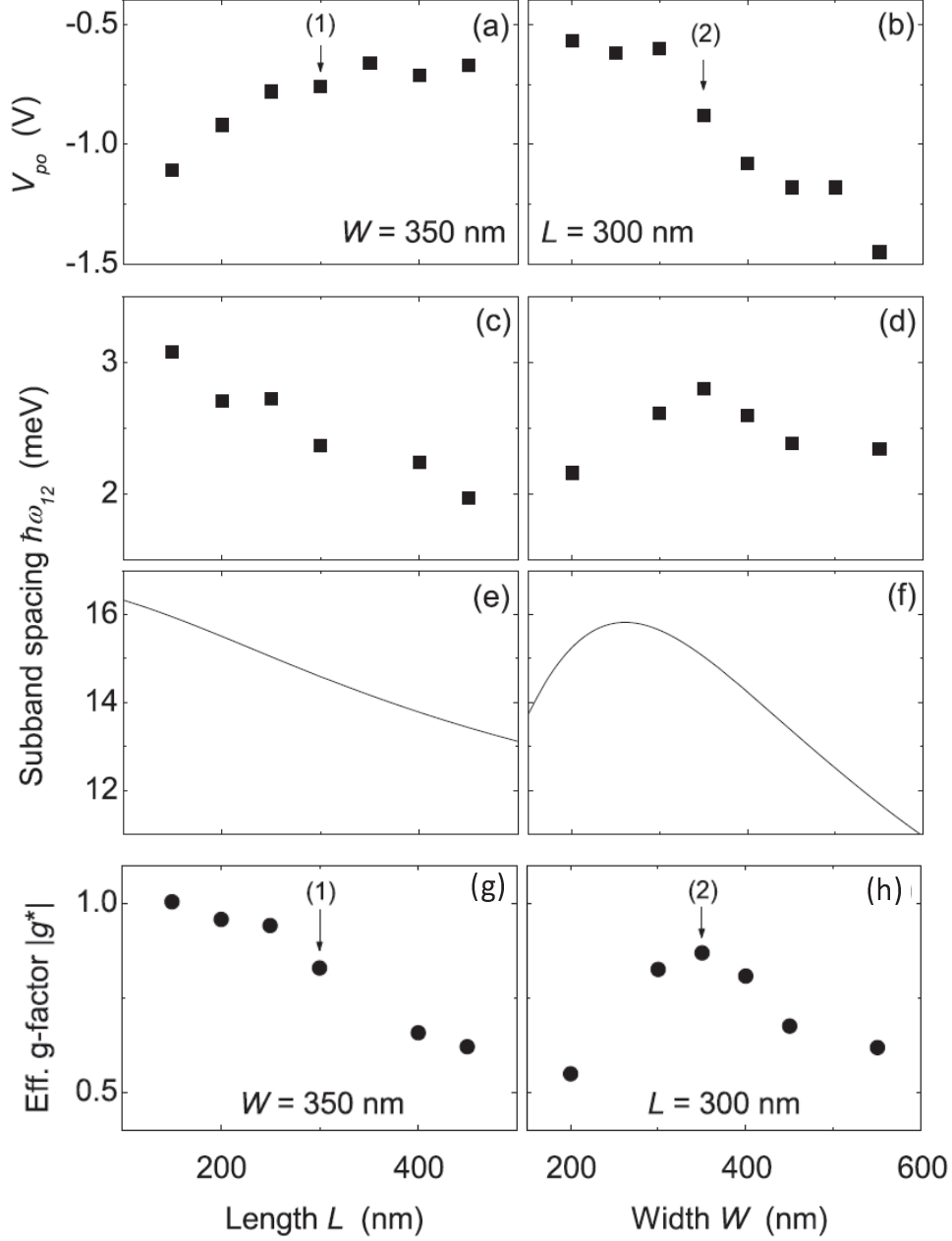


Figure 3.3: (a),(b) Pinch-off voltage V_{po} as a function of length L (at fixed width) and width W (at fixed length). (c),(d) Measured subband spacings $\hbar\omega_{12}$ as a function of L and W . (e),(f) Subband spacings $\hbar\omega_{12}$ as in (c) and (d), calculated with an electrostatic model. (g),(h) Measured values of the effective g-factor $|g^*|$ for the first subband as a function of L and W . Figure courtesy of E. J. Koop.

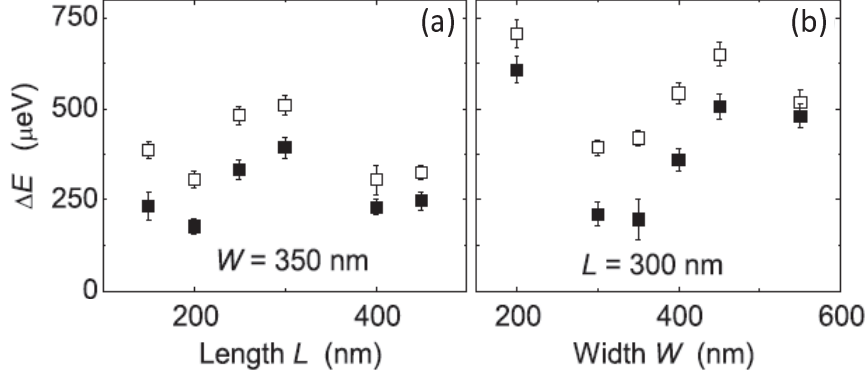


Figure 3.4: The parameters ΔE_{hfo} (solid squares) and the apparent energy splitting for the 0.7 anomaly $\Delta E_{0.7}$ (open squares) as a function of length L (at fixed width) (a) and width W (at fixed length) (b) for the first subband ($N = 1$). Figure courtesy of E. J. Koop.

3.3.2 Correlation not found for the 0.7 anomaly and ZBA

We next focus on the correlations between the device geometry and the many-body effects that appear as the 0.7 anomaly and the ZBA. Figs. 3.4a,b show the apparent energy splitting for the 0.7 anomaly $\Delta E_{0.7}$ for zero field (open squares) and the high-field offset ΔE_{hfo} (solid squares) for the first subband ($N = 1$), as a function of length and width. Both $\Delta E_{0.7}$ and ΔE_{hfo} show strong variations but this variation shows no correlation with the length or width of the QPCs. Notably, the two parameters are correlated to each other. This indicates that the effects that causes the high-field offset and the 0.7 anomaly have a common origin.

In Fig. 3.5 we focus on the behavior of the ZBA. Figure 3.5a shows the temperature dependence of the ZBA. With increasing temperature the ZBA gets suppressed. Figures 3.5b-d present the dependence of the ZBA on applied magnetic field (in-plane), and shows a collapse of the ZBA for all conductance levels. Similar data from Cronenwett *et al.* [10] showed a splitting of the ZBA in magnetic field at conductance levels near $0.7 \times 2e^2/h$. For higher and lower conductance values they also observed a collapses without splitting. The splitting of the ZBA in magnetic field was interpreted as a signature of the Kondo effect [10], and the absence of the splitting for the higher conductance regime (Fig. 3.5b) could be attributed to having a Kondo temperature that is much stronger than the Zeeman splitting [14, 10]. For the lower conductance values (Figs. 3.5c,d) it is not clear

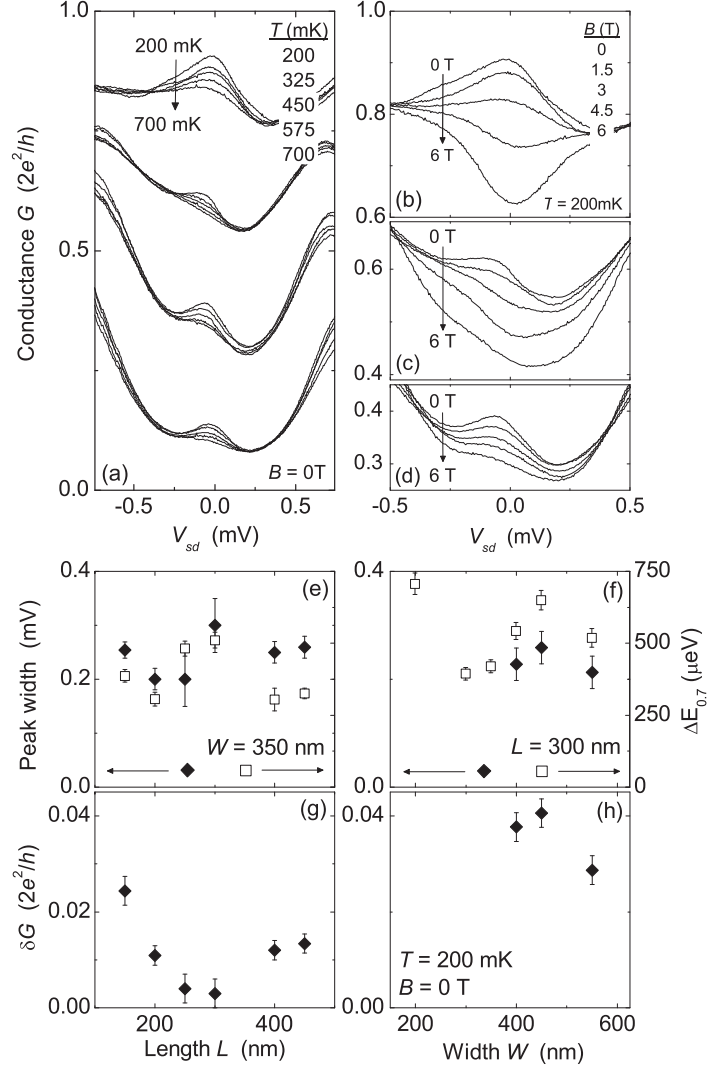


Figure 3.5: (a) The ZBA at different conductance values for different temperatures. The height of the ZBA decreases with increasing the temperature. (b)-(d) The ZBA for three conductance levels (high, intermediate and low) for increasing magnetic field values. No splitting of the ZBAs is observed. Instead, it collapses with increasing magnetic field. (e),(f) ZBA peak width (left axis, filled diamonds) and the apparent energy splitting for the 0.7 anomaly $\Delta E_{0.7}$ (right axis, open squares) as a function of L (e) and width W (f). (g),(h) Peak height δG as a function of L (g) and width W (h). The data in (e)-(h) is for a conductance value at $0.3 \times 2e^2/h$. A few data points in (h) are missing due to malfunctioning of the QPC at a late stage of the measurements. Figure courtesy of E. J. Koop.

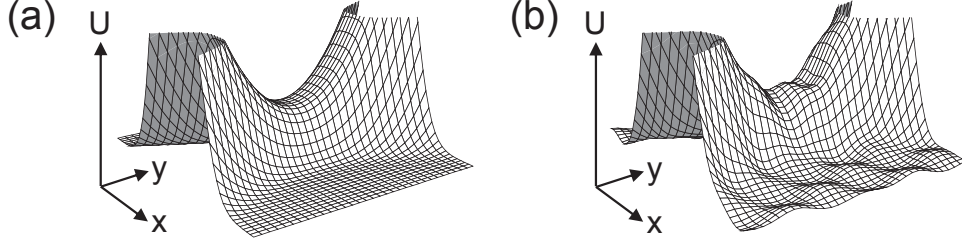


Figure 3.6: Saddle-point potentials as in Fig. 2.2b that illustrate the presence of weak static fluctuations on the potential. (a) shows an ideal potential, (b) illustrates the influence of remote impurities and defects, and small nanofabrication errors, that are always present in real devices.

how the absence of a splitting can be explained within a Kondo interpretation.

Figures 3.5e,f show the peak width of the ZBA at $\sim 0.3 \times 2e^2/h$ (left axes for filled diamonds) as a function of length and width. Since it is of interest to explore the correlations between the ZBA and the 0.7 anomaly we also plot $\Delta E_{0.7}$ in the same graph (right axes for open squares). While both parameters do show fluctuations without a regular dependence on geometry, the results indicate indeed a correlation between the ZBA peak width and $\Delta E_{0.7}$. We have also characterized the peak height δG of the ZBA at the same conductance level ($\sim 0.3 \times 2e^2/h$), see Figs. 3.5g,h (a few data points are missing due to malfunctioning of some QPCs during a late stage of the measurements). The peak height δG also does not show any clear dependence on device geometry (length or width).

3.3.3 Summary of Part I

We have studied the QPC transport properties as a function of the QPC device geometry (length and width). The regular variation of the pinch-off voltage V_{po} and subband spacing $\hbar\omega_{12}$ indicate that we have a set of QPCs with device imperfections at a level that is low enough for not strongly influencing the physics that is observed as quantized conductance. At the same time, the parameters that characterize the 0.7 anomaly and the ZBA show strong device-to-device fluctuations without a regular correlation with the device geometry. This shows that the many-body physics that underlies these signatures is highly sensitive to small details of the devices, lithographic errors and remote impurities and defects in the environment of the QPC channel (see also Fig. 3.6).

3.4 Part II: Observation of a double-peak ZBA

In this section we highlight the observation of a ZBA with double-peak character in one particular QPC with fixed dimensions ($L = 200$ nm, $W = 350$ nm). The double-peak ZBA has been predicted [13] for QPCs that contain a pair of self-consistent localized states. A trademark for the Kondo effect with such a pair of localized states is a double-peak ZBA due to the competition between the Kondo effect for each spin and the anti-ferromagnetic coupling between the two spins [16, 17, 18]. We study in this section to what extent the observed double-peak ZBA reflects the properties of the two-impurity Kondo model. We will also link this analysis to the parameters for characterizing many-body physics $|g^*|$, $\Delta E_{0.7}$ and ΔE_{hfo} (introduced in the previous section).

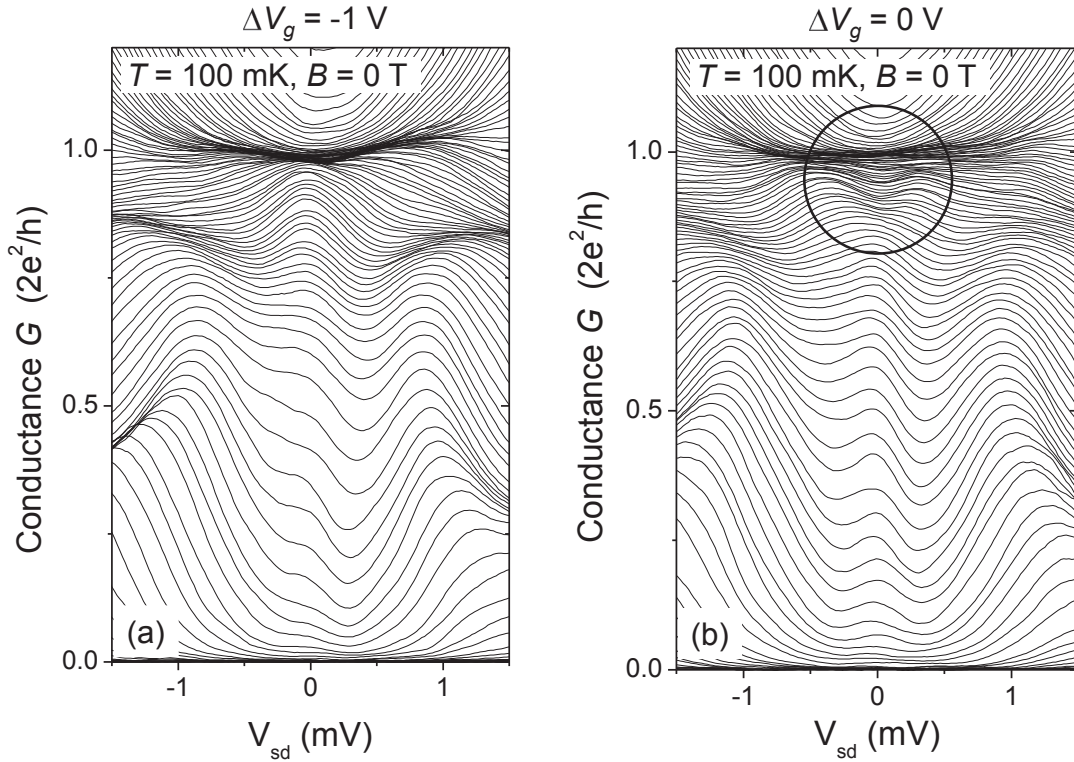


Figure 3.7: Non-linear differential conductance for (a) $\Delta V_g = -1$ V (QPC channel shifted sideways with respect to the middle between the split-gate electrodes) and (b) $\Delta V_g = 0$ V (QPC channel positioned in the middle between the split-gate electrodes). In (b) a double-peak ZBA is observed just below the first conductance plateau which evolves into a single-peak ZBA when shifting the QPC channel to the position as in (a).

3.4.1 Tuning between single and double-peak ZBA

Figures 3.7a,b show nonlinear conductance results for the QPC that we study in this section. The double-peak ZBA appears in the plot Fig. 3.7b just below the first conductance plateau (marked with the circle). The two plots in Fig. 3.7 illustrate that the ZBA at this conductance level can in fact be tuned between single (left) and double-peak ZBA (right). This occurs upon sideways shifting of the QPC channel position in the material by applying asymmetric gate voltages on the two gate fingers of the QPC (denoted by $\Delta V_g = V_{gLeft} - V_{gRight}$). The left plot is for $\Delta V_g = -1$ V and the right plot is for $\Delta V_g = 0$ V. In other fixed-geometry QPCs we observed that the double-peak ZBA can in fact appear anywhere between zero conductance and the first conductance plateau (and also between higher plateaus). This is presented in *Chapter 4*.

Figure 3.8 presents a more detailed analysis of the tuning between the single and double-peak ZBA by shifting of the channel position. Note that shifting the channel in the opposite direction ($\Delta V_g = +0.5$ V) does not cause a single-peak peak ZBA. Instead, the ZBA evolves into a double-peak ZBA with more asymmetric peaks (Fig. 3.8c). The ΔV_g tuning of the ZBA is very regular for all conductance levels (Fig. 3.8b). Notably, the quantized conductance traces (linear conductance) showed (besides a weak modulation of the 0.7 anomaly) no significant dependence of the channel position.

For this study we cannot rule out a role for weak fluctuations on the QPC saddle-point potential as in Fig. 3.6. With such fluctuations from the material background, shifting the channel corresponds to tuning of weak structure on the potential (bottom) of the channel, and thereby also to minor tuning of the QPC channel length. It is also interesting to consider whether small differences between the dimensions of the two gate fingers can cause minor tuning of the channel length, given the study with length-tunable QPCs that is presented in the next chapter. In that case the length parameter L for the gate electrodes on either side the channel would have to be slightly different (for example due to minor lithography errors), and sideways shifting of the channel then corresponds indeed with minor tuning of the QPC channel length. Post-measurement SEM inspection of the device that is measured here revealed indeed a difference of about 10 nm for L of the two gates.

Figure 3.8a shows that the peak spacing (derived from fitting two Gaussians to the double-peak ZBAs) is independent of temperature. Increasing the temperature only changes the peak heights. Smaller double-peak ZBAs (at lower conductance values in this case) start to disappear already at less elevated tem-

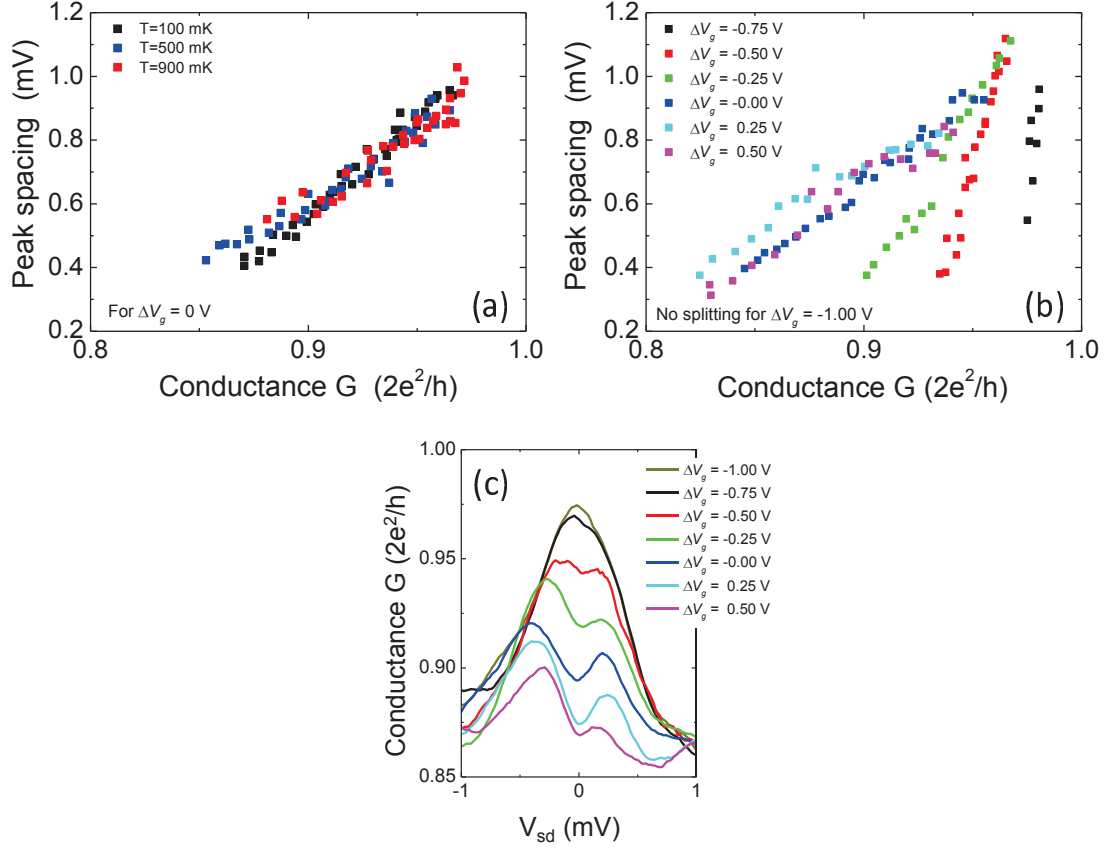


Figure 3.8: Peak spacings for the double-peak ZBA as a function of channel shift and temperature. **(a)** Peak spacing for 3 different temperatures as a function of conductance at $\Delta V_g = 0$ V. **(b)** Peak spacing for various values of ΔV_g at 100 mK. **(c)** Evolution of a double-peak ZBA for various values of ΔV_g at a fixed level of conductance (evaluated next to the ZBA at $V_{sd} = 1$ mV). Data for the device of Fig. 3.7.

peratures. This behavior is in fact consistent with the Kondo scenario [10, 12, 13] for two self-consistent localized states, where the distance between the peaks is set by the spin-spin interaction strength, and a higher Kondo temperature for each localized state results in a more pronounced (in particular wider) ZBA sub-peak (see also the quantum dot data in Ref. [20]). For the case where we tuned to a single-peak ZBA, we carried out a Kondo scaling analysis as worked out by Cronenwett *et al.* [10] (plot not shown). We obtained a similar level of agreement as Cronenwett *et al.* when scaling with the modified scaling law Eq. 2.11.

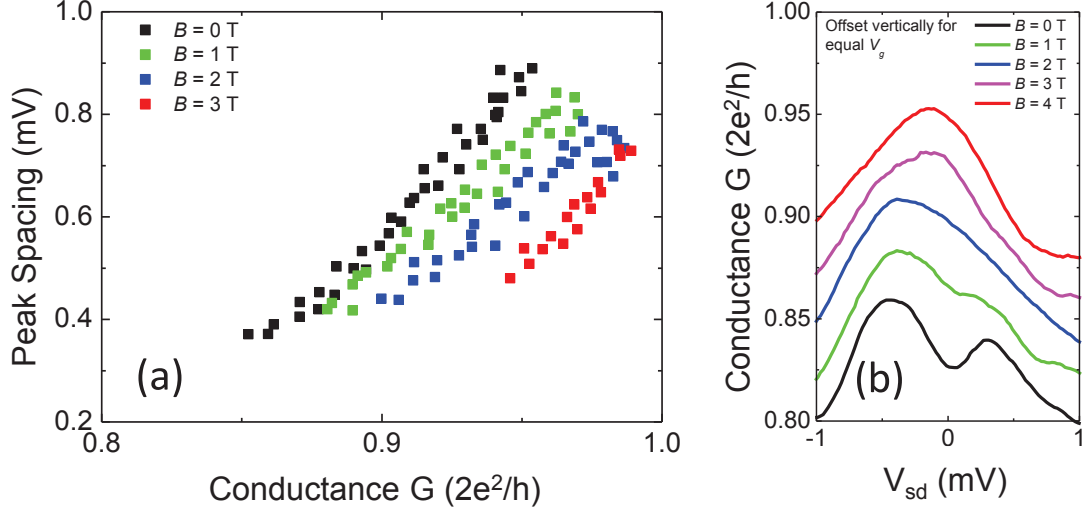


Figure 3.9: ZBA peak spacing and peak evolution as a function of in-plane magnetic field. (a) Peak spacings for the double-peak ZBA for different in-plane magnetic field values. The larger peak spacings at zero field require a stronger field for reducing the peak spacing to zero. (b) Evolution of the double-peak ZBA with increasing magnetic field (traces for 3 T and lower are offset vertically for clarity). When increasing the magnetic field in the range 4 T-9 T the ZBA remains a single peak (data not shown) with traces similar as for 4 T. Data for the device of Fig. 3.7 at $\Delta V_g = 0$ V.

3.4.2 Magnetic field dependence of the double-peak ZBA

Figure 3.9 present the dependence of this double-peak ZBA on in-plane magnetic field. All the data in this figure is for $\Delta V_g = 0$ V. With increasing magnetic field the peak spacing for the double-peak ZBA decreases, and eventually transform into a single-peak ZBA. A stronger zero-field splitting requires a stronger field for the transition into a single-peak ZBA. In a Kondo scenario, the peak spacing between the two peaks in the double-peak ZBA is a measure for the strength of the coupling between the spins of the two self-consistent localized states, and the value of the magnetic-field energy needed for turning the double-peak ZBA into a single-peak ZBA should be of the order of this peak-spacing energy [19]. In our case, estimating the coupling (J) between the two localized spin states as half the peak separation gives $\sim 420 \mu\text{eV}$. The magnetic field to suppress the double-peak ZBA should then be $B = J/(g\mu_B)$ which is ~ 3 T, in good agreement with the data in Fig. 3.9b.

3.4.3 Correlation with the parameters $|g^*|$, $\Delta E_{0.7}$ and ΔE_{hfo}

In this section we analyze for this device the parameters for the effective g-factor $|g^*|$, the apparent energy splitting for 0.7 anomaly $\Delta E_{0.7}$ and the high-field offset ΔE_{hfo} , and their dependence on shifting the channel position. The results are presented in Fig. 3.10. For the effective g-factor $|g^*|$ (extracted as for Fig. 3.3g,h) there is no significant change when shifting the channel. In the case of Fig. 3.3g,h the effective g-factor $|g^*|$ only showed a dependence on the device geometry when the length and width of QPC devices were varied over a wide range. For the data in Fig. 3.10a, the effective change in the length and width of the QPC is at most about 10 nm. These results are therefore consistent.

The parameters $\Delta E_{0.7}$ and ΔE_{hfo} do show a strong variation upon sideways shifting of the channel. The change is here gradual, but it still confirms that these parameters are very sensitive to small changes on the QPC saddle-point potential. Note that the two parameters are also correlated to each other for this data set. It is less obvious whether these parameters show a correlation with the character of the ZBA (single versus double peak). Here $\Delta E_{0.7}$ and ΔE_{hfo} get lower during the transition from single- to double peak ZBA, but preliminary results from other devices show in some cases the opposite trend (data not shown here).

3.4.4 Summary of Part II

Part II reported our first observation and in depth study of a double-peak ZBA for transport through a QPC. The temperature and magnetic field dependence show agreement with the scenario where the double-peak ZBA is interpreted as the signature of having two self-consistent localized states in the QPC channel. The transport then shows the characteristics of the two-impurity Kondo model. Sideways shifting of the QPC channel in the material confirmed that the many-body physics that underlies the 0.7 anomaly and the ZBA is very sensitive to very small changes on the QPC saddle-point potential. By shifting the channel the ZBA can be tuned from single peak to double peak, and such tuning also modulates the 0.7 anomaly. The appearance of quantized conductance, however, does not change significantly upon such channel shifting. This shows that in-depth studies of the dependence of these effects on the QPC device geometry needs ultra-clean QPCs realized with ultra-precise nano-fabrication. Alternatively, one could use an approach with QPCs that are compatible with very gradual tuning of the channel length without causing a channel shift. In *Chapter 4* and *Chap-*

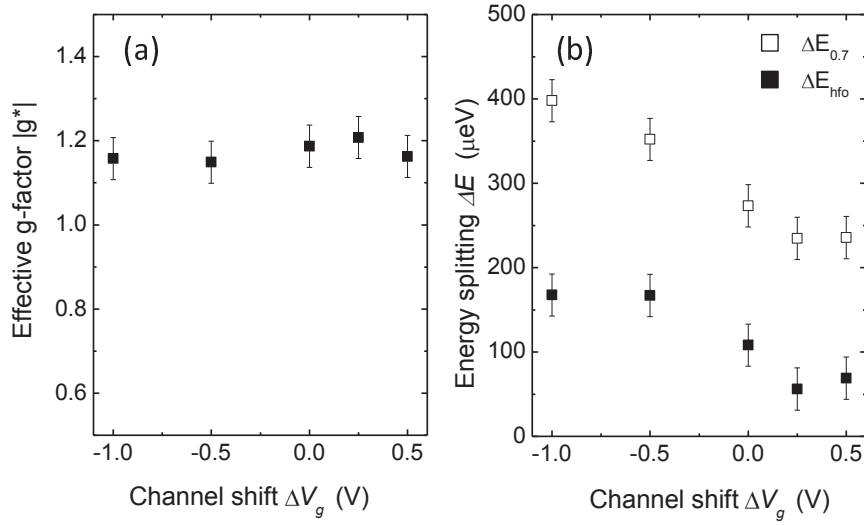


Figure 3.10: Effective g-factor and the energy splitting parameters $\Delta E_{0.7}$ and ΔE_{hfo} as a function of channel shift (ΔV_g value). (a) The effective g-factor does not change significantly when shifting the channel sideways. (b). The parameters ΔE_{hfo} and the apparent energy splitting for 0.7 anomaly $\Delta E_{0.7}$ show strong dependence on channel shift. Data for the device of Fig. 3.7.

ter 5 we work out this latter option with studies on QPCs with an *in-situ* tunable length for the channel.

Bibliography

- [1] A. P. Micolich, J. Phys.: Condens. Matter **22**, 443201 (2011).
- [2] T. Rejec *et al.*, Nature **442**, 900 (2006).
- [3] S. M. Cronenwett, Ph. D. Thesis, Stanford University (2001).
- [4] Personal communication with Yigal Meir where he mentioned the views of the Charlie Marcus on the double-peak ZBA observed in one of their QPC devices (Ref. [3]).
- [5] E. J. Koop *et al.*, J. Supercond. Novel Magn. **20**, 433 (2007).
- [6] E. J. Koop, Ph. D. Thesis, University of Groningen (2008).
- [7] Chuan-Kui Wang *et al.*, Phys. Rev. B. **54**, 14257 (1996).
- [8] K. J. Thomas *et al.*, Phys. Rev. B **58**, 4846 (1998).

- [9] J. H. Davies and I. A. Larkin, J. Appl. Phys. **77**, 4504 (1995).
- [10] S. M. Cronenwett *et al.*, Phys. Rev. Lett. **88**, 226805 (2002).
- [11] N. J. Curson *et al.*, Appl. Phys. Lett. **78**, 3466 (2001).
- [12] Y. Meir *et al.*, Phys. Rev. Lett. **89**, 196802 (2002).
- [13] T. Rejec *et al.*, Nature **442**, 900 (2006).
- [14] S. M. Cronenwett *et al.*, Science **281** 540 (1998) .
- [15] W. G. van der Wiel *et al.*, Science **289** 2105 (2000).
- [16] R. Aguado *et al.*, Phys. Rev. Lett. **85**, 1946 (2000).
- [17] H. Jeong *et al.*, Science **293**, 2221-2223 (2001).
- [18] J. Bork *et al.*, Nat. Phys. **7**, 901 (2011).
- [19] H. B. Heersche *et al.*, Phys. Rev. Lett. **96**, 017205 (2006).
- [20] N. J. Craig *et al.*, Science **304**, 565 (2004).

Chapter 4

Emergent impurity states from many-body physics in clean quantum point contacts

Abstract

Quantum point contacts (QPCs) are the ultimate building blocks for controlling nanoscale electron transport. However, electron many-body effects have a significant influence on the QPC conductance. Understanding is here incomplete and the so-called 0.7 anomaly in quantized conductance traces is a topic of debate. We discovered an operation regime where transport around the 0.7 anomaly shows signatures of both single- and two-impurity Kondo physics. For a systematic study of these effects we developed length-tunable QPCs. Here the 0.7 anomaly and Kondo signatures both show a periodic modulation as a function of QPC length. Our results demonstrate that Friedel oscillations and emergent impurity states from many-body physics are fundamental to these phenomena, and that tunable QPCs offer a rich platform for investigating many-body effects.

This chapter is based on Ref. 2 on p. 159.

4.1 Introduction

A quantum point contact (QPC) is a short and narrow transport channel between two electron reservoirs and thereby one of the most basic nano-electronic devices. In clean channels electron transport is ballistic and the conductance as a function of channel width is then quantized [1, 2] with plateaus at integer multiples of $2e^2/h$ (e is the electron charge and h Planck's constant). This can be understood in a picture where the electron states are propagating waves, without a need to account for electron-electron interactions. Quantized conductance can thus be seen as the signature of ultimate control over electron transport at the nanoscale. However, even studies with the cleanest QPCs generically show significant anomalies on quantized conductance traces and there is consensus that these result from electron many-body effects [3, 4]. Despite extensive experimental and theoretical studies since 1996 [4], understanding is here incomplete. These phenomena thus provide a test for fundamental understanding in solid-state physics and better insight is key for assessing the role of QPCs in proposals for spintronic and quantum information applications [5, 6, 7].

There are two signatures of many-body physics that are generically observed for a wide variety of QPCs, which includes systems in GaAs [3], Si [9], graphene [10], and both for electron and hole transport [8, 9]. First, the quantized conductance traces often show the so-called 0.7 anomaly: an additional small plateau at about $0.7 \cdot (2e^2/h)$. Second, as a function of bias voltage across the channel the conductance G typically shows a peak around zero bias (hence named Zero-Bias Anomaly, ZBA) at conductance levels between quantized plateaus. We report here experimental evidence that these signatures result from an electron many-body state with one or more localized electrons in the channel. This is a remarkable phenomenon since a QPC is a fully open quantum system. To avoid confusion with localization by an atomic impurity, these many-body states carry the name self-consistent localized states or emergent impurity states.

Such many-body states were proposed in theoretical work [15, 16] that was inspired by the experimental observation [11] that the ZBA and the 0.7 anomaly had similarities with the Kondo effect for quantum dots (transport through a single localized electron state [12, 13]). This theoretical work developed the picture that the many-body effects in QPC channels are intimately related with the occurrence of a Friedel oscillation (an oscillation in the electron charge density that occurs when electron waves get reflected in a partially open QPC channel), which gets enhanced into a localized state with about one electron of charge

due to Coulomb repulsion and exchange interactions between electrons. In turn, transport through such a state can carry signatures of the Kondo effect [21]. This theoretical work also predicted that these effects can yield a pair of localized states in the channel. This would result in a double-peak ZBA (earlier observed as the two-impurity Kondo effect in double quantum dots [14]) instead of a single-peak ZBA, but till now such double-peak ZBAs were not reported for QPCs. We present here results from observing and studying such double-peak ZBAs in a large number of QPCs. In what follows, we present how the 0.7 anomaly and single-peak and double-peak ZBAs appeared in our QPCs, which includes results from a new type of QPC which has a tunable channel length. In these latter devices the 0.7 anomaly and ZBA showed a periodic modulation as a function of QPC length. For analysis of these results we introduce an extension of the theoretical work [16] that predicted the formation of self-consistent localized states.

4.2 Experimental

We realized QPCs by locally depleting the two-dimensional electron gas (2DEG) below the surface of a GaAs/AlGaAs heterostructure (see Supporting Appendix Material (SAM, starting at p. 73) Section 4.6 for details). Applying negative voltage to two metallic gate fingers on the surface of such material (Fig. 4.1A) induces an electrostatic potential barrier between a source and drain reservoir in the 2DEG, with a small tunable opening in the form of a saddle-point potential (Fig. 4.2B). Such devices with two gate fingers will be denoted as QPC_{2F} and these have a fixed length L for the length of the channel. We also studied devices with six gate fingers (Fig. 4.2A), denoted as QPC_{6F}, which have a channel with tunable length L_{eff} . We focus on the differential conductance G , which is obtained by applying and measuring voltage and current signals as in the simplified scheme in Fig. 4.1A (see SAM Section 4.6 for details). Results for G at zero bias voltage V_{sd} will be called linear conductance, while results for G as a function of V_{sd} (bias spectroscopy) will be called nonlinear conductance. Unless stated otherwise, we present data taken at a temperature of 80 mK in zero magnetic field.

4.3 Results from single split-gate QPCs

We first focus on results from QPC_{2F} devices. Figures 4.1B,C present measurements of the linear conductance. The coarse features in these traces are the

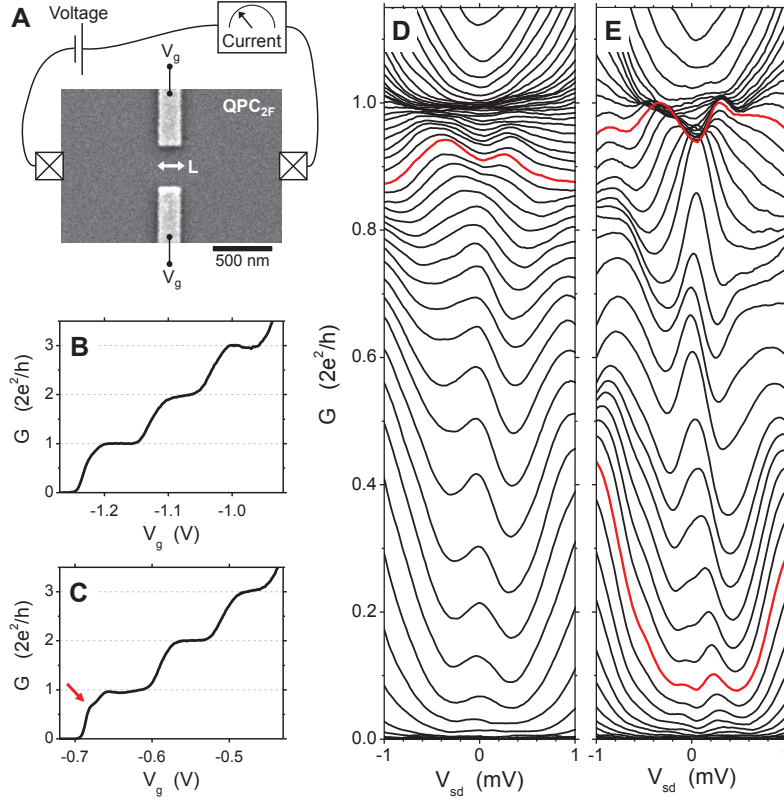


Figure 4.1: Conductance of Quantum Point Contacts (QPC). **(A)** Electron microscope image of a conventional QPC with 2 gate fingers (QPC_{2F}). These gates are on the surface of a wafer with a two-dimensional electron gas (2DEG) at 110 nm or 114 nm depth. Applying voltages V_g to these gates induces a narrow transport channel between source and drain regions of the 2DEG. The conductance of the QPCs is studied by applying and measuring voltage and current signals on contacts to the 2DEG. For QPC_{2F} the length of the transport channel is fixed by the lithographic length L . **(B,C)** Linear conductance G measured on two different QPC_{2F} with $L = 200$ nm. The traces show clear quantized conductance plateaus at integer multiples of $2e^2/h$ (the shift in dependence on V_g for (C) as compared to (B) is due to a different cool-down procedure [20], see SAM on p. 73). The plateaus and transitions between plateaus show small deviations from clean quantized conductance behavior, as for example an additional shoulder at $G \approx 0.7 \cdot (2e^2/h)$ in panel (C) (red arrow). **(D)** Nonlinear conductance G as a function of source-drain voltage V_{sd} at various V_g settings, for the device of panel (B). The Zero-Bias Anomaly (ZBA, enhanced conductance around $V_{sd} = 0$) has mostly single-peak character, but has double-peak character for $G \approx 0.9 \cdot (2e^2/h)$ (for example the red trace). **(E)** Similar results as panel (D) for the device of panel (C). In this device ZBAs with double-peak character appear at $G \approx 0.1 \cdot (2e^2/h)$ and $G \approx 0.95 \cdot (2e^2/h)$.

quantized conductance plateaus at integer multiples of $(2e^2/h)$. The traces show small deviations from ideal quantized conductance behavior. For example, the plateau at $1 \cdot (2e^2/h)$ in panel (C) shows a weak dip. In addition, this same trace shows a shoulder at $G \approx 0.7 \cdot (2e^2/h)$ instead of a smooth step from 0 to $1 \cdot (2e^2/h)$, which was also observed for the device of panel (B) at higher temperatures. This latter effect is typical for the manifestation of the 0.7 anomaly [11]. Results for the nonlinear conductance for these same devices are presented in Fig. 4.1D,E. Most traces between 0 and $1 \cdot (2e^2/h)$ show a single-peak ZBA (the enhancement of conductance within ± 0.5 mV around $V_{sd} = 0$ mV). However, the red traces mark examples where the ZBA appears with double-peak character (the asymmetric character of these nonlinear conductance traces will be discussed below). We initially observed such double-peak ZBAs for a single device (lithographic channel dimensions $L = 200$ nm and width 350 nm) in a set of QPC_{2F} with various widths and lengths values for the channel. We searched for double-peak ZBAs in a set of 80 QPC_{2F} with that same geometry (realized in two different materials, see SAM Section 4.6), and found double-peak ZBAs in about half the studied devices (the SAM Section 4.7 discusses the remarkable fact that double-peak ZBAs were, seemingly, never observed before with QPCs).

We found, however, that it was difficult to draw conclusions from these results from QPC_{2F} devices. The exact manifestation of the 0.7 anomaly and the ZBAs showed strong variation from device to device (while there was no strong variation in the manifestation of non-interacting electron physics such as the quantized conductance [17]), and appeared too diverse for describing the features with a few parameters (compare Figs. 4.1B-D). In addition, for these observations it is difficult to distinguish between signatures of many-body effects and distortions of quantized conductance that do not result from many-body physics. Such distortions could, for example, result from fabrication errors that give significant structure on the QPC saddle-point potential (unintentional formation of a quantum-dot-like system) or an actual atomic impurity or lattice defect in the QPC channel that acts as a scatter center.

4.4 Results from length-tunable QPCs

We addressed this challenge by measuring a set of 6 QPC_{6F} devices, for which we could very gradually change the effective length L_{eff} of the saddle-point potential. These 6 devices showed qualitatively identical behavior with a very regular modulation between single-peak and double-peak ZBAs when increasing L_{eff} .

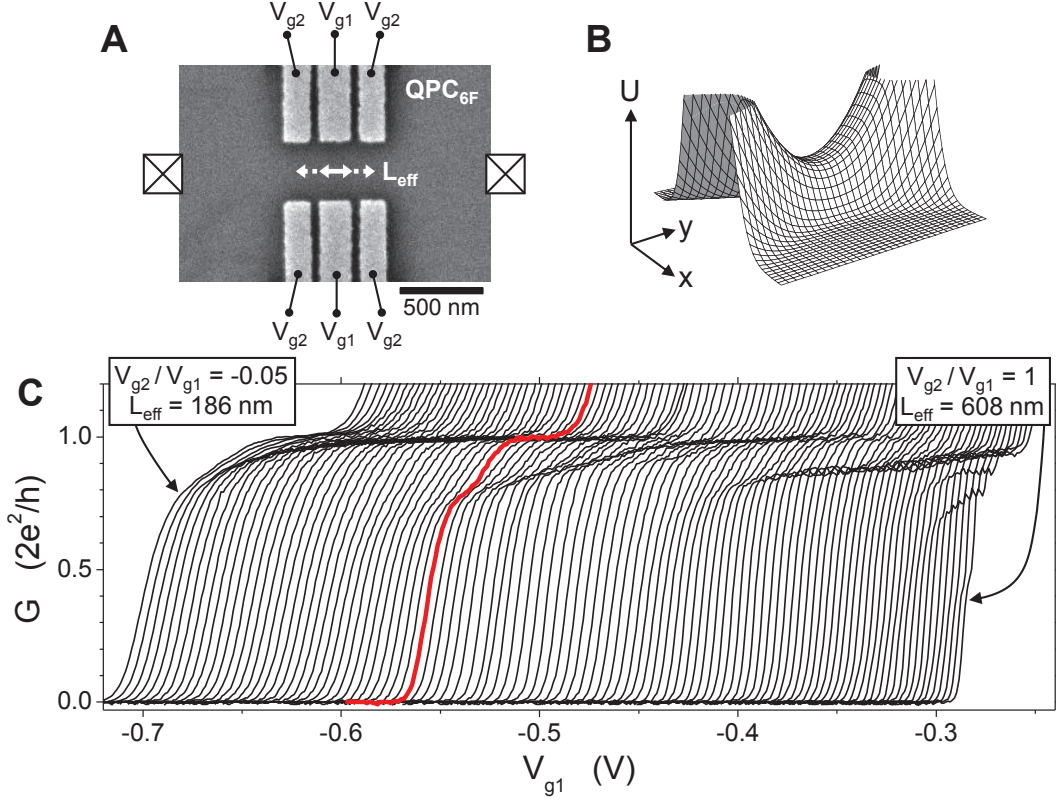


Figure 4.2: Length-tunable quantum point contact (QPC). **(A)** Electron microscope image of a QPC with 6 gate fingers (QPC_{6F}). It has a tunable effective length L_{eff} that is set by operating at a fixed ratio V_{g2}/V_{g1} . **(B)** Saddle-point potential that illustrates the electron potential energy U (without many-body interactions) in the 2DEG plane in a QPC region. **(C)** Linear conductance G as a function of V_{g1} (while co-sweeping V_{g2} at fixed V_{g2}/V_{g1}) measured on a QPC_{6F} for L_{eff} tuned from 186 nm to 608 nm (traces *not* offset). Besides the quantized conductance plateau at $1 \cdot (2e^2/h)$, most traces show a smaller plateau in the range 0.7 to $0.9 \cdot (2e^2/h)$ due to many-body effects. For this signature 3 periods of modulation can be observed in its dependence on V_{g2}/V_{g1} (*i.e.* L_{eff}).

In addition, this study confirmed that changing the effective channel length by as little as 10 nm (the scale of unintentional variation in device fabrication) can significantly change the expression of the many-body effects. These reproducible observations on 6 QPC_{6F} confirm that the modulation between single- and double-peak ZBAs is due to many-body physics that generically occurs, also in ultra-clean QPC channels. However, the exact manifestation is very sensitive to weak static fluctuations on the saddle-point potential (see also Fig. 3.6), which

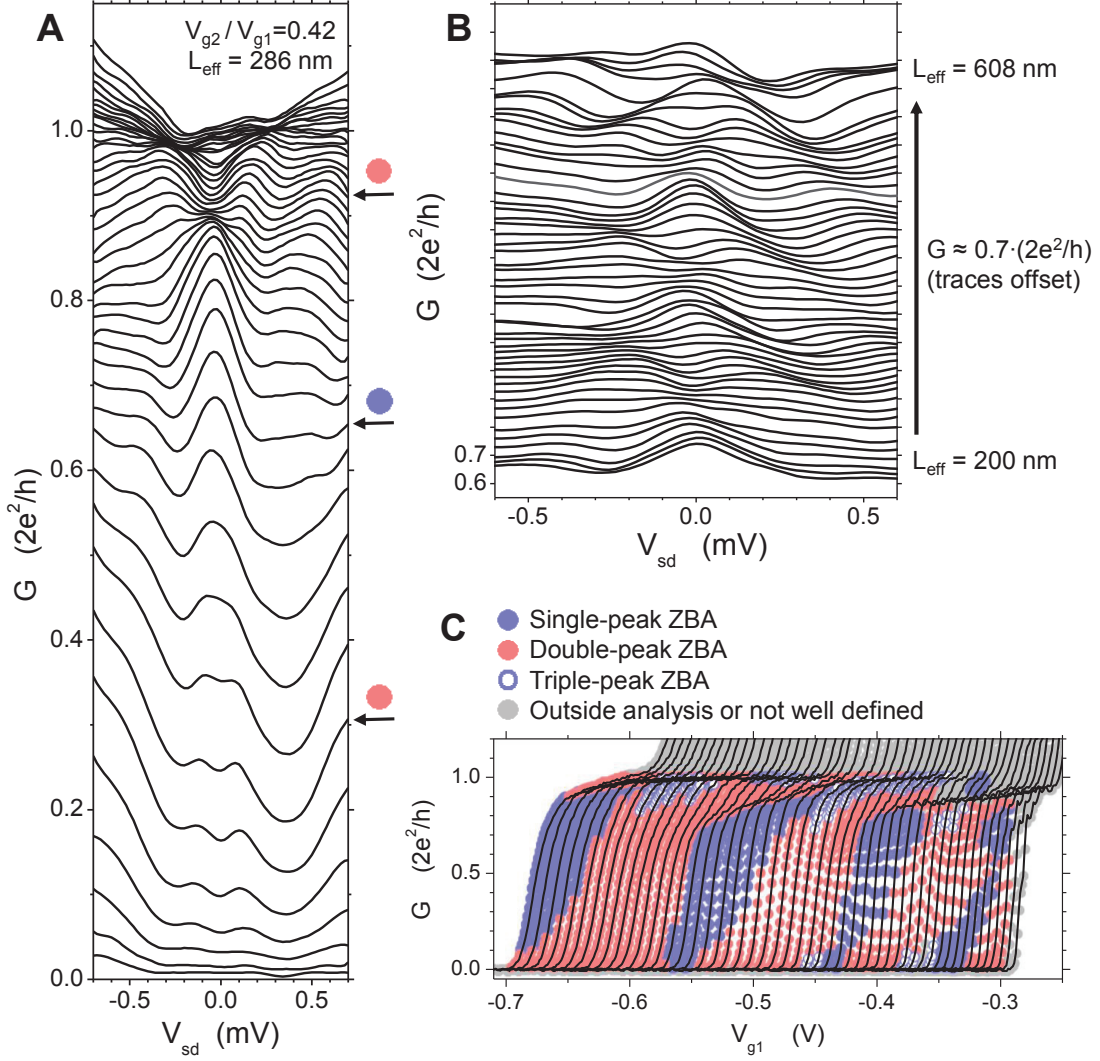


Figure 4.3: Zero-bias anomalies (ZBAs) in the nonlinear conductance of a QPC_{6F}. **(A)** Nonlinear conductance G as a function of source-drain voltage V_{sd} at various V_{g1} settings, for operation at $L_{eff} = 286$ nm. The ZBA appears alternately with single- or double-peak character. **(B)** Evolution of the ZBA in the nonlinear conductance at fixed conductance level of $\sim 0.7 \cdot (2e^2/h)$ as a function of L_{eff} (traces offset). The ZBA has alternately single- or double-peak character. **(C)** The character of the ZBA (single-, double-, or triple-peak, as labeled) mapped out on the linear conductance data of Fig. 4.2C.

are in practice always present due to remote imperfections [18]. This is consistent with the picture that we present below, where the many-body effects result in the formation of one or more self-consistent localized states and where the coupling between these states, and their couplings to the reservoirs, are exponentially

sensitive to very weak structure on the saddle-point potential.

Figure 4.2A presents how we realized QPC_{6F} devices, for which the channel length L_{eff} could be tuned continuously from about 186 nm to 608 nm. These were operated with the gate voltage V_{g1} always more negative than V_{g2} to avoid quantum dot formation. We opened such QPC channels by making V_{g1} less negative at fixed ratio V_{g2}/V_{g1} . The effective length L_{eff} is then set by V_{g2}/V_{g1} (short for V_{g2}/V_{g1} near 0, long for V_{g2}/V_{g1} near 1, see Chapter 5 for details on how L_{eff} is defined). Electrostatic simulations (based on Ref. [23]) show that we thus operate the QPC_{6F} in a regime where the gates induce a smooth saddle-point potential (Fig. 4.2B). That is, the narrow gaps between the gate fingers do not cause significant structure on the potential (see Chapter 5).

Figure 4.2C presents linear conductance results for a QPC_{6F}. All QPC_{6F} showed clear quantized conductance plateaus. In addition, the 0.7 anomaly appears in most traces as a smaller plateau in the range 0.7 to $0.9 \cdot (2e^2/h)$, and it shows a dependence on L_{eff} for which 3 periods of modulation can be observed for the range $L_{eff} = 186$ nm to 608 nm. Nonlinear conductance measurements from this same device are presented in Fig. 4.3. Figure 4.3A shows how the ZBAs appear for $L_{eff} = 286$ nm. At fixed length, the ZBAs alternate between single-peak and double-peak character when opening the QPC. Figure 4.3B shows that there is also a modulation between single- and double-peak character when increasing L_{eff} at a fixed level for the conductance (as evaluated immediately next to the ZBA). Figure 4.3C plots again the data of Fig. 4.2C, with colored symbols on the traces that mark whether the ZBA at that point has single- or double peak character (in some cases we find ZBAs that are best described as triple-peak). The modulation between single-peak and double-peak ZBA as a function of L_{eff} also shows about 3 periods, and is clearly correlated with the modulation of the 0.7 anomaly in Fig. 4.2C. Notably, the length increase of L_{eff} that induces one period of modulation (~ 100 nm to ~ 150 nm) has a value that matches with the Fermi wavelength in the QPC channel (see SAM Section 4.8 for details). We use this in our analysis (below) to conclude that the observed periodicity is linked to Friedel oscillations in the channel, which gradually develop additional periods as the QPC channel gets longer. Fig. 4.5C illustrates with a sketch how this can also result in modulation of a Friedel oscillation with a single or pair of maxima. That such Friedel oscillations occur upon scattering in a 2DEG has been observed directly in a different setting [24].

Figure 4.4 presents for this same device a study of the temperature dependence of the 0.7 anomaly and ZBAs. At the highest temperature (4000 mK), the linear

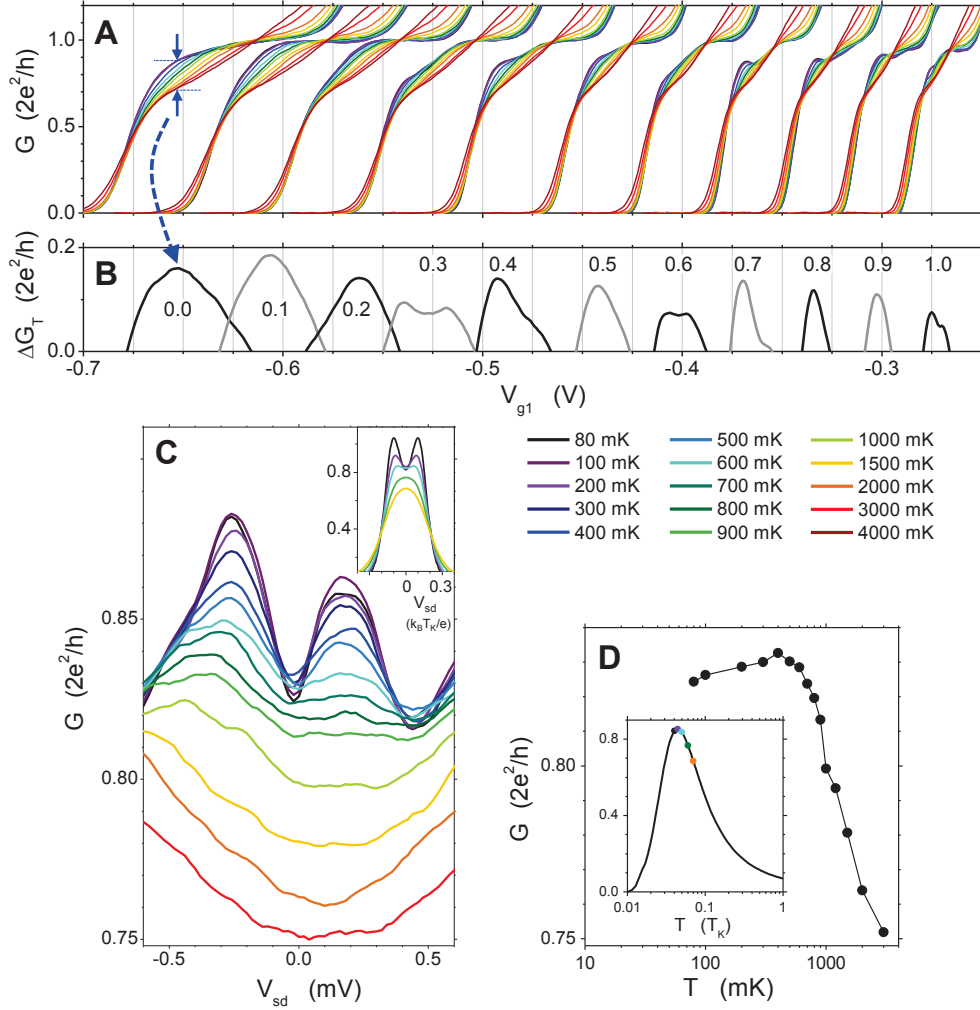


Figure 4.4: Temperature dependence of the linear conductance and ZBAs. **(A)** Evolution of the linear conductance traces of Fig. 4.2C as a function of temperature (color legend above panel (D)). Traces are displayed for gate ratios $V_{g2}/V_{g1} = 0.0, 0.1, 0.2 \dots 1.0$, as labeled in (B). **(B)** The difference in linear conductance ΔG_T between the 80 mK and 4000 mK traces of panel (A). These traces directly reflect the enhancement of the linear conductance around the 0.7 anomaly with decreasing temperature. **(C)** Evolution of the nonlinear conductance (with double-peak ZBA) as a function of temperature for a QPC_{6F} operated with fixed $V_{g1} = -0.528$ V and fixed $V_{g2}/V_{g1} = 0.3$ (traces not offset). The inset presents calculated nonlinear-conductance traces from a two-impurity Kondo model (see main text). **(D)** The conductance level of panel (C) near zero bias (between the two ZBA peaks, evaluated at $V_{sd} = -0.02$ mV) as a function of temperature (logarithmic axis). The inset presents the same analysis applied to the theoretical results in the inset of panel (C).

conductance traces no longer show quantized conductance plateaus (Fig. 4.4A) and the only remaining feature is the 0.7 anomaly, which no longer shows a modulation as a function of L_{eff} . For the following discussion we focus on gate settings that give $G \approx 0.7 \cdot (2e^2/h)$ at 4000 mK. At these points, the linear conductance increases from 0.7 towards $1 \cdot (2e^2/h)$ when lowering the temperature. Notably, the increase in conductance is for all L_{eff} for the largest part due to a growing height of the ZBA (observed in the corresponding nonlinear conductance results). Also, subtracting 4000 mK traces from 80 mK traces (defining the traces ΔG_T in Fig. 4.4B) shows that the conductance increase is largest around these points. However, some ΔG_T traces show a suppression (for $V_{g2}/V_{g1} = 0.3, 0.6$ and 1.0 in Fig. 4.4B) and these points coincide with a strong 0.7 anomaly at the lowest temperatures and pronounced double-peak character for the ZBA. That is, the ΔG_T curves show that the enhancement of G due to many-body effects is strongest where the linear conductance is about $0.7 \cdot (2e^2/h)$ at high temperatures, but that there is a range within each L_{eff} period where exactly at this point the strongest expression of a new effect causes in fact a dip in ΔG_T . Further analysis shows that this coincides with the points where the double-peak ZBA shows behavior that is characteristic for the two-impurity Kondo model, and that the energy scale for the coupling between the two spins in this model appears maximum at this point.

This further analysis is based on data as in Fig. 4.4C. The nonlinear conductance develops from $0.75 \cdot (2e^2/h)$ at 3000 mK into a double-peak ZBA with peak values up to about $0.90 \cdot (2e^2/h)$ as the temperature is decreased. The conductance values between the peaks (the linear conductance), however, get lower when lowering the temperature sufficiently. The conductance values between the peaks are analyzed in Fig. 4.4D and show a nonmonotonic temperature dependence. The insets for Fig. 4.4C,D show the same behavior for G as calculated with the two-impurity Kondo model (theory traces provided by a collaboration with R. Aguado, based on Ref. [22]). The nonmonotonic temperature dependence is characteristic for two-impurity Kondo physics and occurs due to a competition between anti-ferromagnetic ordering and Kondo interaction with a reservoir for the two localized electron spins. The theoretical traces that are shown here are for two impurity sites that have the same coupling strength Γ to a neighboring electron reservoir, and the same Kondo temperature T_K . Calculations for the case with a small asymmetry between the two Γ parameters give asymmetric double-peak ZBAs, with the minimum conductance level between the peaks not exactly at $V_{sd} = 0$, in a manner that is very similar to the asymmetry in the double-peak

ZBAs observed experimentally. In practice, we should expect such asymmetries between the two Γ parameters since the values of Γ depend exponentially on the potential landscape between the localized site and the electron reservoir. This model is thus compatible with our observations that the signatures of the many-body physics are in practice highly sensitive to small differences between devices and weak static fluctuations on the QPC saddle-point potential (see Fig. 3.6).

We also studied the magnetic field dependence of the double-peak ZBAs, but this showed very diverse results. We see this as an indication that the self-consistent localized states in QPCs are more easily disturbed by the field than states with enforced localization in quantum dots [14]. For the ZBAs that had pronounced single-peak character, the behavior showed agreement with the single-impurity Kondo model when analyzed as in Ref. [11].

A more general analysis of the number of peaks, and the positions, widths and amplitudes of ZBA peaks is presented in Fig. 4.5A,B (similar plots for various other conductance levels are in SAM Section 4.7). The symbol size in Fig. 4.5B is proportional to peak area. We mostly observe that the peak width roughly correlates with peak amplitude, such that similar plots with the symbol size proportional to peak width or peak amplitude roughly give the same picture. For the Full-Width at Half-Maximum (FWHM) of the peaks we mainly find values in the range 0.1 to 0.4 mV (or meV for energy scale) for the conductance levels between 0.4 and $0.85 \cdot 2e^2/h$ (while the effective electron temperature of 80 mK allows for probing peak structures as narrow as $4k_B T/e = 0.03$ mV). Within a single- and two-impurity Kondo interpretation of our data the peak width corresponds to twice the Kondo temperature of a localized electron state. The distance between the peaks for a double-peak ZBA (two-impurity Kondo model) is then equal to two times the effective spin-spin interaction strength. For the data in Fig. 4.4C this interaction energy scale is ~ 0.2 meV, and this is a typical value for the larger data set in Fig. 4.5B. This should be consistent with the temperature where the double-peak character of the ZBA gets washed by temperature increase. For the data in Fig. 4.4C this occurs for ~ 800 mK (*i.e.* ~ 0.1 meV). This is in reasonable agreement with the distance between the peaks. The fact that it is on the low side is probably due to the fact that the Kondo temperature T_K for this setting is at almost the same energy scale (~ 0.15 meV when estimated as half the peak widths in Fig. 4.4C).

We thus interpret our observations as signatures for the predicted single- and paired self-consistent localized states in QPCs [16]. The combination of Kondo behavior for the ZBAs and a length dependence that matches with the

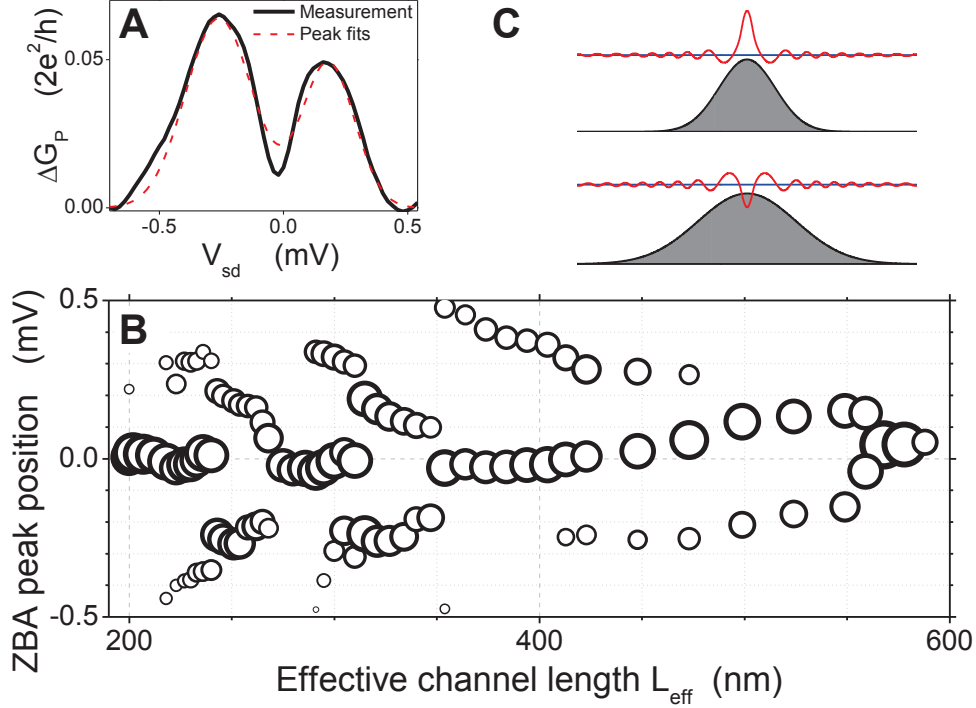


Figure 4.5: Analysis of ZBA peaks at $0.85 \cdot (2e^2/h)$ conductance level and illustration of Friedel oscillations. **(A)** An example of results from fitting two Gaussian peak shapes on a double-peak ZBA. Fits are carried out on peak traces ΔG_P , that are obtained by subtracting a background conductance level (linear or parabolic where needed). **(B)** Result of fitting ZBA peaks, displayed as peak positions (in V_{sd} units) as a function of L_{eff} . The area of the symbols is proportional to the peak area (obtained as the product of peak amplitude and peak width). **(C)** Diagrams illustrating the manifestation of Friedel oscillations in the QPC channel (horizontal axis is position x along the QPC channel). On both sides of the QPC potential barrier (black line), the electron charge density (red line) shows a decaying oscillation due to scattering and charge screening at the barrier. This so-called Friedel oscillation is here illustrated for electrons at the Fermi energy (blue line). The Friedel oscillations have a phase ϕ that depends on the details of the barrier, such that they can connect in the center of the QPC with a single maximum (top) or minimum (bottom) in the charge density. The latter case corresponds to having two maxima directly next to the center of the QPC. The Friedel oscillation traces were calculated with Eq. 4.1 for our material parameters, with a phenomenological linear dependence of ϕ on L_{eff} (except for $|x| < 10$ nm, where traces were filled in by smoothly connecting data from $|x| > 10$ nm instead).

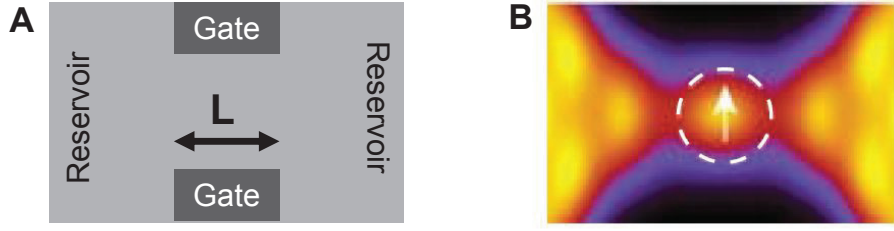


Figure 4.6: Results of Spin-Density-Functional Theory calculations (SDFT). **(A)** Gate and reservoir geometry that is considered for the simulations. **(B)** Results of SDFT calculations for a QPC channel with length $L = 250$ nm (figure adapted from Ref. [16]). The plot area is a direct map of the geometry as in panel (A). The color scale represents electron spin-up density (black for zero, yellow for $0.35 \cdot 10^{11} \text{ cm}^{-2}$) and shows a localized state in the QPC channel that has about one electron of charge and a net spin. One can recognize that the parts of the reservoirs that extend into the channel also show a weak modulation in the density (directly reflecting the physics of Friedel oscillations), where the maximums can be interpreted as the onset of additional localized states. Ongoing SDFT calculations in the team of Y. Meir that focus on the dependence of this type of results on channel length L show that for increasing L the number of localized states in the channel indeed slowly increases to situations with 2, 3 or 4 localized states in the channel. New SDFT studies of the dependence on gate voltage (opening the QPC at fixed length) also show transitions from 1 to more localized states.

physics of Friedel oscillations favors this interpretation over alternative theories for the many-body effects in QPCs [4]. We strengthen this conclusion by extending the numerical calculations of Ref. [16] for the scenario where QPC channels gradually become longer at a fixed level of conductance. These Spin-Density-Functional Theory (SDFT) calculations are carried out in the team of our collaborator Y. Meir. An example of results from such calculations is presented in Fig. 4.6. Ongoing work on such SDFT calculation show that for a wide range of parameters additional periods of the Friedel oscillation form in the channel as it gets longer. This first causes a transition from a single to a pair of localized states. As the channel grows even longer, a chain of three localized states appears. Kondo physics from such a state can cause a ZBA that has mainly single-peak character with two remote side peaks (or a ZBA with triple-peak character). Consequently, the modulation between single-peak and double-peak ZBAs as a function of L_{eff} that is observed in our experiments is consistent with these SDFT calculations. A further theoretical analysis of these SDFT studies and Kondo modeling is in progress.

4.5 Conclusions

In conclusion, we have discovered an operation regime where the many-body effects in QPCs show signatures of localization with rich and tunable behavior. Our studies in this direction systematically showed ZBAs that reflect both single and paired localized states due to many-body physics. The periodic character of both the ZBA and the 0.7 anomaly as a function of QPC length provides evidence that the physics of Friedel oscillations is fundamental to these phenomena. Advanced numerical SDFT modeling that also accounts for Coulomb and exchange interactions showed that such Friedel oscillations generically develop into single or paired self-consistent localized states in the QPC channel, with a dependence on channel length that is consistent with a periodic modulation between single-peak and double-peak ZBAs. In turn, with such localized states near a reservoir the Kondo effect will often play a role in the formation of the many-body state. Research on quantum dots showed that the Kondo effect is under these conditions a very generic phenomenon and the behavior of the ZBAs in our QPCs show indeed a strong correspondence with transport through single and paired Kondo states. However, as compared to the enforced localization in quantum dots, the self-consistent localized states in QPCs get more easily disturbed by external parameters like magnetic field. In these cases the Kondo behavior in QPCs deviates from trends that are predicted by the most basic models for Kondo physics. Our work shows that tunable QPCs offer an excellent new test ground for detailed studies of Friedel oscillations and electron many-body effects at the level of a single site.

Acknowledgments

We thank B. J. van Wees and A. Aqeel for stimulating discussions. M. J. Iqbal thanks the Pakistani HEC for financial support.

Supporting Appendix Material

4.6 Appendix: Materials and methods

Materials and device fabrication QPC devices were fabricated with two different GaAs/AlGaAs heterostructures containing a 2DEG in a heterojunction quantum well. They had similar MBE-growth parameters and properties of the 2DEG. We obtained very similar results with both materials. Most of the results presented in this report come from Material 2, only the data in Fig. 4.1B,D comes from Material 1.

Material 1 was a GaAs/Al_{0.32}Ga_{0.68}As heterostructure with a 2DEG at 114 nm below the surface from modulation doping with Si at about $1 \cdot 10^{24} \text{ m}^{-3}$. At 4.2 K, the mobility of the 2DEG was $\mu = 159 \text{ m}^2/\text{Vs}$, and the electron density $n_s = 1.5 \cdot 10^{15} \text{ m}^{-2}$ after cooling down in the dark. The layer with modulation doping started at 37 nm distance from the 2DEG position towards the wafer surface (this material was uniquely used in the related results presented in Ref. [17]).

Material 2 was a GaAs/Al_{0.35}Ga_{0.65}As heterostructure with a 2DEG at 110 nm below the surface from modulation doping with Si at about $1 \cdot 10^{24} \text{ m}^{-3}$. At 4.2 K, the mobility of the 2DEG was $\mu = 118 \text{ m}^2/\text{Vs}$, and the electron density $n_s = 1.60 \cdot 10^{15} \text{ m}^{-2}$. Here the layer with modulation doping started at 45 nm distance from the 2DEG position.

The QPCs were activated by applying negative gate voltages V_g to the gate electrodes on the wafer surface. The 2DEG below the electrodes is then fully depleted, and tuning of V_g allows for controlling the effective QPC shape. The depletion gates were defined with standard electron-beam lithography and lift-off techniques, using deposition of 15 nm of Au with a Ti sticking layer. The reservoirs were connected to macroscopic leads via ohmic contacts, which were realized by annealing a thin Au/Ge/Ni layer that was deposited on the surface. Part of our data (including all the results presented in this report, except for the data in Fig. 4.1B,D) was obtained after cooling down with about +0.3 V on the gates for suppressing $1/f$ and telegraph noise in the conductance signals due to charge instabilities in the doping layer [20]. We obtained (besides the change in noise properties) similar results for the cases with and without biased cool-down.

Measurement techniques and setup

The presented results of linear and nonlinear conductance measurements all concern the differential conductance $G = dI/dV_{sd}$ (where I is the measured current). For linear conductance measurement we used standard lock-in techniques (typically at 387 Hz), with an ac voltage bias $V_{sd} = V_{ac} = 10 \mu\text{V}$. For the nonlinear conductance measurements we superimposed an ac and a dc voltage bias, $V_{sd} = V_{dc} + V_{ac}$. We used an effective 4-terminal measurement where we locally measured the source-drain voltage drop V_{sd} across the QPC, such that we can present results without significant contributions from series resistance. Only one of the source-drain contacts was connected to the grounded shielding of our setup, and all gate voltages were applied with respect to this ground.

Measurements were performed in a dilution refrigerator with the sample at temperatures from $\sim 5 \text{ mK}$ to 4.2 K . For all our data the temperature dependence saturated when cooling below $\sim 80 \text{ mK}$. This is consistent with independent measurements of the lowest effective electron temperature that could be achieved with this setup.

The in-plane magnetic field was applied both parallel and perpendicular to the current direction and we measured both devices with the current along the $[110]$ and $[-110]$ directions of the crystal, but the results did not depend significantly on these orientations. Alignment of the sample with the magnetic field was within 1° , as determined from Hall voltage measurements on the 2DEG.

4.7 Appendix: Earlier reports showing modulated 0.7 anomalies and double-peak ZBAs

A remarkable aspect of our observations of double-peak ZBAs in many different QPC devices is that such observations were to our knowledge never explicitly reported before, despite about 20 years of research into many-body effects in QPCs (with a few hundred publications reporting on the topic). Similarly, our observations of a periodic modulation of the 0.7 anomaly as a function of QPC channel length is a phenomenon that -to our knowledge- has not been reported before. It is therefore justified to ask why this is the case, and to question whether our -seemingly unique- observations result from an irregularity that is unique to our devices. The main text already reported that we observed double-peak ZBAs in many conventional QPC_{2F} devices from two different wafer materials and in 6 different QPC_{6F} devices, which is a strong indication that the new phenomena

are not due to a particular device irregularity.

We noticed in our studies on many QPC_{2F} that a strong expression of the many-body effects that we report here appears as quantized conductance plateaus that are not flat, and a 0.7 anomaly that appears as a peaked resonance instead of only a shoulder on the step from $G = 0$ to $1 \cdot (2e^2/h)$ (see for example also Fig. 4.4A near $V_{g1} = -0.35$ V). These two signatures can then also show replicas at and just below the second and third quantized conductance plateau. In such cases, the ZBA often has double or triple-peak character with strong asymmetries and smaller side peaks. Such QPC results were in fact observed long before by our group, but such results (and further studies of the devices) were discarded because a device imperfection was suspected. We know that most groups in the field had the same practice (see for example Ref. [19]). Also, such imperfections on quantized conductance traces were often removed by applying a small (typically 25 mT) perpendicular magnetic field during the QPC studies, or by measuring at about 600 mK instead of the lowest available temperature (see also Ref. [19], not applied in any of our studies). Only our recent study on a large number of QPC_{2F} showed us that such strong deviations on quantized conductance traces fall in fact on a regular trend from weak to strong expression of the 0.7 anomaly and the ZBA. Nevertheless, it remains difficult to investigate this systematically since the appearance is very diverse, and for results from one particular QPC_{2F} it remains a challenge to rule out a (partial) role for an actual material or device defect.

In the remainder of this Section we report that several signatures of double-peak ZBAs and periodic modulation of the 0.7 anomalies can in fact be recognized in the experimental data of earlier publications (but they were never discussed or systematically investigated). Below here we review the literature on this, first for modulation of the 0.7 anomaly and subsequently for double-peak ZBAs. For both phenomena it is also illustrative to inspect all experimental data in the extensive review Ref. [4].

Reports showing modulated 0.7 anomalies

Several publications report a very regular modulation of the 0.7 anomaly over about 1 period as a function of back(top)-gate voltage in experiments that have a large-area back(top) gate in addition to the split-gate structure of the QPC. A deviation from our experiment is that such a back-gate modulates at the same time the QPC saddle-point potential and the electron density of the reservoirs. A regular modulation of the 0.7 anomaly over about 1 period with a fixed density for

the reservoirs was also reported before, in experiments with split-gate QPCs that have an additional side gate or narrow top gate. Examples are Ref. [25] (Fig. 2), Ref. [19] (Fig. 6-17, left panel on QPC2 on p. 105), Ref. [26] (Figs. 2, 3a and 3b), Ref. [27] (Fig. 2), and Ref. [28] (Fig. 1). The latter three references show in fact modulation over about 1.5 period, with an anomaly at a conductance level of about $0.9 \cdot (2e^2/h)$ that disappears while a new one appears at about $0.6 \cdot (2e^2/h)$ (as in our data).

Reports showing double-peak ZBAs

We also found several publications that report double-peak ZBAs for data taken at zero magnetic field. An example that looks much like our data is in Ref. [19], Fig. 6-19a on p. 107. Other examples can be found in Ref. [29] (Fig. 4) and Ref. [30] (Figs. 1a, 1c, 3b and 3d).

4.8 Appendix: Friedel oscillations and Fermi wavelength in the QPC

The approximate form of a Friedel oscillation for screening of a charged scatter center at $x = 0$ (valid for positions not too close to $x = 0$) is

$$\rho_{devi} \propto \frac{\sin(2k_F x + \phi)}{x^d}, \quad (4.1)$$

where ρ_{devi} is the deviation in electron charge density, d is the dimensionality of the Fermi liquid, k_F is the Fermi wavenumber, and ϕ is a phase parameter that depends on the details of the scattering [31]. The factor 2 before k_F shows that the wavelength of Friedel oscillations is half the Fermi wavelength.

The electron reservoirs in our experiment had a density $n_{2D} = 1.6 \cdot 10^{15} \text{ m}^{-2}$, which corresponds to a Fermi wavelength $\lambda_F = 2\pi/k_F = 62 \text{ nm}$. In the QPC channel the electron kinetic energy is reduced. For an estimate we assume that the kinetic energy ($E_F = 5.7 \text{ meV}$ for the reservoir) gets reduced in the QPC entries to a value of about 1 meV , which is estimated by taking half the 1D subband energy spacing of our QPC (see Chapter 3). This yields that λ_F increases here to about 150 nm , which corresponds to about 75 nm for the Friedel oscillation wavelength in the QPC channel. When increasing the length of the QPC, the number of Friedel oscillations in the channel increases at the same time (more or less symmetrically) in both entries of the QPC. Thus, a length dependence that relies on the number of Friedel oscillations in the channel should show a

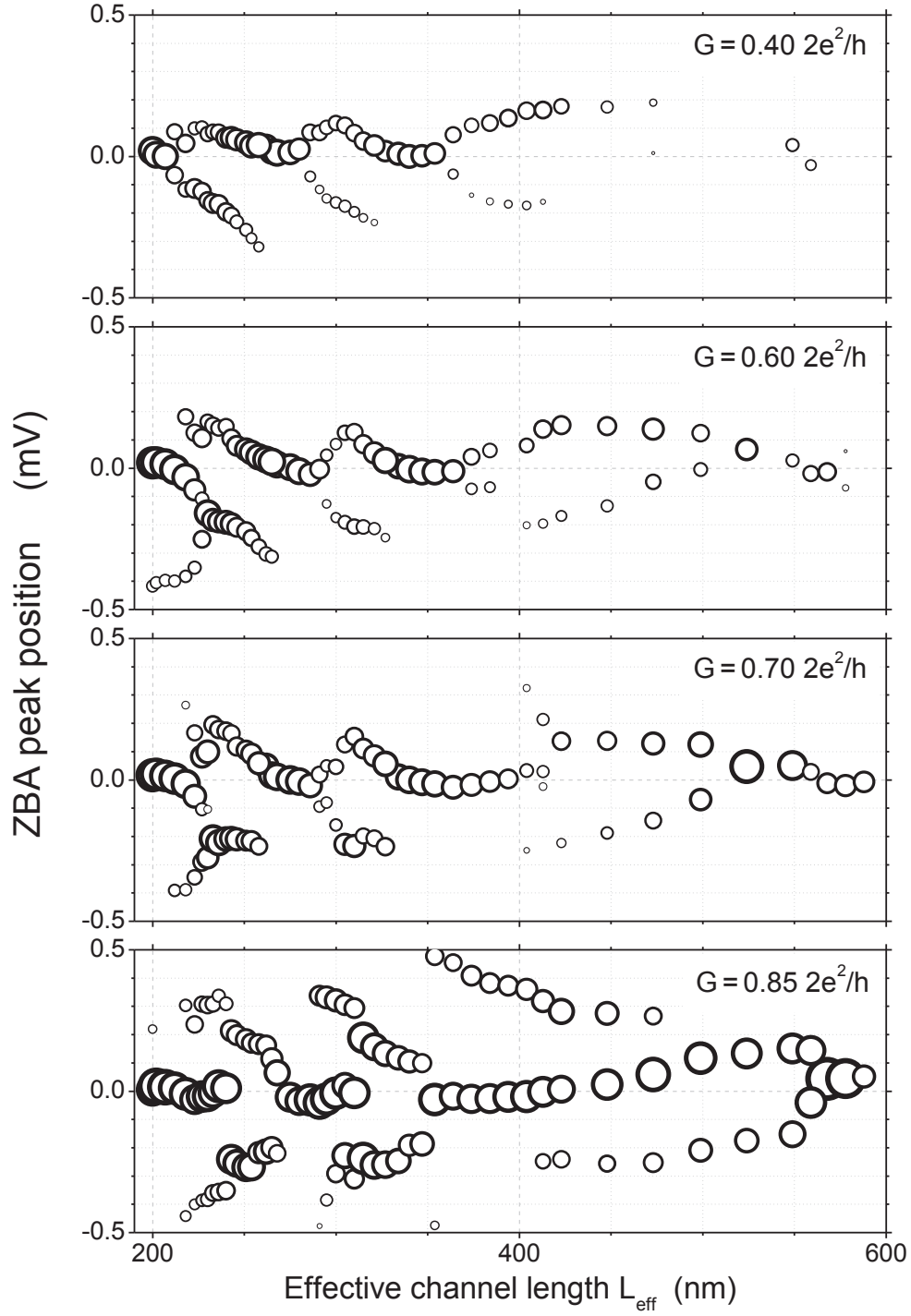


Figure 4.7: Analysis of ZBA peak positions at $G = 0.4, 0.6, 0.7$ and $0.85 \cdot (2e^2/h)$, with a symbol size that is proportional to the peak area (product of height and FWHM from peak fitting).

modulation with a periodicity of about 150 nm, or a bit smaller (~ 100 nm) if the effective Fermi wavelength in the QPC entries is still a bit closer to the value for the reservoirs. Fig. 4.7 shows that this is well in the range of the observed periodicity. The fact that the modulation occurs faster around $L_{eff} = 250$ nm than around $L_{eff} = 500$ nm is consistent with the fact that the latter case corresponds to a longer shallow channel (less abrupt saddle-point potential) where the Fermi wavelength is reduced over a longer range.

4.9 Appendix: Analysis of ZBA peak positions at $G = 0.4, 0.6, 0.7$ and $0.85 \cdot (2e^2/h)$

Figure 4.7 presents the positions of ZBA peaks as in Fig.4.5B for 4 different conductance levels.

Bibliography

- [1] B. J. van Wees *et al.*, Phys. Rev. Lett. **60**, 848 (1988).
- [2] D. A. Wharam *et al.*, J. Phys. C **21**, L209 (1988).
- [3] K. J. Thomas *et al.*, Phys. Rev. Lett. **77**, 135 (1996).
- [4] A. P. Micolich, J. Phys.: Condens. Matter **23**, 443201 (2011).
- [5] A. Bertoni, P. Bordone, R. Brunetti, C. Jacoboni, and S. Reggiani, Phys. Rev. Lett. **84**, 5912 (2000).
- [6] R. Ioniciu, G. Amaratunga, and F. Udrea, Int. J. Mod. Phys. B **15**, 125 (2001).
- [7] M. Blaauboer and D. P. DiVincenzo, Phys. Rev. Lett. **95**, 160402 (2005).
- [8] Y. Komijani *et al.*, Euro. Phys. Lett. **91**, 67010 (2010).
- [9] N. T. Bagraev, I. A. Shelykh, V. K. Ivanov, and L. E. Klyachkin, Phys. Rev. B **70**, 155315 (2004).
- [10] N. Tombros *et al.*, Nature Physics **7**, 697 (2011).
- [11] S. M. Cronenwett *et al.*, Phys. Rev. Lett. **88**, 226805 (2002).
- [12] D. Goldhaber-Gordon *et al.*, Nature **391**, 156 (1998).
- [13] Sara M. Cronenwett, Tjerk H. Oosterkamp, Leo P. Kouwenhoven, Science **281**, 540 (1998).
- [14] H. Jeong, A. M. Chang, M. R. Melloch, Science **293**, 2221 (2001).
- [15] Kenji Hirose, Yigal Meir and Ned S. Wingreen, Phys. Rev. Lett. **90**, 026804 (2003).
- [16] T. Rejec and Y. Meir, Nature **442**, 900 (2006).
- [17] E. J. Koop, A. I. Lerescu, J. Liu, B. J. van Wees, D. Reuter, A. D. Wieck, C. H. van der Wal, J. Supercond. Nov. Magn. **20**, 433 (2007).
- [18] Such weak potential fluctuations are to be expected in QPC devices. They can, for example, result from the small device-to-device variation that is inherent to the nanofabrication process. In addition, our devices have a doping layer at about 40 nm distance from the QPC channel. In this doping layer ionized doping centers are at random positions with an average inter-dopant distance of about 10 nm.
- [19] S. M. Cronenwett, *Coherence, Charging, and Spin Effects in Quantum Dots and Quantum Point Contacts*, PhD thesis, Stanford University (2001).

- [20] C. Buizert *et al.*, Phys. Rev. Lett. **101**, 226603 (2008).
- [21] Y. Meir, K. Hirose and N. S. Wingreen, Phys. Rev. Lett. **89**, 196802 (2002).
- [22] R. Lopez, R. Aguado, and G. Platero, Phys. Rev. Lett. **89**, 136802 (2002).
- [23] J. Davies, I. A. Larkin, and E. V. Sukhorukov, J. Appl. Phys. **77**, 4504 (1995).
- [24] K. Kanisawa, M. J. Butcher, H. Yamaguchi, and Y. Hirayama, Phys. Rev. Lett. **86**, 3384 (2001).
- [25] K. S. Pyshkin *et al.*, Phys. Rev. B **62**, 15842 (2000).
- [26] D. J. Reilly *et al.*, Phys. Rev. B **63**, 121311(R) (2001).
- [27] W.K. Hew *et al.*, Physica E: Low-dim. Systems and Nanostruc. **40**, 1645 (2008).
- [28] P. M. Wu, P. Li, and A. M. Chang, arXiv:1007.0150.
- [29] N. K. Patel *et al.*, Phys. Rev. B **4**, 13549 (1991).
- [30] T.-M. Chen *et al.*, Phys. Rev. B **79**, 153303 (2009).
- [31] G. E. Simion and G. F. Giuliani, Phys. Rev. B **72**, 045127 (2005).

Chapter 5

Split-gate quantum point contacts with tunable channel length

Abstract

We report on developing split-gate quantum point contacts (QPCs) that have a tunable length for the transport channel. The QPCs were realized in a GaAs/AlGaAs heterostructure with a two-dimensional electron gas (2DEG) below its surface. The conventional design uses 2 gate fingers on the wafer surface which deplete the 2DEG underneath when a negative gate voltage is applied, and this allows for tuning the width of the QPC channel. Our design has 6 gate fingers and this provides additional control over the form of the electrostatic potential that defines the channel. Our study is based on electrostatic simulations and experiments and the results show that we developed QPCs where the effective channel length can be tuned from about 200 nm to 600 nm. Length-tunable QPCs are important for studies of electron many-body effects because these phenomena show a nanoscale dependence on the dimensions of the QPC channel.

This chapter is based on Ref. 3 on p. 159.

5.1 Introduction

A quantum point contact (QPC) is the simplest mesoscopic device that directly shows quantum mechanical properties. It is a short ballistic transport channel between two electron reservoirs, which shows quantized conductance as a function of the width of the channel [1, 2]. A widely applied approach for implementing QPCs is using a split-gate structure on the surface of a heterostructure with a two-dimensional electron gas (2DEG) at about 100 nm beneath its surface. The conventional design of such a split-gate QPC has two metallic gate fingers (Fig. 5.1a). Operating this device with a negative gate voltage V_g results in the formation of a barrier with a small tunable opening between two 2DEG reservoirs, because the 2DEG below the gate fingers gets depleted over a range that depends on V_g . For electrons in the 2DEG, this appears as an electrostatic potential U that is a large barrier with a small opening in the form of a saddle-point potential (Fig. 5.3). The saddle-point potential gives transverse confinement in the channel that is roughly parabolic, which results for this transverse direction in a discrete set of electronic energy levels. For electron transport along the channel this gives a discrete set of subbands with one-dimensional character. Quantized conductance appears because each subband contributes $G_0 = 2e^2/h$ to the channel's conductance [1, 2], where e is the electron charge and h is Planck's constant.

We present here the design and experimental characterization of QPCs which offer additional control over the shape of the saddle-point potential. We focused on developing devices for which the effective length of the saddle-point potential (along the transport direction) can be tuned *in situ*. The additional control is implemented with a symmetric split-gate design based on 6 gate fingers (Fig. 5.1b). Such devices will be denoted as QPC_{6F}, and conventional devices with 2 gate fingers (Fig. 5.1a) as QPC_{2F}. These QPC_{6F} are operated with the gate voltage on the outer fingers (V_{g2}) less negative than the gate voltage on the central fingers (V_{g1}) to avoid quantum dot formation. Sweeping V_{g1} from more to less negative values opens the QPC_{6F}. By co-sweeping V_{g2} at fixed ratio V_{g2}/V_{g1} it behaves as a QPC with a certain length for the saddle-point potential, and this length can be chosen by setting V_{g2}/V_{g1} : It is shortest for $V_{g2}/V_{g1} \approx 0$ and longest for $V_{g2}/V_{g1} \lesssim 1$. For our design the effective length could be tuned from about 200 nm to 600 nm.

The motivation for developing these length-tunable QPCs comes from studies of electron many-body effects in QPCs. A well-known manifestation of these

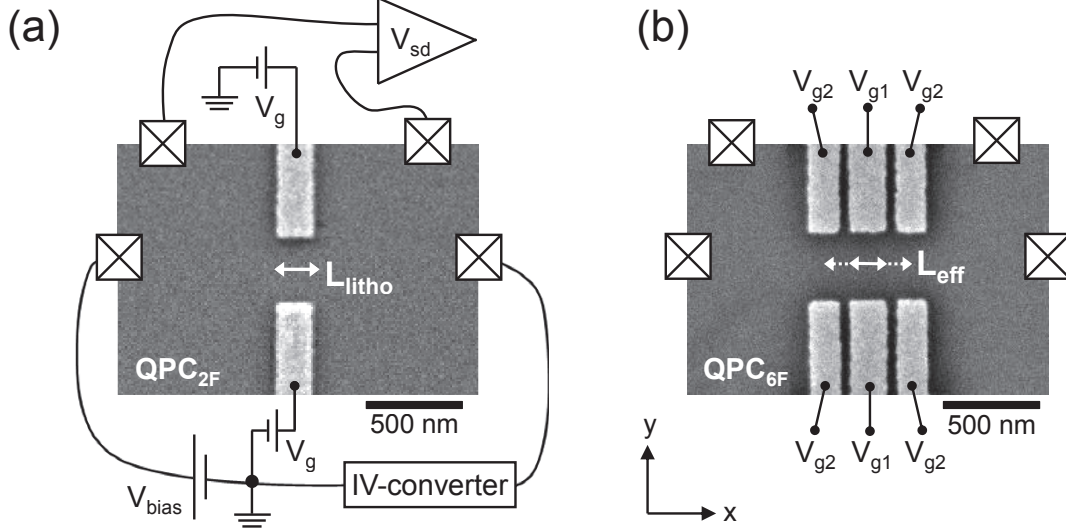


Figure 5.1: (a) SEM image of a conventional split-gate quantum point contact (QPC). It has two gate fingers (QPC_{2F} device). The length of the QPC channel is fixed and can be parameterized by the lithographic length L_{litho} of the gate structure. The diagram also illustrates the measurement scheme (see main text for details). (b) SEM image of a length tunable QPC with 6 gate fingers (QPC_{6F} device). Here the effective length L_{eff} of the QPC can be tuned by changing the ratio of the gate voltages on the central gates (V_{g1}) and side gates (V_{g2}).

many-body effects is the so-called 0.7 anomaly [3], which is an additional shoulder at $0.7 G_0$ in quantized conductance traces. These many-body effects are, despite many experimental and theoretical studies since 1996 [4], not yet fully understood. Recent theoretical work [5] suggested that many-body effects cause the formation of one or more self-consistent localized states in the QPC channel, and that these effects result in the 0.7 anomaly and the other signatures of many-body physics. This theoretical work predicted a clear dependence on the length of the QPC channel, and testing this directly requires experiments where this length is varied.

The work by Koop *et al.* [6] already explored the relation between the device geometry and parameters that describe the many-body effects in a large set of QPC_{2F} devices (see also Chapter 3). This work compared nominally identical devices, and devices for which the lithographic length L_{litho} (see Fig. 5.1a) and width of the channel in the split-gate structure was varied. These results were, however, not conclusive. The parameters that describe the many-body effects showed large, seemingly random variation, not correlated with the device ge-

ometry. At the same time, the devices showed (besides the 0.7 anomaly) clean quantized conductance traces, and the parameters that reflect the non-interacting electron physics did show the variation that one expects when changing the geometry (for example, the channel pinch-off gate voltage V_{po} and subband spacing $\hbar\omega_{12}$). This confirms that these QPCs had saddle-point potentials that were smooth enough for showing quantized conductance, while it also shows that the many-body effects are very sensitive to small static fluctuations on these saddle-point potentials (see also Fig. 3.6), or to nanoscale device-to-device variations in the dimensions of the potentials. This picture was confirmed by shifting the channel position inside a particular QPC_{2F} device. This can be implemented by operating a QPC_{2F} with a difference ΔV_g between the values of V_g on the two gate fingers in Fig. 5.1a. Such a channel shift did not change the quantized conductance significantly, but did cause strong variation in the signatures of many-body physics. Earlier work had established that such device-to-device fluctuations can be due to remote defects or impurities [7], a slight variation in electron density [8], or due to the nanoscale variation in devices that is inherent to the nanofabrication process. Consequently, studying how the many-body effects depend on the length of the QPC channel requires QPCs for which the channel length can be tuned continuously *in situ*, and where this can be operated without a transverse displacement of the QPC channel in the semiconductor material. The work that we report here aimed at realizing such devices.

This Chapter is organized as follows: Section 5.2 starts with a short overview of the options and the choices we made for realizing the QPC_{6F} devices. Next, in Section 5.3, we present the results of electrostatic simulations. In Section 5.4, we describe the sample fabrication and measurement techniques. This is followed by comparing results from simulations and experiments for QPC_{6F} devices in Section 5.5, and Section 5.6 summarizes our conclusions.

5.2 Design considerations

We designed our QPC_{6F} devices with 6 rectangular gate fingers, in a symmetric layout with two sets of 3 parallel gate fingers (Fig. 5.1b and Fig. 5.2a). SEM inspection of fabricated devices yields that the central gate finger is 200 nm wide (as measured along the direction of channel length L_{eff}). The outer gate fingers are 160 nm wide, and the narrow gaps between gate fingers are 44 nm wide. This yields $(200 + 2 \cdot 160 + 2 \cdot 44)$ nm = 608 nm for the total distance between the outer sides of the 3 parallel gate fingers. The lithographic width of the QPC channel

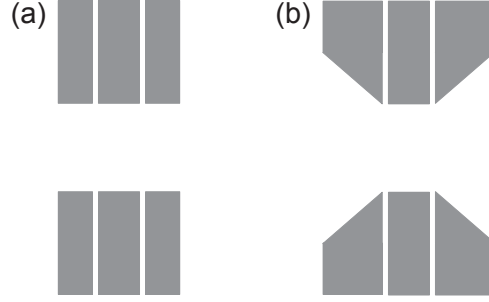


Figure 5.2: (a) Design of the geometry of the 6 gate fingers for a QPC_{6F} device with 6 rectangular gate fingers. (b) Design of a QPC_{6F} device with the 4 outer gates in a shape that explicitly induces a funnel shape for the entry and exit of the QPC transport channel.

(distance between the two sets of 3 gate fingers) is 350 nm.

An example of alternative designs for the gate geometries that we considered is in Fig. 5.2b. This design has a two-sided funnel shape for the channel and this could result in length-tunable QPC operation that better maintains a regular shape for the saddle-point potential. However, the electrostatic simulations in Section 5.3 show that the rectangular gate fingers as in Fig. 5.2a also give a length-tunable saddle-point potential that maintains a regular shape while tuning the length. This observation holds for a range of device dimensions similar to our design. For our particular design, the lithographic length and width (350 nm) of the channel are comparable, and the 2DEG is as far as 110 nm distance below the surface (and the part in the center of the channel that actually contains electrons is very narrow, about 30 nm). In this regime, the saddle-point potential is strongly rounded with respect to the lithographic shapes of the gates (see for example Fig. 5.3c,d). An important advantage of the rectangular design is that it provides two clear points for calibrating the effective channel length L_{eff} : Operating at $V_{g2}/V_{g1} = 0$ gives $L_{eff} = L_{litho}$ for the central gate finger alone (200 nm, see Fig. 5.1b), while operating at $V_{g2}/V_{g1} = 1$ gives L_{eff} equal to the lithographic distance between the outer sides of the 3 parallel gate fingers (608 nm).

A point of concern for this design that deserves attention is whether the narrow gaps between the 3 parallel gate fingers induce significant structure on the saddle-point potential. The electrostatic simulations show that this is not the case (see again the examples in Fig. 5.3c,d). The part of the channel that contains electrons is relatively far away from the gate electrodes, and the potential U at

this location is strongly rounded. Notably, the full height of the potentials in Fig. 5.3 is about 1 eV, while the occupied subbands are at a height of only about 10 meV above the stationary point of the saddle-point potential (in the center of the channel). Such gaps between parallel gate electrodes can be much narrower when depositing a wider gate on top of the central gate, with an insulating layer between them. We chose against applying this idea since we also aimed to have devices with a very low level of noise and instabilities from charge fluctuations at defect and impurity sites in the device materials. In this respect, we expect better behavior when all gate fingers are deposited in a single fabrication cycle, and when deposition of an insulating oxide or polymer layer can be omitted.

5.3 Electrostatic simulations

This section presents results of electrostatic simulations of the saddle-point potentials that define the QPC channel. The focus is on the design with 6 rectangular gate fingers (Fig. 5.2a), with gate dimensions as mentioned in the beginning of Section 5.2. The simulations are based on the modeling approach that was introduced by Davies *et al.* [9].

5.3.1 Davies' method for simulating 2DEG electrostatics

Davies *et al.* [9] introduced a method for modeling the electrostatics of gated 2DEG. It calculates the electrostatic potential U for electrons in the 2DEG regions around the gates (the approach only applies to the situation where the 2DEG underneath the gates is depleted due to a negative voltage on gate electrodes). There are other models and approaches [8, 10, 11, 12, 13] for calculating such potential landscapes, but these are all more complicated and computationally more demanding. The approach by Davies *et al.* is relatively simple. It does not account for electrostatic screening effects, and, notably, it does not account for the electron many-body interactions that were mentioned earlier. Still, it was shown that it is well suited for calculating a valid picture of a QPC saddle-point potential near the channel pinch-off situation [6].

The negative voltage on a gate that is needed to exactly deplete 2DEG underneath a large gate is called the threshold voltage V_t , and it is to a good approximation given by

$$V_t = \frac{-en_2Dd}{\epsilon_r\epsilon_0}. \quad (5.1)$$

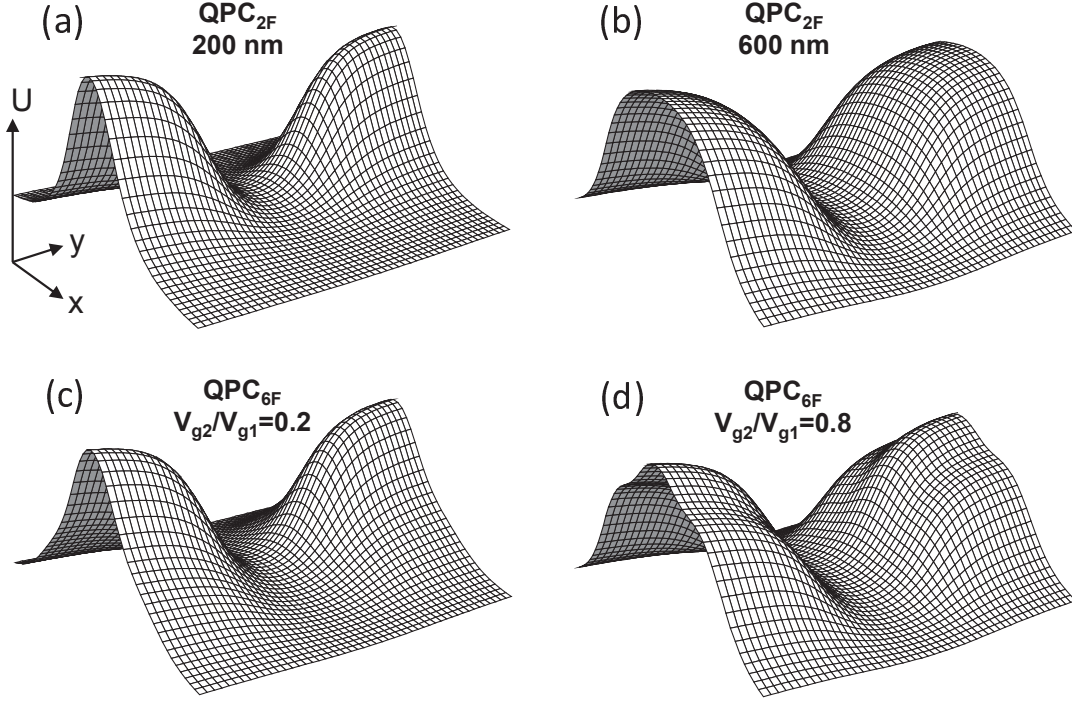


Figure 5.3: (a),(b) Saddle-point potentials that represent the electrostatic potential U felt by electrons in the 2DEG plane. The plots represent an area of $1000 \times 1000 \text{ nm}^2$, centered at the middle of a QPC channel with a length L_{litho} of 200 nm (a) and 600 nm (b) of a QPC_{2F} device with a lithographic channel width of 350 nm. It is calculated for the material parameters that are valid for the measured devices. See Fig. 5.1b for relating the x - and y -direction to the gate geometry. (c),(d) Similar saddle-point potentials U calculated for QPC_{6F} devices (with material parameters and geometry as the measured devices). The effective channel length is shorter for the case that is calculated for $V_{g2}/V_{g1} = 0.2$ (c) than for the case $V_{g2}/V_{g1} = 0.8$ (d) (also note that QPC_{6F} results for $V_{g2}/V_{g1} = 0$ are the same as plot (a)). Panel (c) and (d) also show that the narrow gaps between 3 parallel gate fingers do not induce significant structure at low energies in the saddle-point passage (it only induces a weak fingerprint off to the side in the channel, at energies that are much higher than the occupied electron levels, see panel (d)).

Here n_{2D} is the electron density in the 2DEG (at zero gate voltage), d is the depth of the 2DEG, ϵ_r is the relative dielectric constant of the material below the gate, and ϵ_0 is the dielectric constant of vacuum (for details see Ref. [6, 9]). The value of V_t for a certain 2DEG material defines the value U_0 where the electrostatic potential U for electrons in the 2DEG becomes higher than the chemical potential of the 2DEG. In turn, this can be used to define in an arbitrary

potential landscape U (for arbitrary gates shapes and for arbitrary gate voltages) the positions where $U = U_0$. That is, one can calculate the positions in a gated device structure where there is a boundary between depleted and non-depleted 2DEG, and also calculate the electrostatic potential U around such points. When the center of the QPC has $U = U_0$, the channel is at pinch-off and no electrons can pass through the QPC. The gate voltage at which this happens is called the pinch-off voltage V_{po} . Notably, the calculated value of U at a certain position is simply the superposition of all the contributions to U from different gate electrodes, and it is linear in the gate voltage on each of these electrodes [9].

Figure 5.3 presents examples of saddle-point potentials U that are calculated with Davies' method, both for QPC_{2F} and QPC_{6F} devices. The calculations are for material parameters and geometries of measured devices (as described in detail in the next sections). Figures 5.3c,d show that the length of the transport channel depends on the applied ratio V_{g2}/V_{g1} , and that the narrow gaps between 3 parallel electrodes in QPC_{6F} devices do not give significant structure on the saddle-point potential in the operation regime that we consider.

5.3.2 Definition and tuning of the effective length L_{eff}

The focus of this work is on realizing QPC channels with a tunable length. The channels are in fact saddle-point potentials (see Fig. 5.3), and it is for such a smooth shape not obvious what the value is of the channel length. We therefore characterize this channel length with the parameter L_{eff} , which corresponds to the value of the lithographic length L_{litho} of a QPC_{2F} type device (with rectangular gate electrodes, see Fig. 5.1a) that gives effectively the same saddle-point potential.

We implemented this as follows. We calculated the saddle-point potential $U(x, y)$ for the pinch-off situation (see Fig. 5.1b and Fig. 5.3a for how the x - and y -directions are defined). The transverse confinement in this potential is in the middle of the QPC (defined as $x = 0$, $y = 0$) parabolic to a very good approximation. When moving out of the channel along the x -direction, the transverse confinement becomes weaker, but remains at first parabolic. Notably, the energy eigenstates for confinement in such a parabolic potential, described as

$$U(y) = \frac{1}{2}m^*\omega_0^2y^2, \quad (5.2)$$

have a width that is (for all levels) proportional to $\omega_0^{-1/2}$. In this expression m^* is the effective mass of the electron, and ω_0 is the angular frequency of natural

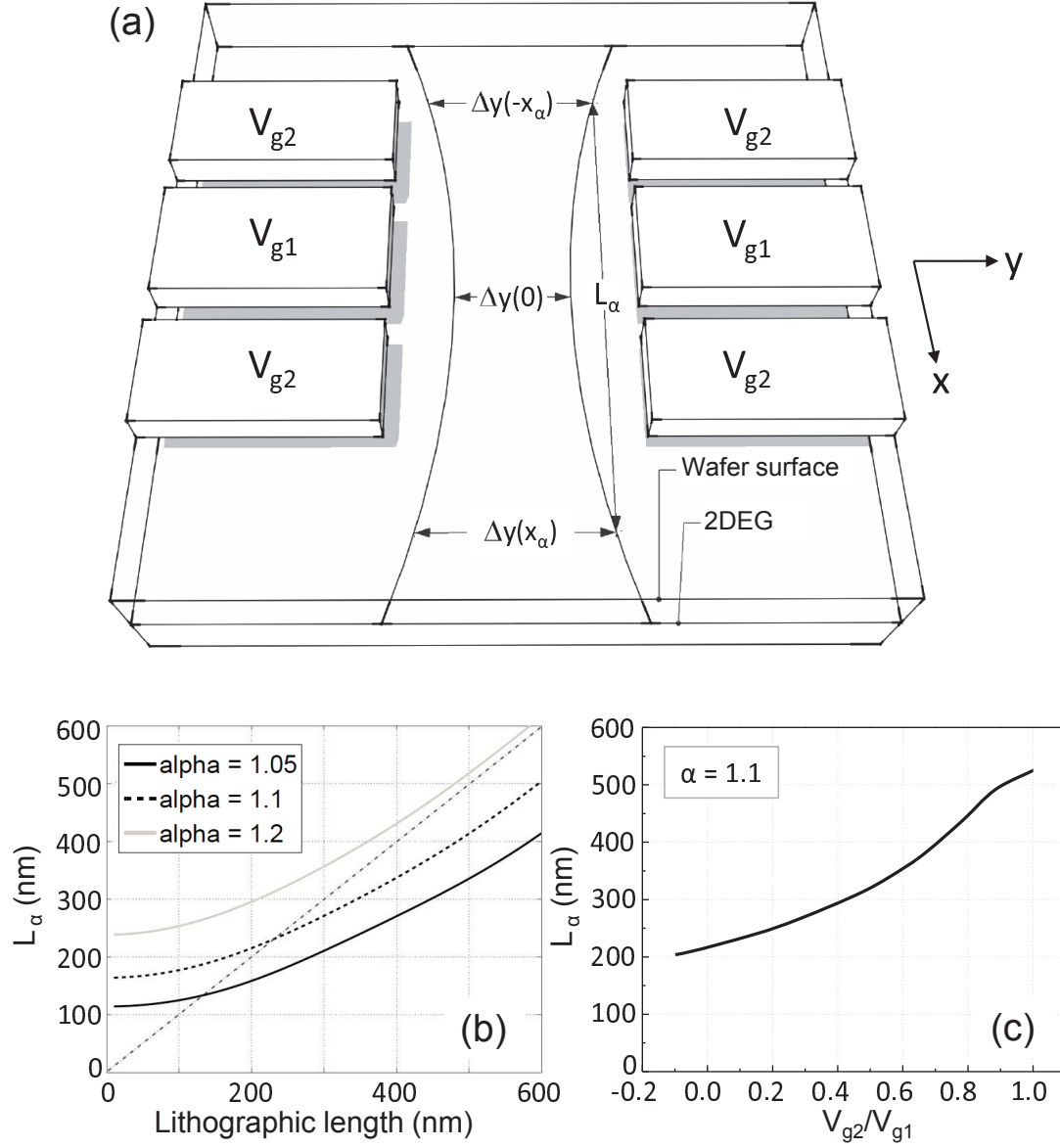


Figure 5.4: (a) Schematic representation of a QPC_{6F} device, illustrating length variables that are introduced in the main text. (b) The calculated length L_α for a range of values of the lithographic length of QPC_{2F} devices, for three values of α . (c) The calculated effective length L_α for $\alpha = 1.1$ for a QPC_{6F} device, as a function of the ratio V_{g2}/V_{g1} .

oscillations in this potential. The parameter ω_0 defines here the steepness of $U(y)$, and we obtain $\omega_0(x)$ values from fitting Eq. 5.2 to potentials $U(x, y)$ obtained with Davies's method. We use this and investigate the width $\Delta y(x)$ in y -direction for the lowest energy eigenstate, at all positions x along the channel (see Fig. 5.4a). For parabolic confinement this wavefunction in y -direction has a Gaussian shape and has a width

$$\Delta y(x) = \sqrt{\frac{h}{4\pi m^* \omega_0(x)}}. \quad (5.3)$$

With this approach we analyzed that the distance from $x = 0$ to the x -position x_α where the value $\Delta y(x)$ increased by a factor $\alpha \approx 1.1$ defines a suitable point for defining the value of L_{eff} . That is, we define

$$L_\alpha = 2 x_\alpha, \quad (5.4)$$

and find x_α by solving

$$\Delta y(x = x_\alpha) = \alpha \cdot \Delta y(x = 0) \quad (5.5)$$

for a certain α . Subsequently, L_{eff} is defined by using the suitable α value,

$$L_{eff} = L_\alpha \text{ for } \alpha = 1.1. \quad (5.6)$$

We came to this parameterization as follows. We used this *ansatz* first in simulations of QPC_{2F} devices. Here, we explored for different values of α the relation between L_{litho} and L_α . Results of this for $\alpha = 1.05, 1.1$ and 1.2 are presented in Fig. 5.4b. For the range of L_{litho} values that is of interest to our study (~ 100 nm to ~ 500 nm), we find the most reasonable overall agreement between the actual value for L_{litho} (input to the simulation) and the value L_α (derived from the simulation) for $\alpha = 1.1$. The agreement is not perfect, but we analyzed that the deviation is within an uncertainty that we need to assume because the exact shapes of saddle-point potentials in different device geometries do show some variation, and because the limited validity of Davies' method. Nevertheless, it provides a reasonable recipe for assigning a value L_{eff} to any saddle-point potential, with at most 20% error.

Fig. 5.4c presents results of calculating $L_\alpha = L_{eff}$ for $\alpha = 1.1$ from simulations of a QPC_{6F} device, operated at different values for V_{g2}/V_{g1} . The results show a clear monotonic trend, with $L_{eff} = 210$ nm for $V_{g2}/V_{g1} = 0$ to $L_{eff} = 525$ nm for $V_{g2}/V_{g1} = 1$. This is for a QPC_{6F} device for which we expect $L_{eff} = 200$ nm

for $V_{g2}/V_{g1} = 0$ and $L_{eff} = 608$ nm for $V_{g2}/V_{g1} = 1$ (see Section 5.2). In Section 5.5 we discuss how this latter point is used for applying a small correction to the simulated values for L_{eff} . These simulations show that the QPC_{6F} that we consider allows for tuning L_{eff} by about a factor 3.

It is worthwhile to note that our current design showed optimal behavior in the sense that it can tune L_{eff} from about 180 nm to 600 nm, while the dependence of L_{eff} on V_{g2}/V_{g1} is close to linear. We also simulated QPC_{6F} devices with wider gate electrodes for the outer gates, and (as mentioned in Section 5.2) devices with gate geometries as in Fig. 5.2b. These devices showed a steeper slope for part of the relation between V_{g2}/V_{g1} and L_{eff} , which is not desirable.

5.4 Sample fabrication and measurement techniques

We fabricated QPC devices with a GaAs/Al_{0.35}Ga_{0.65}As MBE-grown heterostructure, which has a 2DEG at 110 nm depth below its surface from modulation doping. The layer sequence and thickness of the materials from top to bottom (*i.e.* going into the material) starts with a 5 nm GaAs capping layer, then a 60 nm Al_{0.35}Ga_{0.65}As layer with Si doping at about $1 \times 10^{18} \text{ cm}^{-3}$, which is followed by an undoped spacer layer of 45 nm. The 2DEG is located in a heterojunction quantum well at the interface with the next layer, which is a 650 nm undoped GaAs layer. This heterostructure was grown on a commercial semi-insulating GaAs wafer, after first growing a sequence of 10 GaAs/AlAs layers for smoothing the surface and trapping impurities. The 2DEG had an electron density $n_{2D} = 1.6 \cdot 10^{15} \text{ m}^{-2}$ and a mobility $\mu = 118 \text{ m}^2 \text{ V}^{-1} \text{ s}^{-1}$. We fabricated both conventional QPC_{2F} devices and QPC_{6F} devices by standard electron-beam lithography and clean-room techniques. The gate fingers were deposited using 15 nm Au on top of a 5 nm Ti sticking layer. For measuring transport through the QPCs we realized ohmic contacts to the 2DEG reservoirs by annealing of a AuGe/Ni/Au stack that was deposited on the wafer surface [14]. The geometries of the fabricated devices were already described in the beginning of Section 5.2.

The measurements were performed in a He-bath cryostat and in a dilution refrigerator, thus getting access to effective electron temperatures from 80 mK to 4.2 K. We used standard lock-in techniques with an a.c. excitation voltage $V_{bias} = 10 \text{ } \mu\text{V}$ RMS at 387 Hz. Fig. 5.1a shows the 4-probe voltage-biased measurement scheme, where both the current and the actual voltage drop V_{sd}

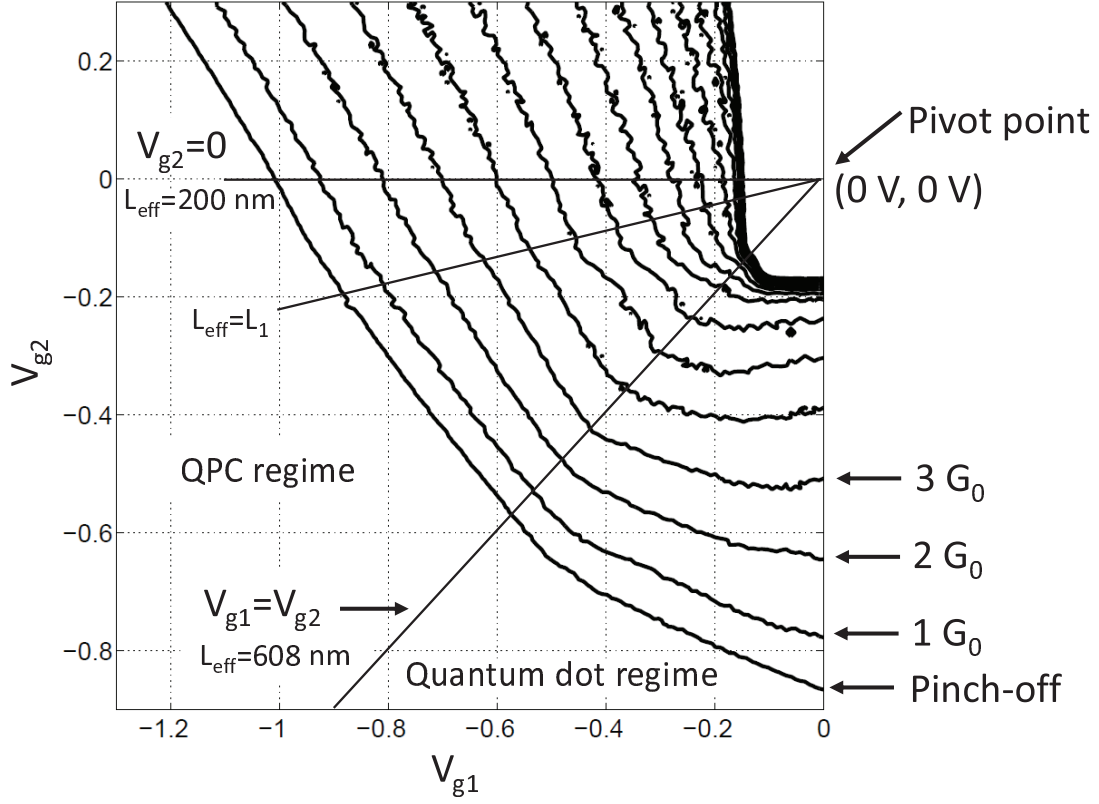


Figure 5.5: QPC linear conductance as a function of V_{g1} and V_{g2} for a QPC_{6F} device, presented in the form of iso-conductance lines at integer G_0 levels. The conductance was measured at 4.2 K where the quantized conductance is nearly fully washed out by temperature. The two operational regimes above and below the line $V_{g1} = V_{g2}$ yield QPC and quantum dot behavior, respectively.

across the QPC channel are measured such that any influence of series resistances could be removed unambiguously. The gate voltages are applied with respect to a single grounded point in the loop that carries the QPC current.

5.5 Experimental realization of length-tunable QPCs

This section presents an experimental characterization of the QPC_{6F} devices that we designed (Fig 5.1b) and we compare the results to our simulations. Figure 5.5 presents measurements of the conductance G as a function of V_{g1} and V_{g2} . Several labels in the plot illustrate relevant concepts, which were partly discussed before. For the area in this plot with V_{g2} more negative than V_{g1} we expect some quantum-

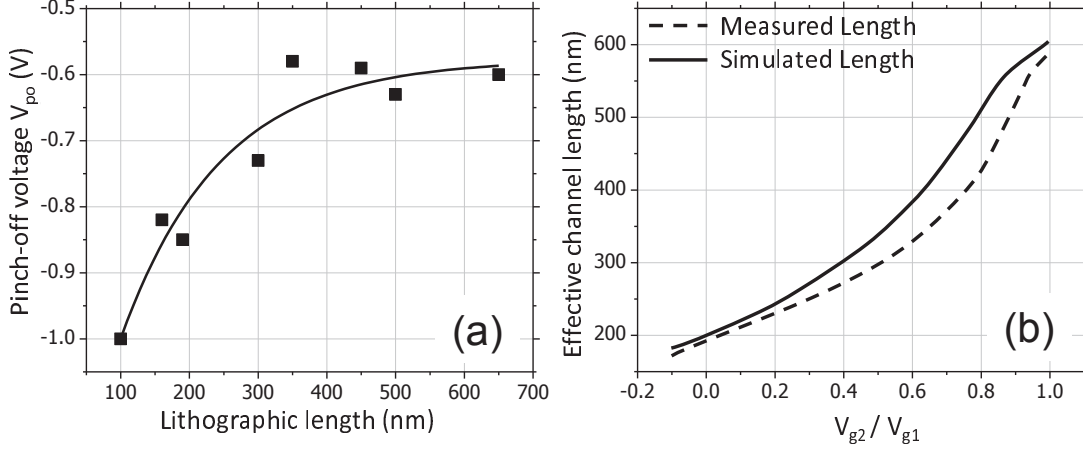


Figure 5.6: (a) Experimentally determined relation between the pinch-off gate voltage V_{po} and the lithographic length of QPC_{2F} devices. Points are experimental results. The solid line is a phenomenological expression that was used for parameterizing the relation between V_{po} and the lithographic length. (b) Comparison between measured and simulated values of the effective channel length for a QPC_{6F} device.

dot like localization in the middle of the channel and this regime should therefore be avoided in studies of QPC behavior. Further, the plot illustrates that operation for a particular value of L_{eff} requires co-sweeping of V_{g1} and V_{g2} from a particular point below pinch-off in a straight line to the pivot point. This corresponds to opening the QPC at a fixed ratio for V_{g2}/V_{g1} . The pivot point is the point where the gate voltages do not alter the original electron density of the 2DEG. For this measurement this is for $V_{g1} = V_{g2} = 0$ V, but this is different for the case of biased cool downs. We carried out biased cool downs for suppressing noise from charge instabilities in the donor layer [15, 16]. For such experiments the QPCs were cooled down with a positive voltage on the gates. We typically used +0.3 V, and observed indeed better stability with respect to charge noise. The effect of such a cool down can be described as a contribution to the gate voltage of -0.3 V that is frozen into the material [15, 16]. Consequently, co-sweeping of V_{g1} and V_{g2} for maintaining a fixed channel length must now be carried out with respect to the pivot point $V_{g1} = V_{g2} = +0.3$ V instead of $V_{g1} = V_{g2} = 0$ V.

The theory behind the Davies method illustrates why operation at fixed effective length requires a fixed ratio V_{g2}/V_{g1} . All points in the potentials landscapes U for QPC_{2F} devices as in Fig. 5.3a,b have a height that scales linear with the gate voltage V_g . Thus, when opening the QPC the full saddle-point potential changes height at a fixed shape. Mimicking this situation with QPC_{6F} devices requires

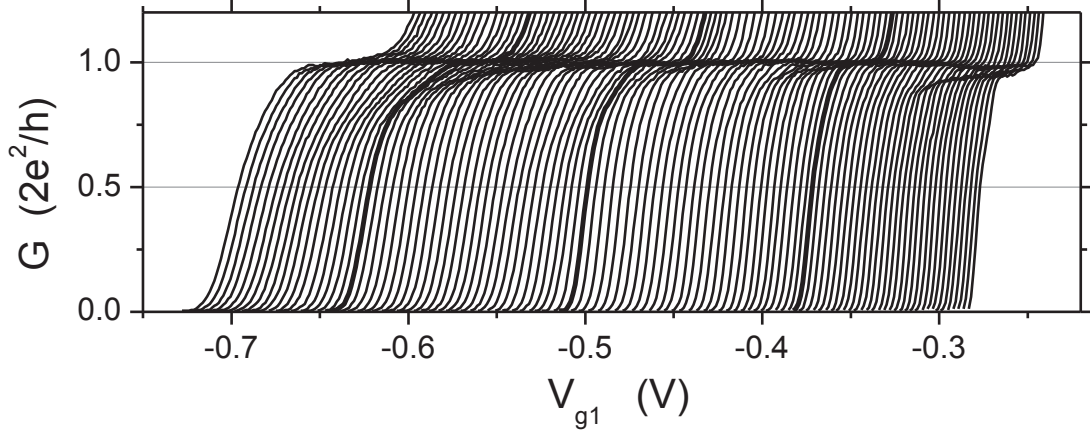


Figure 5.7: The linear conductance G as a function of V_{g1} for a QPC_{6F} device, measured at 80 mK. Different traces are for fixed ratio $V_{g2}/V_{g1} = 0$ to $V_{g2}/V_{g1} = 1$ (left to right, traces *not* offset), which corresponds to increasing the effective channel length L_{eff} from 200 nm to 608 nm.

a fixed ratio V_{g2}/V_{g1} , again because V_{g1} and V_{g2} influence U in a linear manner. The plot also illustrates the two special operation lines where the effective length of the channel is unambiguous, and we used these points to better calibrate the relation between V_{g2}/V_{g1} and L_{eff} . The first case is the line at $V_{g2} = 0$, which yields $L_{eff} = 200$ nm, as defined by the central gates alone. The second case is the line $V_{g1} = V_{g2}$. Here L_{eff} is 608 nm, as defined by the full lithographic length of the 3 gate fingers.

We improved and further checked our calibration of the relation between V_{g2}/V_{g1} and L_{eff} as follows. We used the trend that came out of the simulations (Fig. 5.4c), but pinned the curve at 200 nm for $V_{g2}/V_{g1} = 0$ and at 608 nm for $V_{g2}/V_{g1} = 1$ (black line in Fig. 5.6b). This trace shows good agreement with results from an independent check (dashed line) that used the pinch-off gate voltage V_{po} as an identifier for the effective length. This independent check used data from a set of QPC_{2F} devices for calibrating the relation between L_{litho} and V_{po} (Fig. 5.6a). This shows the trend that shorter QPC_{2F} devices require a more negative gate voltage to reach pinch-off [17]. We related this to the pinch-off values in QPC_{6F} devices. In particular, we analyzed the pinch-off points on the V_{g1} axis, and its dependence on V_{g2}/V_{g1} (see also Fig. 5.7). The results of using this for assigning a certain L_{eff} to each V_{g2}/V_{g1} is the red dashed line in Fig. 5.6b, and shows good agreement with the values that were obtained from simulations. We can thus assign a value to L_{eff} for each V_{g2}/V_{g1} with an absolute error that is at most 50 nm. Notably, the relative error when describing the increase in L_{eff}

upon increasing V_{g2}/V_{g1} is much smaller.

The results in Fig. 5.7 provide an example of linear conductance measurements on a QPC_{6F} device at 80 mK. The traces show clear quantized conductance plateaus for all settings of L_{eff} . Several of these linear conductance traces also show the 0.7 anomaly, and the strength of its (here rather weak) expression shows a modulation as a function of L_{eff} over about 3 periods. A detailed study of this type of periodicity can be found in Ref. [18]. This example illustrates the validity and importance of our type of QPCs in studies of length-dependent transport properties.

5.6 Conclusions

We have developed and characterized length-tunable QPCs that are based on a symmetric split-gate geometry with 6 gate fingers. Gate structures with different shapes and dimensions can be designed depending upon the required range for length tuning and for optimizing the tuning curve. For our purpose (QPCs with an effective channel length between about 180 nm and 600 nm, and 350 nm channel width) we found that simple rectangular gate fingers are an attractive choice. Our simulations and experimental results are in close agreement. We were able to tune the effective length by about a factor 3, from 180 nm to 608 nm. QPCs are the simplest devices that show clear signatures of many-body physics, as for example the 0.7 anomaly and the Zero-Bias Anomaly (ZBA) [19]. Our length-tunable QPCs provide an interesting platform for systematically investigating these many-body effects. In particular, these QPCs provide a method for studying the influence of the QPC geometry without suffering from device-to-device fluctuations that hamper such studies in conventional QPCs with 2 gate fingers. Studies in this direction are presented in Ref. [18].

We thank B. H. J. Wolfs for help and the German programs DFG-SPP 1285, Research school Ruhr-Universität Bochum and BMBF QuaHL-Rep 01BQ1035 for financial support.

Bibliography

- [1] B. J. van Wees *et al.*, Phys. Rev. Lett. **60**, 848 (1988).
- [2] D. A. Wharam *et al.*, J. Phys. C **21**, L209 (1988).
- [3] K. J. Thomas *et al.*, Phys. Rev. Lett. **77**, 135 (1996).

- [4] A. P. Micolich, J. Phys.: Condens. Matter **23**, 443201 (2011).
- [5] T. Rejec and Y. Meir, Nature **442**, 900 (2006).
- [6] E. J. Koop *et al.*, J. Supercond. Novel Magn. **20**, 433 (2007).
- [7] D. H. Cobden *et al.*, Phys. Rev. B **44**, 1938 (1991).
- [8] J. A. Nixon and J. H. Davies, Phys. Rev. B **41**, 7929 (1990).
- [9] J. Davies, I. A. Larkin, and E. V. Sukhorukov, J. Appl. Phys. **77**, 4504 (1995).
- [10] G. L. Snider, I. H. Tan, and E. L. Hu, J. Appl. Phys. **68**, 2849 (1990).
- [11] M. Chen, W. Porod, and D. J. Kirkner, J. Appl. Phys. **75**, 2545 (1994).
- [12] S. E. Laux, D. J. Frank, and F. Stern, Surf. Sci. **196**, 101 (1988).
- [13] J. A. Nixon and J. H. Davies, Phys. Rev. B **43**, 12638 (1991).
- [14] M. J. Iqbal *et al.*, available as Chapters 6 and 7 in this thesis.
- [15] M. Pioro-Ladriere *et al.*, Phys. Rev. B **101**, 226603 (2005).
- [16] C. Buizert *et al.*, Phys. Rev. Lett. **72**, 115331 (2008).
- [17] H.-M. Lee *et al.*, J. Appl. Phys. **100**, 043701 (2006).
- [18] M. J. Iqbal *et al.*, available as Chapter 4 in this thesis.
- [19] S. M. Cronenwett *et al.*, Phys. Rev. Lett. **88**, 226805 (2002).

Chapter 6

The annealing mechanism of AuGe/Ni/Au ohmic contacts to a two-dimensional electron gas in GaAs/Al_xGa_{1-x}As heterostructures

Abstract

Ohmic contacts to a two-dimensional electron gas (2DEG) in GaAs/Al_xGa_{1-x}As heterostructures are often realized by annealing of AuGe/Ni/Au that is deposited on its surface. We studied how the quality of this type of ohmic contact depends on the annealing time and temperature, and how optimal parameters depend on the depth of the 2DEG below the surface. Combined with transmission electron microscopy and energy-dispersive X-ray spectrometry studies of the annealed contacts, our results allow for identifying the annealing mechanism and proposing a model that can predict optimal annealing parameters for a certain heterostructure.

This chapter is based on Ref. 4 on p. 159.

6.1 Introduction

Epitaxially grown GaAs/Al_xGa_{1-x}As heterostructures that contain a two-dimensional electron gas (2DEG) are widely used for electron transport studies in low-dimensional systems [1, 2]. Establishing electrical contacts to the 2DEG is a crucial step in device fabrication with these heterostructures. A commonly used recipe for making ohmic contacts is annealing of a AuGe/Ni/Au alloy that has been deposited on the heterostructure surface [3]. High-quality heterostructures are often only available in a limited quantity, and it is desirable to minimize the heating that is needed for annealing the contacts to avoid damaging the heterostructure. A model that predicts optimal annealing times and temperatures for a heterostructure with the 2DEG at a certain depth is therefore very valuable.

We present here a study of the annealing mechanism for this type of ohmic contact, and a model that can predict optimal annealing parameters for a certain heterostructure. We used electron transport experiments to study how the quality of AuGe/Ni/Au based ohmic contacts depends on annealing time and temperature, and how the optimal parameters change with the depth of the 2DEG below the surface. These results confirm that the annealing mechanism cannot be described by a single simple diffusion process. Cross-sectional studies of annealed contacts with Transmission Electron Microscope (TEM) and Energy Dispersive X-ray (EDX) techniques were used for identifying a more complex annealing mechanism, that is in agreement with the results from our electron transport studies.

The AuGe/Ni/Au contact was first introduced by Braslau *et al.* [4] to contact n-GaAs, and several studies aimed at understanding the contact mechanism for this type of contact [5, 6, 7, 8, 9, 10, 11, 12, 13, 14, 15, 16, 17, 18]. Later studies focussed on the formation of an ohmic contact to a 2DEG in a GaAs/Al_xGa_{1-x}As heterostructure [19, 20, 21, 22, 23, 24, 25, 26, 27], but do not report how the optimal annealing parameters depend on the depth of the 2DEG below the surface. A number of these studies suggest that a contact is formed because a pattern of Au/Ni/Ge spikes that originate from the metallization penetrate the heterostructure, just beyond the depth of the 2DEG [23, 25]. Earlier work had already suggested that in good contacts Ni-rich phases may form at the depth of the 2DEG, in contact with the GaAs below the Al_xGa_{1-x}As [19]. We observe, instead, a mechanism where metal-rich phases only penetrate the heterostructure over a distance that is shorter than the depth of the 2DEG. The mechanism that results in a good contact is then similar to a process that has been described [9]

for contacts to n-GaAs: during annealing, the AuGe/Ni/Au on the surface segregates in Ni-rich and Au-rich domains, where the Ni domains contain most of the Ge. These domains penetrate the heterostructure and grow towards the 2DEG in large grains rather than narrow spikes. For optimal electrical contact conditions the Au and Ni-rich grains do not reach the 2DEG. The contact resistance decreases and the contact becomes ohmic because Ge diffuses deeper, forming a highly doped $\text{Al}_x\text{Ga}_{1-x}\text{As}$ region between the 2DEG layer and metal-rich phases at the surface. We find that even for very long annealing times, when the contact resistance has significantly increased compared to the optimal contact, the Au and Ni-rich phases still do not penetrate the 2DEG.

The outline of this article is as follows: we first describe our wafer materials and device fabrication. Next, we present electrical measurements and use these to identify annealed contacts with optimal ohmic properties. In Section 6.4 we present the results of our TEM and EDX studies of annealed contacts. Section 6.5 then summarizes the annealing mechanism that we identified, and this is used in Section 6.6 to propose a model that can predict optimal annealing parameters. Finally, in Section 6.7, we present a study of how the contact resistance depends on the shape of the contact (varying area or circumference), which gives further insight in the annealing mechanism and the electrical contact properties.

6.2 Device fabrication

We studied annealed AuGe/Ni/Au contacts to three GaAs/ $\text{Al}_x\text{Ga}_{1-x}\text{As}$ heterostructures, grown on (001)-oriented i-GaAs substrates, with the 2DEG at a heterojunction at 70 nm (wafer A), 114 nm (wafer B), and 180 nm (wafer C) below the surface of the wafer. These wafers have similar values for the 2DEG electron density n_s and mobility μ (around $2 \cdot 10^{15} \text{ m}^{-2}$ and $100 \text{ m}^2/\text{Vs}$, respectively, results for 4.2 K and samples kept in the dark during cool down). For all three wafers the layer sequence (from the surface down) is very similar besides the depth of the 2DEG. The top layer is a ~ 5 nm n-GaAs capping layer, then an $\text{Al}_x\text{Ga}_{1-x}\text{As}$ doping layer (Si at $\sim 1 \cdot 10^{18} \text{ cm}^{-3}$) with $x \approx 0.32$, of thickness 30 nm (A), 72 nm (B) or 140 nm (C). After this follows an undoped $\text{Al}_x\text{Ga}_{1-x}\text{As}$ buffer layer (~ 35 nm thick). The 2DEG is located at the interface with the next layer, which is a several μm thick undoped GaAs layer.

We studied $200 \times 200 \mu\text{m}^2$ contacts that were defined by optical lithography on a 1 mm wide and 2 mm long etched mesa with a typical Hall-bar geometry. An electron-beam evaporator was used for deposition of subsequently 150 nm AuGe

of eutectic composition (12 wt% Ge), 30 nm of Ni and 20 nm of Au. Subsequent annealing took place in a pre-heated quartz furnace tube with a clean N_2 flow of about 1 cm/s over the sample to prevent oxidation. We also found that using a much weaker N_2 flow could result in surface contamination that was electrically conducting. We have used three different annealing temperatures, 400 °C, 450 °C and 500 °C. The samples were placed on a quartz boat and then moved into the center of the oven for various annealing times. Figure 6.1a shows the temperature of the surface of the quartz boat as a function of time for an oven temperature of 450 °C. We assume that the sample temperature closely follows the temperature of the quartz boat, since we assured a good thermal contact over the full surface of the sample.

6.3 Electrical measurements

We measured the current-voltage (IV) characteristics of all contacts to determine optimal annealing parameters. We found that a suitable and sufficient definition for an optimal ohmic contact is a contact with the lowest zero-bias resistance at 4.2 K. The typical resistance for such a contact is $\sim 20 \Omega$, but we have observed resistances as low as 5Ω . These values for contact resistance are close to the lowest values that have been reported [28]. All contacts defined as optimal in this manner showed highly linear IVs up to at least 1 mV (over and under annealed contacts did show non-linear IVs due to effects like Schottky or tunnel barriers in the contacts). Further, all these optimal contacts showed a strong monotonous reduction of the contact resistance upon lowering the sample temperature from 300 K to 4.2 K. Highly over and under annealed contacts showed an increase of the contact resistance upon cooling to 4.2 K.

We used a current-biased 4-terminal configuration to measure the voltage drop across a single contact, with two terminals attached to the metal bond wire that is pressed onto the ohmic contact, and two terminals attached to the 2DEG via other ohmic contacts (this allowed us to use a standard sample design in our fabrication facility). We accounted for a small voltage drop in the 2DEG area between the contact and the voltage probe via the 2DEG. We are aware that the Transmission Line Method (TLM) [29, 30] is a better method for determining the exact value of a contact resistance, but this is not needed for our approach. We compare resistances of various annealed contacts that were fabricated under identical conditions besides the variation in annealing time and temperature. Within such a set, we determine which contacts have the lowest contact resistance.

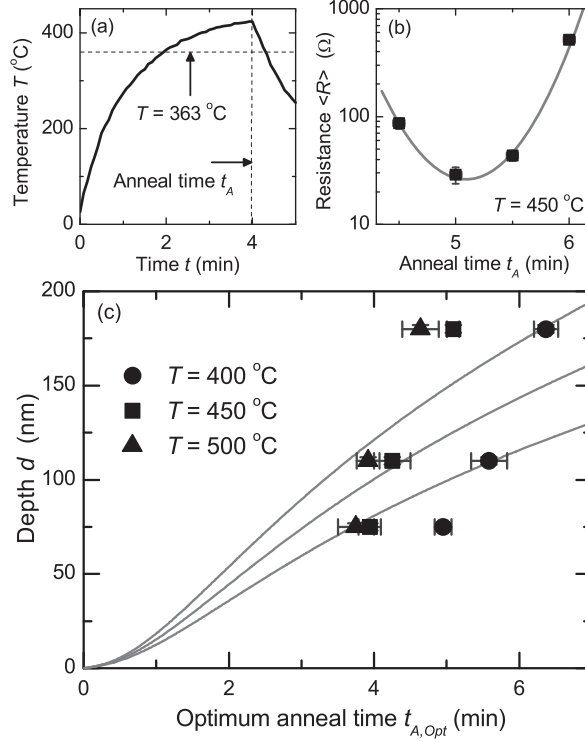


Figure 6.1: (a) Temperature of the quartz boat as a function of time for an oven temperature of 450 °C. Horizontal dashed line indicates the AuGe melting temperature $T = 363$ °C. The vertical dashed line indicates our definition of the annealing time t_A , the time at which the boat is taken out of the oven. (b) Average contact resistance $\langle R \rangle$ as a function of annealing time t_A for contacts on wafer C, annealed at 450 °C. A parabolic fit is made to estimate the annealing time where the resistance has a minimum. (c) Overview of optimal annealing times $t_{A,Opt}$ as a function of depth d of the 2DEG beneath the wafer surface for $T = 400, 450$ and 500 °C. The three gray lines (bottom to top for 400, 450 and 500 °C) are results of fitting a simple diffusion model to the experimental data (see text), which does not yield a good fit.

When reproducing our results with contacts that were fabricated in a different batch (using the same electron-beam evaporator, but after replenishing the AuGe target), we find that the values of the lowest contact resistance can be different up to a factor 2 around the typical result. We attribute these batch-to-batch fluctuations to variations in the exact composition of the AuGe/Ni/Au layer that we deposit. The optimal annealing times, however, show batch-to-batch fluctuations of only 10%. Thus, our approach for determining optimal annealing conditions does not depend on the exact value of the measured contact resistance.

Figure 6.1b shows a typical result, from which we determine the optimal annealing time for contacts to wafer C for the case of annealing with the oven at 450 °C. Contact resistance data that is denoted as $\langle R \rangle$ is the average resistance measured on a set of 8 identical contacts, and the error bar represents the standard deviation. The results in Fig. 6.1b show a clear minimum in contact resistance for annealing times near 5 minutes. We fit a parabola (phenomenological ansatz) to the $\log \langle R \rangle$ values of these data points, and define the optimal annealing time as the time coordinate of the minimum of the parabola. In this manner, the optimal annealing times $t_{A,Opt}$ are obtained for contacts on wafers A, B and C, annealed at each of the temperatures.

Figure 6.1c presents these optimal annealing times. As expected, the optimal annealing time increases as the temperature is decreased, and increases as the depth d of the 2DEG increases. While it is known that several simultaneous diffusion processes play a role in contact formation [9], we will, for the sake of argument, show that a simple diffusion model has little value for predicting how optimal annealing times depend on the depth d and the annealing temperature. For this simple diffusion model, we assume that a certain dopant (with fixed concentration C_0 at the surface) diffuses into the heterostructure. The relevant solution to Fick's second law is then

$$C = C_0 \operatorname{erfc} \frac{z}{\sqrt{4Dt}}. \quad (6.1)$$

Here C is the doping concentration at time t and depth z into the heterostructure, and D is the diffusion constant (erfc is complementary error function). Since the temperature of our sample is not constant (see Fig. 6.1a) we will use the measured temperature profile $T(t)$ to integrate the diffusion constant over time, and use in Eq. 6.1 $\int D(t)dt$ instead of Dt , where

$$D(t) = D_0 \exp\left(-\frac{E_a}{k_B T(t)}\right), \quad (6.2)$$

and where E_a is an activation energy. We assume that an optimal contact then always occurs for a certain optimal value for C/C_0 at the depth of the 2DEG ($z = d$). We define the annealing time as the time from start to the moment when the boat is taken out of the oven, but integrate over the entire time span that the sample is at elevated temperatures, (as shown in Fig. 6.1a, fully including the cooling down). This gives a model with the activation energy E_a , diffusion constant D_0 and concentration C/C_0 as fitting parameters.

The gray lines in Fig. 6.1c show the best fitting result that reasonably covers all 9 data points in a single fit. Besides the fact that the shape of the traces only

poorly matches the trend in the data, the parameter values give unreasonable results. The temperature dependence alone governs the fitting result for E_a , giving here 0.15 eV. This is on the low side for typical values for diffusion in GaAs materials (~ 1 eV) [31, 32, 33]. For fixed E_a , various combinations of C/C_0 and D_0 give identical results. When assuming a typical value $D_0 \sim 3 \cdot 10^{-7} \text{ m}^2/\text{s}$ (for diffusion of Ge, Ni or Au in GaAs [31, 32, 33]), this fit yields C/C_0 very close to 1, i.e. completely saturated diffusion. This is in contradiction with the clear dependence on depth that we observe (and this remains the case when allowing for E_a up to ~ 1 eV, but then the fit does not cover all 9 data points at all). Thus, we find that predicting optimal annealing times with simple diffusion (according to $t_{A,Opt} \propto d^2$ at constant temperature) does not work and that a more complex model needs to be considered.

6.4 Cross-sectional TEM and EDX imaging

We have studied the contact formation using cross-sectional TEM imaging of contacts at several stages during the annealing process. The samples were prepared for TEM imaging by using a Focussed Ion Beam (FIB) to slice out a micrometer thin piece of the measured contact. By further thinning using the FIB the thickness was reduced to 100 nm.

Figure 6.2a shows an overview of an optimally annealed contact on wafer C which was annealed for 5 minutes at 450 °C. The composition of the various phases has been determined by Energy Dispersive X-ray (EDX) analysis and is illustrated in Fig. 6.2b. From bottom to top we recognize the GaAs substrate, and an AlAs/GaAs superlattice to smoothen the surface of the substrate. On top of that we find another layer of epitaxially grown GaAs and a layer of $\text{Al}_x\text{Ga}_{1-x}\text{As}$. The 2DEG is at the interface of these two layers. The GaAs capping layer that was originally on top of the $\text{Al}_x\text{Ga}_{1-x}\text{As}$ layer is no longer visible. Instead, we see large Au-rich and Ni-rich grains that have penetrated below the original wafer surface. Both of these phases contain out-diffused Ga and As, with Ga mainly in the Au-rich grains and As mainly in the Ni-rich grains. Further, the Ni-rich phase absorbed most of the Ge. We find that the Au grains do not contain any Ge, consistent with the findings of Kuan *et al.* [9] in work with n-GaAs.

The wide and curved dark lines going over all the heterostructure layers (most clearly visible in the GaAs layers) are due to strain induced by the FIB sample preparation and are not related to the diffusion process.

We find that the Au-rich and Ni-rich grains do not have to penetrate the

2DEG in order to establish a good electrical contact. We can rule out that we do not see grains reaching the 2DEG due to the small thickness of the sample slice, since we observed no substantial variation in the penetration depth of a large number of Au and Ni grains going along the sample slice. We examined two slices from two different samples, both with a length of 100 μm , after electrical measurements confirmed that these contacts were indeed optimally annealed.

The TEM image in Fig. 6.2c shows a larger region of an optimally annealed contact. Large Au and Ni grains that have penetrated the $\text{Al}_x\text{Ga}_{1-x}\text{As}$ layer can be identified. Figure 6.2d shows an over annealed contact on wafer C, that was annealed for 7 minutes at 450 °C. Remarkably, the Au and Ni grains did not penetrate much further into the $\text{Al}_x\text{Ga}_{1-x}\text{As}$, and do still not reach the 2DEG. The most significant change with respect to Fig. 6.2c is that the Au-rich phase is diffusing underneath the Ni-rich grains, reducing the total Ni-grain- $\text{Al}_x\text{Ga}_{1-x}\text{As}$ interface area. This was also observed by Kuan *et al.* [9] (and confirmed in detailed studies by Lumpkin *et al.* [18]) in work on n-GaAs, and the results of these authors indicate that this process is mainly responsible for the increase in contact resistance when a sample is being over annealed.

Kuan *et al.* [9] report that the contact resistance is sensitive to the ratio of the total contact area between Au-rich regions and $\text{Al}_x\text{Ga}_{1-x}\text{As}$, and that of Ni-rich regions. The Au- $\text{Al}_x\text{Ga}_{1-x}\text{As}$ interface is considered a region of poor conductance because the Au-rich grains (in contrast to Ni-rich grains) do not contain any Ge, such that it cannot act as a source for diffusion of Ge into the heterostructure. However, it is to our knowledge not yet understood why the diffusion of Au underneath the Ni grains at later stages of annealing (when a large amount of Ge already diffused out of Ni) results in a strong increase of the contact resistance.

6.5 Summary of annealing mechanism

In this Section we use the results from the previous two Sections, together with established results from the literature, for giving a qualitative description of the formation of an ohmic contact to a 2DEG in a GaAs/ $\text{Al}_x\text{Ga}_{1-x}\text{As}$ heterostructure. It is remarkably similar to the annealing mechanism as described by Kuan *et al.* [9] for contacts to n-GaAs. In the initial stages of the annealing process (already during the heating of the sample) Au and Ge segregate, and most Ge forms a new phase with the Ni. At the same time, these Ge-rich Ni grains move to the wafer surface due to a wetting effect [16], which results in the situation that the

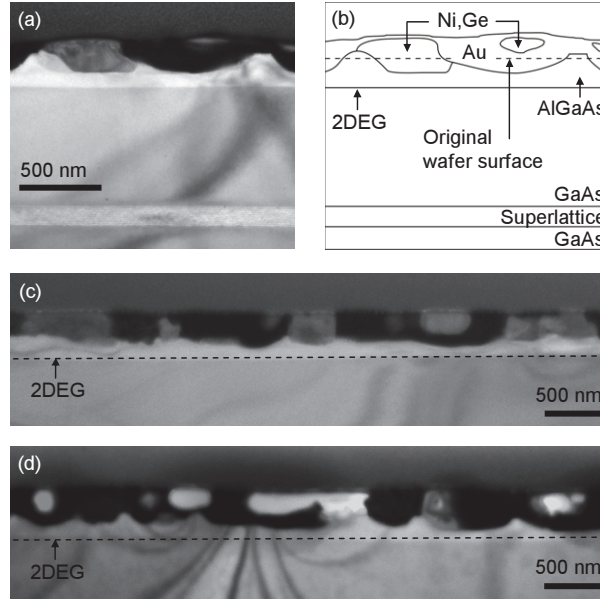


Figure 6.2: (a) Cross-section TEM image of a contact on wafer C, annealed for the optimal annealing time at 450 °C. (b) A sketch of the TEM image in (a) to specify the various layers and phases. (c) Larger area TEM image of the same contact as in (a) showing large Au-rich (black) and Ni-rich grains (dark gray) contacting the $\text{Al}_x\text{Ga}_{1-x}\text{As}$. (d) Similar image for a highly over annealed contact. The Au and Ni grains still do not penetrate the 2DEG, but Au has diffused underneath the Ni grains, which results in an increased contact resistance.

wafer surface is covered with neighboring Au and Ni_xGe [34] grains. There is evidence that for thin metallization layers (~ 100 nm) this process already occurs well below the bulk melting temperature (363 °C) of the eutectic AuGe phase [16].

Next, at higher temperatures, both the Au-rich and Ni-rich grains penetrate into the heterostructure by solid phase inter diffusion, compensated by a back flow of As and Ga. Our EDX results confirm that Ga mainly flows into Au, and As mainly into Ni-rich grains. This concerns the formation of new material phases. In several earlier studies [9, 19, 12, 14, 16, 17, 18] these phases have been identified as AuGa alloys and phases close to Ni_2GeAs . These phases penetrate only tens of nm below the original wafer surface for typical annealing conditions [9, 14].

At the same time, there is diffusion of *atomic* Ge, Ni and Au (at similar concentrations) into the heterostructure, which penetrates deeper [8, 19, 20, 15,

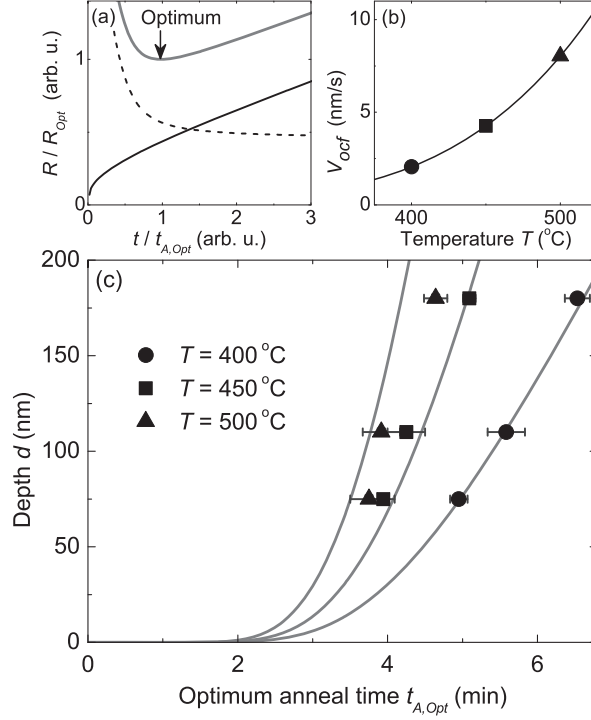


Figure 6.3: (a) Model for the resistance of an ohmic contact as a function of annealing time at constant temperature. The resistance R_{Ge} of the $\text{Al}_x\text{Ga}_{1-x}\text{As}$ layers (dashed line) decreases in time due to increased Ge doping. The interface resistance R_{if} between the surface metallization and the Ge-doped $\text{Al}_x\text{Ga}_{1-x}\text{As}$ layers (solid black line) increases in time due to a decreasing Ni-grain- $\text{Al}_x\text{Ga}_{1-x}\text{As}$ interface area. The time where the sum of these two resistances (gray solid line) shows a minimum defines the optimum annealing time $t_{A,Opt}$. (b) Effective velocity of optimal contact formation v_{ocf} as a function of temperature (Eq. 6.6), plotted for parameters that give the best fit in (c). (c) Optimal annealing times as the 2DEG depth and annealing temperature is varied (same experimental data as in Fig. 6.1c). The solid gray lines (left to right for 500, 450 and 400 °C) represent fits using the model of Eqs. 6.5 and 6.6 (see text for details).

27]. In particular, Ge diffuses out of the Ni-rich grains into the $\text{Al}_x\text{Ga}_{1-x}\text{As}$ layers, and a good ohmic contact is formed when the $\text{Al}_x\text{Ga}_{1-x}\text{As}$ layers are sufficiently doped with Ge all the way up to the 2DEG. While this is progressing, the Au-rich grains start to expand underneath the Ni-rich grains [9, 18], which have the lowest contact resistance with the doped $\text{Al}_x\text{Ga}_{1-x}\text{As}$ layer since they were the dominant supplier of Ge. The expansion of the AuGa grains is possibly due to the relatively low activation energy for out diffusion of Ga into Au [33] (while

the Al-As binding energy is relatively high [19]). This latter process increases the interface resistance between the metallization on the surface and the doped $\text{Al}_x\text{Ga}_{1-x}\text{As}$ layer. Thus, the formation of an optimal contact is a competition between these two processes.

The in-diffusion of Ge lowers the contact resistance for two reasons. 1) The full $\text{Al}_x\text{Ga}_{1-x}\text{As}$ region between the surface and the 2DEG becomes a highly doped region with a reasonably low bulk resistivity. 2) The Ge doping in this region makes the Schottky barrier between the doped semiconductor and the surface metallization very thin (the barrier height is probably not changing significantly [35]), up to the point where its series contribution to the contact resistance is small. The total contact resistance is then dominated by doped $\text{Al}_x\text{Ga}_{1-x}\text{As}$ region, giving linear transport characteristics (a similar effect occurs for contacts to n-GaAs due to spreading resistance below the contact [6]).

As said, it is not yet well established which processes are responsible for the resistance increase upon over annealing. The fact that over annealing with 2DEG samples and n-GaAs samples [9] occurs qualitatively in a very similar manner (and also at similar annealing times and temperatures) is a first indication that it is due to a process near the interface with metal-rich phases on the surface, rather than a process at the depth of the 2DEG or the edge of a contact. Further, our results now show that the resistance increase for 2DEG samples is also correlated with the expanding AuGa grains below the Ni-rich grains. Various authors have suggested that the increasing contact resistance that is associated with over annealing may be due to a large number of vacancies just below the metal-rich phases near the surface [19, 14, 24] (but others suggested it was due to excessive in-diffusion of Ni [5, 14]). These mainly result from out-diffusion of Ga into the Au-rich grains (which indeed results in a very stable AuGa phase near the original wafer surface [5, 16, 17]). These vacancies occur in particular when there is no (longer) Ge diffusion into these vacancies. One should note, however, that with n-GaAs an increasing contact resistance was also observed without an expansion of the AuGa grains below the Ni-rich grains [14], but this does not rule out that an increasing number of vacancies is responsible for over annealing.

Finally we remark that both the Ni-rich and Au-rich grains are probably important for rapid annealing at relatively low temperatures. The Ni-rich grains act as the supplier of Ge. The presence of Au grains may be important since it rapidly results in a large number of Ga vacancies. This probably enhances the in-diffusion of Ge. It was for example also observed that the creation of such vacancies near the surface, enhances the diffusion of Si dopants from the doping

layer (much deeper into the material) into neighboring layers [15].

6.6 Diffusion model

We use the above description to construct a model that predicts the optimal annealing time for a given annealing temperature and 2DEG depth d . The contact resistance is then the series resistance of the resistance of the Ge-doped $\text{Al}_x\text{Ga}_{1-x}\text{As}$ region (R_{Ge}) and the interface resistance between the surface metallization and this Ge-doped $\text{Al}_x\text{Ga}_{1-x}\text{As}$ layer (R_{if}). For both we consider the average over the full contact area. We will first assume an anneal temperature T that is constant in time. We model the resistance of the Ge-doped $\text{Al}_x\text{Ga}_{1-x}\text{As}$ region using the result from work on n-GaAs that the contact resistance is inversely proportional to the doping concentration [6]. Thus, we assume that

$$R_{Ge} \propto \int \frac{1}{C(z)/C_0} dz, \quad (6.3)$$

where $C(z)/C_0$ is the local Ge concentration at depth z as in Eq. 6.1, and where the integral runs from the depth of the Au and Ni grains to the depth of the 2DEG. The behavior of this equation is that R_{Ge} first rapidly decreases, and then curves off to saturate at a level that is proportional to d (dashed curve in Fig. 6.3a).

To model R_{if} , we assume that the increase in resistance for over annealed contacts is related to the decrease in Ni-grain- $\text{Al}_x\text{Ga}_{1-x}\text{As}$ interface area. Imagine, for simplicity, a single, square shaped Ni-rich grain with area $A_{Ni} = L_{Ni}^2$. We model the reduction of this area as a sideways diffusion process of Au, again with a time-dependence as simple diffusion analogues to Eq. 6.1. The length of a side is then reduced as $L_{Ni}(t) \approx L_0 - 2\sqrt{4D_{Au}t}$, where L_0 is the initial grain size, and D_{Au} the diffusion constant for this process, such that

$$R_{if} \propto \frac{1}{(L_0 - 2\sqrt{4D_{Au}t})^2}. \quad (6.4)$$

For a very wide parameter range, this model gives that R_{if} increases more or less linearly in time (solid black curve in Fig. 6.3a). A resistance increase that is much stronger than linear only sets in when the total interface area approaches zero, when the contact is already strongly over annealed. The total contact resistance is the sum of R_{Ge} and R_{if} (gray solid curve Fig. 6.3a), and the optimal annealing time is then defined as the time where this sum shows a minimum value.

We can reduce the number of fitting parameters for this modeling to only two with the following approach. For R_{Ge} in Eq. 6.3, we assume parameters where R_{Ge} saturates at a value below, but on the order of the optimal contact resistance R_{opt} . We also assume that this saturation occurs in a time scale on the order of a few times the optimal annealing time. For R_{if} in Eq. 6.4, we assume that it has a value below R_{opt} for $t = 0$, and that it increases more or less in a linear fashion to a value of order R_{opt} . This increase should take place in a time scale on the order of the optimal annealing time. Numerically investigating this model then shows that it has for a very wide parameter range the behavior that the increase of optimal annealing time $t_{A,Opt}$ with increasing 2DEG depth d is close to linear. We can express this using an effective velocity for optimal contact formation v_{ocf} ,

$$t_{A,Opt} = d/v_{ocf}. \quad (6.5)$$

Furthermore, numerical investigation of the temperature dependence shows that v_{ocf} behaves according to

$$v_{ocf}(T) = v_0 \exp\left(-\frac{E_a}{k_B T}\right) \quad (6.6)$$

when the diffusion processes that underlie Eq. 6.3 and Eq. 6.4 are both thermally activated with a similar activation energy E_a . We can now fit this model to our experimental data only using Eq. 6.5 and Eq. 6.6, such that we only have v_0 and E_a as fitting parameters. In doing so, we take again into account that the temperature $T(t)$ is not constant during annealing, and use again profiles as in Fig 6.1a.

The results of this fitting are presented in Fig. 6.3c, and v_{ocf} as a function of temperature for these fitting parameters ($E_a = 0.6$ eV and $v_0 = 7.6 \cdot 10^{-5}$ m/s) is plotted in Fig. 6.3b. While it is a crude model, the fits are very reasonable, showing that the model is useful for predicting optimal annealing times. Furthermore, the value for E_a is a realistic number [31, 32, 33]. Our model also predicts that the minimum value of the resistance that can be achieved for optimally annealed contacts increases with increasing 2DEG depth. We did not observe such a clear trend, probably because the resistance of optimal contacts is so low that one needs to include contributions from 2DEG square resistance around and underneath the contact when evaluating absolute values (further discussed below).

6.7 Contact-shape dependence

Our model for the annealing mechanism implies that optimal contacts have a rather uniform Ge concentration throughout the $\text{Al}_x\text{Ga}_{1-x}\text{As}$ layers, and that this results in a value for R_{Ge} of order $10\ \Omega$. This implies that the bulk resistivity in the doped Ge-doped $\text{Al}_x\text{Ga}_{1-x}\text{As}$ layer is around $4\ \Omega\text{m}$. In turn, this implies that in-plane electron transport under an optimal contact from the metallization on the surface to 2DEG on the side of the contact still mainly takes place in the original 2DEG layer. If the square resistance R_\square for transport in the original 2DEG layer below the contact does not strongly increase during annealing, and if it is smaller than the contact resistance, this also implies that the resistance of optimal contacts should be inversely proportional to the contact area. Thus, measuring whether the contact resistance depends on contact area or on the circumference of a contact can give further insight in the annealing mechanism and contact properties.

We carried out such a study, by varying the shape of contacts. All results that we discussed up to here were obtained with square contacts with an area A of $0.04\ \text{mm}^2$ and a circumference $C_L = 4L$ of $0.8\ \text{mm}$ (on the side of a Hall bar). For the dependence on contact shape, we measured various sets where we varied the circumference C_L while keeping the area constant at $0.04\ \text{mm}^2$, and various sets where we varied the area while keeping the circumference constant at $0.8\ \text{mm}$. We varied the shape from smooth circular shape to square shapes with a zig-zag edge at the $50\ \mu\text{m}$ scale, to avoid getting too much resistance contribution from square resistance of 2DEG right next to a contact (for these devices we used electron-beam lithography). The study only used wafer A. All contacts were fabricated and annealed in one single batch to ensure that it is meaningful to compare the values of contact resistance.

For this study, we inject again current into the contact that is measured, and extract the current using another contact. However, the dependence on contact shape can only give an unambiguous result if the resistance from each side of the studied contact to the place in the 2DEG where the current is extracted is sufficiently similar. This can be achieved by making the distance between the contacts larger than the size of the contacts. Thus, we now fabricated contacts in the middle of $2\ \text{mm}$ by $3\ \text{mm}$ cleaved wafer pieces (two rows of four contacts, with center-to-center distance between rows $1\ \text{mm}$, and center-to-center distance between contacts within a row $0.6\ \text{mm}$). Using four different contacts for a 4-terminal measurement on the 2DEG (with the current biased from one row to

the other) gives on these samples indeed low values around 8Ω , in reasonable agreement with the value of the 2DEG square resistance R_{\square} of about 20Ω . Contact resistance values were again determined in a current-biased 4-terminal configuration, with two terminals connected to the bond wire on the contact, the second current terminal on the opposite contact in the other row, and the second voltage terminal on a neighboring contact in the same row.

On contacts that are not annealed, we can observe a tunnel current, as expected for Schottky barriers. Here, the effective resistance is inversely proportional to area. For optimally annealed contacts, we found that the contact resistance was independent on circumference, while only showing a weak dependence on area (weaker than inversely proportional to area), see Fig. 6.4. The fact that the dependence on shape does here not show a clear dependence as $\langle R \rangle \propto 1/A$ agrees with the fact that the $\langle R \rangle$ values are comparable to the square resistance of the 2DEG, such that the latter gives a significant contribution to the total contact resistance. Fully understanding the contact resistance then requires incorporating all square resistance contributions from underneath and around the 2DEG. Since we found it impossible to estimate these effects with a small error bar, we tried to demonstrate a clear dependence on area by measuring slightly under annealed contacts instead.

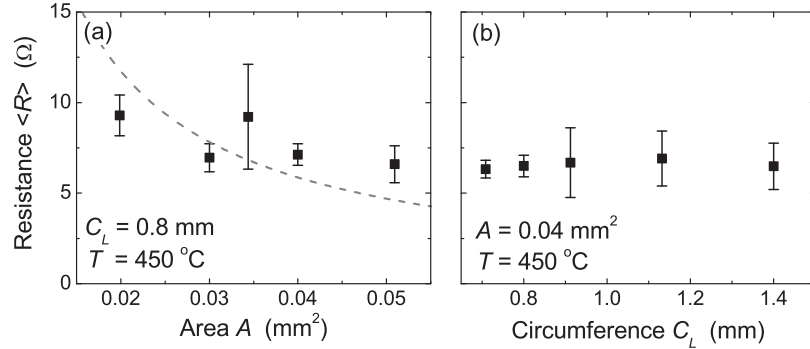


Figure 6.4: Contact resistance $\langle R \rangle$ as a function of (a) contact area A for constant circumference $4L$ and (b) contact circumference C for constant area A . The error bars here represent the standard deviation from measuring R on 8 identical contacts. The dashed line in (a) is a fit using $\langle R \rangle \propto 1/A$.

On two sets of under annealed contacts on wafer A, where we used shorter anneal times than $t_{A,Opt}$ (average contact resistance of 30Ω and 500Ω), we found (within error bar) no dependence on area or circumference. We can only explain this result if we assume that the 2DEG square resistance underneath

the contact is significantly increased (to values comparable to the total observed contact resistance) for under annealed contacts. This probably results from the in-diffusing Ge (and atomic Au and Ni [15, 27]), which already introduces strain and scatter centers in the 2DEG layer before optimal contact conditions are reached. For optimal annealed contacts (here with total resistance of typically $7\ \Omega$, independent of circumference), the square resistance underneath a contact must have returned to a low value of order $10\ \Omega$. Apparently, the resistance increase due to strain and scatter centers is compensated by increased Ge doping near the 2DEG layer.

The summary of this study is that the resistance of annealed contacts never shows in a clear dependence on circumference, and only a weak dependence on area for optimal contacts. We can, nevertheless, draw the following conclusions. For an optimal ohmic contact, it is *not* the case that electron transport between the surface metallization and the surrounding 2DEG mainly occurs at the edge of a contact. Instead, the full contact area plays a role, and in-plane electron transport under an optimal contact mainly takes place in the original plane of the 2DEG. In addition, we find it impossible to evaluate the absolute values of the contact resistance of our devices with an accuracy within a factor 2, since the resistance of an optimal contact has a contribution from the square resistance underneath the contact, and its value is influenced by the annealing process. Further, future studies in this direction should consider that pressing the bond wire (with a footprint of about $100\times 100\ \mu\text{m}^2$) onto the surface metallization may locally disturb the contact properties, which can disturb a clear dependence on contact shape.

We could therefore not study the property of our model that the optimal contact resistance value should be proportional to d . Instead, we should evaluate whether the enhanced square resistance underneath a contact needs to be incorporated in our model. We find that this is not needed for the following reasons: for over annealing it does not play a role, since we observe the same over-annealing mechanism as observed on bulk n-GaAs. Optimally annealed contacts occur when the square resistance underneath the contacts has again low values of order $10\ \Omega$. Here we observe a weak area dependence and no dependence on circumference, such that we can rule out that the effect dominates the contact resistance. Thus, the only effect is that it temporarily enhances the total contact resistance by about a factor 2 while the annealing progresses towards optimal contact conditions. Note that this does not change the fact that lowering the contact resistance in this phase still fully depends on further Ge diffusion towards the 2DEG layer.

Therefore, it only slightly modifies how R_{Ge} in Eq. 6.3 decreases towards low values.

6.8 Conclusions

Summarizing, we have measured the zero-bias resistance of annealed AuGe/Ni/Au ohmic contacts to a 2DEG as a function of annealing time and temperature. We have thus obtained optimal annealing parameters for three different heterostructures where the 2DEG lies at a different depth below the wafer surface. TEM images of several annealed contacts provided further insight into the annealing mechanism and the formation of a good ohmic contact.

Combining this information we have developed a model that can predict the optimal annealing parameters for contacting a 2DEG at a certain depth in a GaAs/Al_xGa_{1-x}As heterostructure. The model assumes two competing processes: 1) Diffusion of Ge into the heterostructure lowers the contact resistance, and results in linear transport characteristics. 2) At longer annealing times, Au-rich phases diffuse in between the heterostructure and Ni-rich phases at the wafer surface. The associated increase in contact resistance is probably due to subsequent diffusion of Ga into this Au-rich phase, since this increases the number of Ga vacancies in the heterostructure near the metallization on the surface. The competition between these two processes results in a mechanism where the optimal annealing time (for a process at constant annealing temperature) is proportional to the depth of the 2DEG below the surface, and the speed of this process has thermally activated behavior. This model should have predictive power for many heterostructures, as long as the temperature of the samples as a function of time during the annealing process is known. Our study of how the contact resistance depends on the shape of the contact confirmed that the full contact area plays a role in electron transport between the metallization on the surface and the 2DEG.

Our model may become invalid for systems with a very deep 2DEG, since R_{if} (Eq. 6.4) is expected to increase more rapidly at long annealing times, possibly resulting in non-ohmic behavior. Our results suggests that for solving this problem the focus should be at maintaining sufficient contact area between Ge-rich Ni grains and the Ge-doped Al_xGa_{1-x}As layer at long annealing times. This can possibly be engineered by changing the layer thickness, order and composition of the initial AuGe/Ni/Au metallization [19, 12, 14, 15, 16, 21, 26], or by including a Pt, Nb or Ag layer below the top Au layer that suppresses the intermixing of

this Au with layers at the wafer surface[7, 19, 15, 22, 24] (uniform Ni/Ge/As layers been reported [21]). Alternatively, one can reduce the depth of the 2DEG by etching before deposition of AuGe/Ni/Au (up to the point where this results in depletion of the 2DEG).

Acknowledgements

We thank B. H. J. Wolfs, M. Sladkov and S. J. van der Molen for help and valuable discussions. Further, we acknowledge the Dutch Foundation for Fundamental Research on Matter (FOM), the Netherlands Organization for Scientific Research (NWO), and the German programs DFG-SFB 491 and BMBF-nanoQUIT for funding.

Bibliography

- [1] See for example: C. W. J. Beenakker and H. van Houten, Solid State Physics **44**, 1 (1991).
- [2] See for example: L. L. Sohn, L.P. Kouwenhoven, and G. Schön, eds., *Mesoscopic Electron Transport*, NATO ASI Series E **345** (Kluwer, Dordrecht, Netherlands, 1997).
- [3] For a review see: A. G. Baca, F. Ren, J. C. Zolper, R. D. Briggs, and S. J. Pearton, Thin Solid Films **308-309**, 599 (1997).
- [4] N. Braslau, J. B. Gunn, and J. L. Staples, Solid-State Electron. **10**, 381 (1967).
- [5] M. Ogawa, J. Appl. Phys. **51**, 406 (1980).
- [6] N. Braslau, J. Vac. Sci. Technol. **19**, 803 (1981).
- [7] C. P. Lee, B. M. Welch, and J. L. Tandon, Appl. Phys. Lett. **39** 556 (1981).
- [8] M. Heiblum, M. I. Nathan, and C. A. Chang, Solid-State Electron. **25**, 185 (1982).
- [9] T. S. Kuan, P. E. Batson, T. N. Jackson, H. Rupprecht, and E. L. Wilkie, J. Appl. Phys. **54**, 6952 (1983).
- [10] N. Braslau, Thin Solid Films **104**, 391 (1983).
- [11] N. Braslau, J. Vac. Sci. Technol. A **4**, 3085 (1986).

- [12] M. Procop, B. Sandow, H. Raidt, and L. D. Son, *Phys. Stat. Sol. A* **104**, 903 (1987).
- [13] J. R. Waldrop and R. W. Grant, *Appl. Phys. Lett.* **50**, 250 (1987).
- [14] R. A. Bruce and G. R. Piercy, *Solid-State Electron.* **30**, 729 (1987).
- [15] J. R. Shappirio, R. T. Lareau, R. A. Lux, J. J. Finnegan, D. D. Smith, L. S. Heath, and M. Taysing-Lara, *J. Vac. Sci. Technol. A* **5**, 1503 (1987).
- [16] E. Relling and A. P. Botha, *Appl. Surf. Scie.* **35**, 380 (1988).
- [17] V. G. Weizer and N. S. Fatemi, *J. Appl. Phys.* **64**, 4618 (1988).
- [18] N. E. Lumpkin, G. R. Lumpkin, and K. S. A. Butcher, *J. Mater. Res.* **11**, 1244 (1996).
- [19] P. Zwicknagl, S. D. Mukherjee, P. M. Capani, H. Lee, H. T. Griem, L. Rathbun, J. D. Berry, W. L. Jones, and L. F. Eastman, *J. Vac. Sci. Technol. B* **4** 476 (1986).
- [20] T. K. Higman, M. A. Emanuel, J. J. Coleman, S. J. Jeng, and C. M. Wayman, *J. Appl. Phys.* **60**, 677 (1986).
- [21] A. K. Rai, A. Ezis, R. J. Graham, R. Sharma, and D. W. Langer, *J. Appl. Phys.* **63**, 4723 (1988).
- [22] Y. Jin, *Solid-State Electron.* **34**, 117 (1991).
- [23] R. P. Taylor, P. T. Coleridge, M. Davies, Y. Feng, J. P. McCaffrey, and P. A. Marshall, *J. Appl. Phys.* **76**, 7966 (1994).
- [24] A. Messina, U. Meirav, and H. Shtrikman, *Thin Solid Films* **257**, 54 (1995).
- [25] R. P. Taylor, R. Newbury, A. S. Sachrajda, Y. Feng, P. T. Coleridge, M. Davies, and J. P. McCaffrey, *Superl. Microstr.* **24**, 337 (1998).
- [26] S. Raiser, U. Graumann, M. Fleischer, J. Schmid, S. Jauerneck, J. Weis, and D. A. Wharam, Scientific program of the 2005 German DPG meeting, abstract HL 58.67 (unpublished); <http://www.dpg-tagungen.de/archive/>.
- [27] G. Sai Saravanan, K. Mahadeva Bhat, K. Muraleedharan, H. P. Vyas, R. Muralidharan, and A. P. Pathak, *Semicond. Sci. Technol.* **23**, 025019 (2008).
- [28] The work that we cite in the introduction shows that the lowest values for contact resistance to n-GaAs and 2DEG systems with only a thin (few nm) buffer layer (undoped $\text{Al}_x\text{Ga}_{1-x}\text{As}$ between doping and the 2DEG) are of order $0.1 \Omega\text{mm}$, giving 0.5Ω for 0.2 mm wide contacts. However, 2DEG systems with the thickness of the buffer layer in the range of 35 nm typically

give values that are an order of magnitude higher [22]. Note that values are often reported in units Ωmm , which is not representing the bulk resistivity between surface metallization and 2DEG, but representing the contact resistance normalized to contact width, as derived with the TLM method [29, 30].

- [29] H. H. Berger, Solid-State Electron. **15**, 145 (1972).
- [30] G. K. Reeves and H. B. Harrison, IEEE Electron Device Lett. **3**, 111 (1982).
- [31] K. Sarma, R. Dalby, K. Rose, O. Aina, W. Katz, and N. Lewis, J. Appl. Phys. **56**, 2703 (1984).
- [32] A. K. Kulkarni and C. Lai, J. Vac. Sci. Technol. A **6**, 1531 (1988).
- [33] A. K. Kulkarni and C. Lai, Thin Solid Films **164**, 435 (1988).
- [34] Early in the annealing process, the grains mainly containing Ni and Ge have been identified as NiGe, Ni₂Ge and Ni₃Ge phases [9, 12].
- [35] It is believed that the height of the Schottky barrier is under all relevant conditions pinned at about 0.8 eV [11]. A lowering of the Schottky barrier with Au, Ni and Ge layers on the wafer surface was only observed for very specific interfaces [13], and does probably not occur during actual annealing of AuGe/Ni/Au contacts [12].

Chapter 7

Robust recipe for low-resistance ohmic contacts to a two-dimensional electron gas in a GaAs/AlGaAs heterostructure

Abstract

The objective of the work presented in this chapter is to measure the various resistance contributions for ohmic contacts, in order to better understand the annealing mechanism of ohmic contacts. In the previous chapter the contact resistance was measured as a function of area and circumference to investigate whether mainly the edges or the entire contact area determines the contact resistance. Only a weak area dependence was found and lack of knowledge about the values of the 2DEG resistance under the contacts prohibited drawing conclusions. Here we report on designing and measuring a dedicated device for unraveling the various resistance contributions, which include pristine 2DEG series resistance, the 2DEG resistance under a contact, the contact resistance itself, and the influence of pressing a bonding wire onto a contact.

This chapter is based on Ref. 5 on p. 159.

7.1 Introduction

In the previous chapter we studied the annealing mechanism for ohmic contacts to a two-dimensional electron gas in various GaAs/Al_xGa_{1-x}As heterostructures. That study left a few question unanswered, in part because of lack of information on whether the 2DEG resistance under an ohmic contact differs from the pristine 2DEG value, and whether pressing a bonding wire on a contact influences the resistance as it can possibly damage the ohmic contact layer over a significant area. To study these questions, we designed a dedicated device structure that allowed us to measure the contact resistance values and contributions with different measurement methods (3-point measurement, 4-point measurement and the Transmission Line Method (TLM) [1, 2]). We used and compared the results for better understanding the annealing mechanism of ohmic contacts. For a general introduction on ohmic contacts we refer to the introduction of *Chapter 6* and references therein.

All the results presented in this chapter are from samples annealed in a rapid thermal annealer (RTA), unlike the work of the previous chapter where the hot gas flow in a glass-tube furnace was used for heating the samples. In the present study we focused on changes in the mentioned contact resistance contributions as a function of annealing time (at fixed annealing temperature and depth of the 2DEG). However, the contact resistance values that we found were for all samples so low that we could not obtain sufficient measurement accuracy for determining a dependence on annealing time for the resistance of 2DEG under an ohmic contact. Instead, the value of these results is that we found a very robust recipe for low contact resistance values, with values that do not change significantly for annealing times between 20 and 350 sec. This kind of robust recipe is useful for annealing contacts on 2DEG materials with different 2DEG depths where one would need a large margin for suitable annealing times. These new results also show that the details of how the sample is heated have a strong influence on the annealing mechanism.

7.2 Experimental details

The core of our study focusses on devices that were fabricated with a GaAs/Al_{0.27}Ga_{0.73}As heterostructure with a 2DEG at 60 nm below the surface. The layer sequence of the heterostructure is as follows (top to bottom): a 5 nm *n*-GaAs cap layer, a 40 nm Al_{0.27}Ga_{0.73}As *n*-doped with Si at $2.0 \times 10^{18} \text{ cm}^{-3}$, a 15 nm intrinsic

$\text{Al}_{0.27}\text{Ga}_{0.73}\text{As}$ spacer layer, and a 800 nm GaAs layer. The 2DEG is located at the interface of the AlGaAs spacer layer and the next GaAs layer. The 2DEG density and mobility at 4.2 K were $n_{2D} = 3.30 \times 10^{15} \text{ m}^{-2}$ and $\mu_{2D} = 19.8 \text{ m}^2/\text{Vs}$, respectively. All the measurements were performed in a liquid helium vessel at 4.2 K. We also fabricated and measured devices in an identical manner from a wafer with the 2DEG at 180 nm depth (wafer WREUT12570 in Appendix A). The study on these devices was less extensive but we will mention the results that are relevant.

The size of the ohmic contact was 200 by 200 μm^2 and they were patterned with electron-beam lithography. For the ohmic contacts, layers of AuGe in eutectic-composition (12 wt% Ge, 150 nm), Ni (30 nm) and Au (20 nm) were deposited subsequently by electron-beam evaporation. The contacts were annealed at 450 °C in the rapid thermal annealer (RTA, model Jipelec Jet 150) for various times. Annealing took place in a clean N_2 flow (600 sccm) to avoid oxidation and material vapors adhering back onto the sample. During annealing the functional sample surface was directly facing the RTA heating lamps.

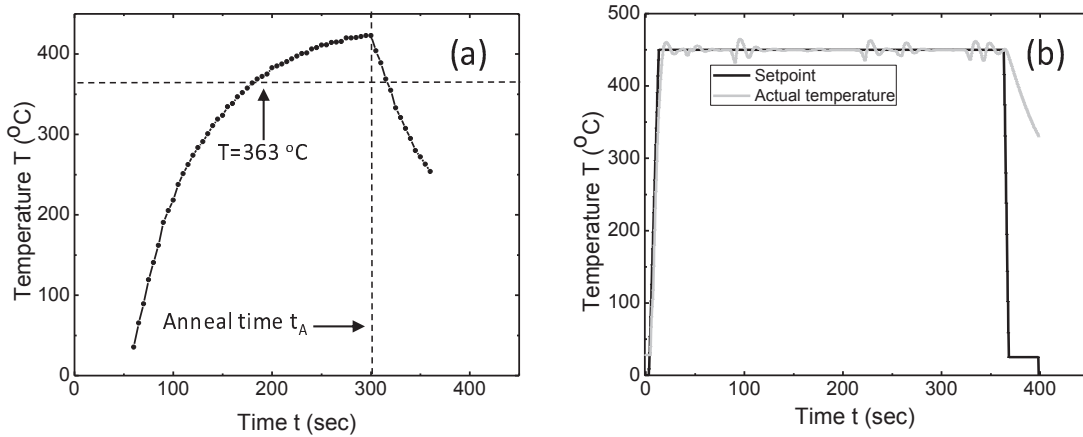


Figure 7.1: Temperature of a thermocouple in close contact with the sample as a function of time during the annealing process in the glass-tube furnace (a) and rapid thermal annealer (RTA) (b).

The annealing temperature profiles for the glass-tube oven (used for the work of *Chapter 6*) and the RTA are shown in Figs. 7.1a,b. For the glass-tube oven, the sample is brought into a pre-heated oven and the temperature rise of the sample holder to the AuGe-eutectic temperature (363°C) takes a few minutes (not easily controllable). For the RTA, on the other hand, the temperature ramp rate can be controlled and the time for reaching the set temperature was set at the much

shorter (but for RTA heating typical) value of 5 sec. This is started with the sample already in the oven. The black and light gray lines in Fig. 7.1b are for the set temperature and the actual temperature as measured by the thermocouple attached to the surface where sample is placed for annealing. All the results discussed in this chapter are for samples annealed in the RTA.

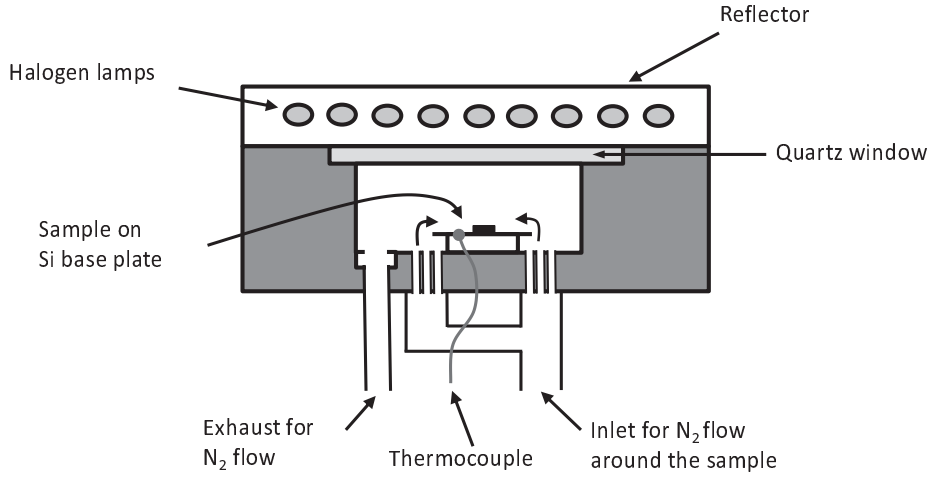


Figure 7.2: Simplified scheme of the RTA annealing chamber.

Fig. 7.2 shows a schematic of the RTA annealing chamber. The heating sources are the halogen lamps that transmit radiation through a quartz window above the sample surface. The sample is placed on a Si base plate and a thermocouple is attached to this plate for measuring the annealing temperature during the process. The flow of N_2 gas is maintained during the entire annealing process and cool down.

7.3 Device design, measurement schemes and methods

We designed a dedicated device structure for being able to study the different contact-resistance contributions with different measurement methods. An optical image of a fabricated device is shown in Fig. 7.3. A $200\ \mu\text{m}$ wide 2DEG channel is defined (U-shaped) by wet etching such that a homogeneous current flow can be applied through the defined strip. Different parts of the devices are labeled. The ohmic contacts are realized on top of the channel as well as on the sides of the channel. The available distances L_i (defined as in Fig. 7.5a) between the contacts on top of the channel are 40, 260, 460, 660, and $860\ \mu\text{m}$. The effect of annealing

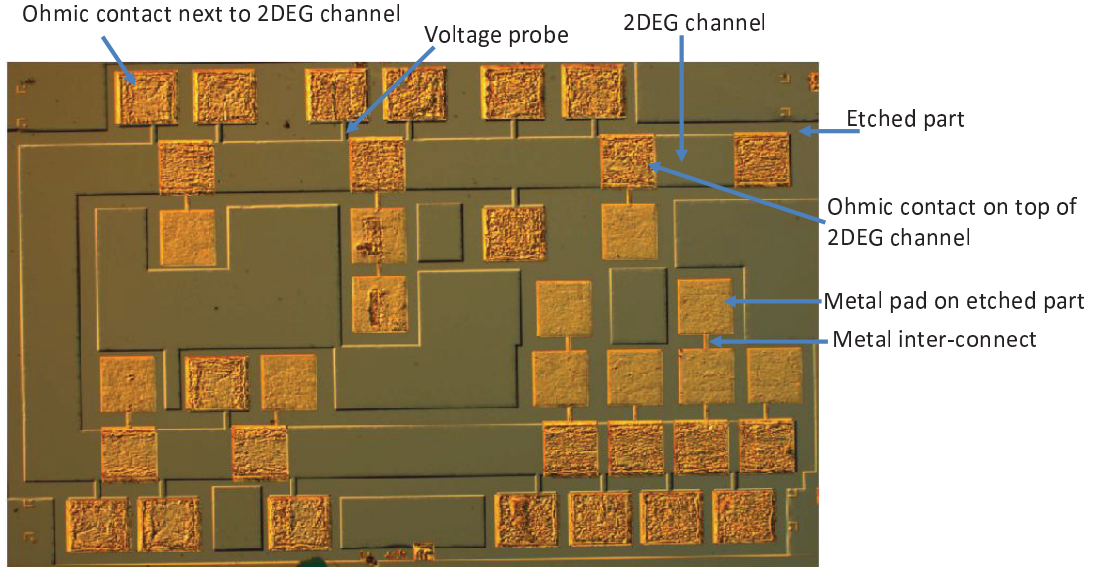


Figure 7.3: Optical microscope image of a device showing etched mesa regions and deposited contacts. The shallow part of the mesa is wet-etched at places where the design requires a boundary to a 2DEG region. The ohmic contacts and metal pads (all $200 \text{ by } 200 \mu\text{m}^2$) are deposited and annealed on 2DEG and etched surface respectively so that the latter are separated from the 2DEG.

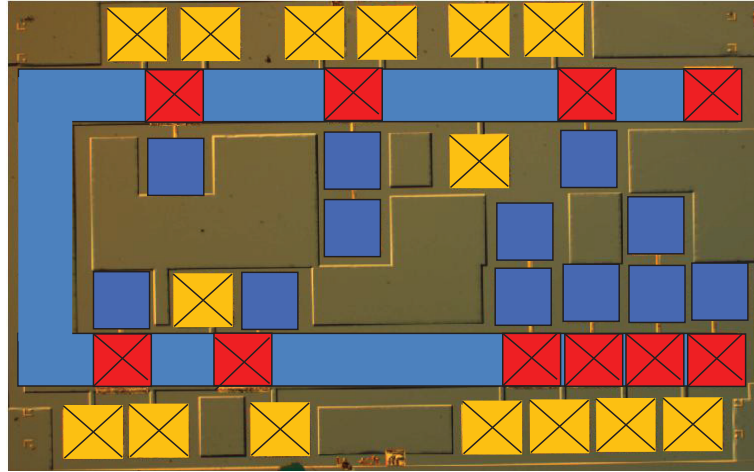


Figure 7.4: Color scheme to highlight different parts of the device. The U-shaped blue part is a $200 \mu\text{m}$ wide 2DEG channel. The red squares are ohmic contacts on top of the main 2DEG channel and the yellow squares are ohmic contacts on the side of the channel that only serve as voltage probes. The dark blue squares are metal contact pads on etched wafer areas (all contacts are $200 \text{ by } 200 \mu\text{m}^2$).

times on the pristine 2DEG resistance, and on the full contact resistance and 2DEG resistance under ohmic contacts are determined for the ohmic contacts deposited on top of the 2DEG channel. The ohmic contacts deposited on the sides are connected to the 2DEG channel via narrow 2DEG strips (20 μm wide) and serve as voltage probes (used when measuring the resistance of the contacts, the resistance of pristine 2DEG and the resistance of 2DEG under contacts). Metal pads and metal inter-connects between pads are deposited on etched parts of the device. These metal pads are connected to the ohmic contacts via metal inter-connects and used for measuring the ohmic contact resistances without directly bonding on the ohmic contacts themselves (the resistance contributions from metal pads and inter-connects are subtracted in this case). By comparing values measured with this bonding scheme to a subsequent measurement with bonding directly on top of the ohmic contacts, the influence of pressing a bonding wire on an ohmic contact can be determined. The color scheme in Fig. 7.4 further illustrates the various device parts more clearly. The long 2DEG channel is shown with a light blue color. The ohmic contacts are shown as crossed color squares, with contacts on top of the 2DEG channel in red and side contacts in yellow. The metal pads on etched regions are shown as dark blue squares.

Fig. 7.5 and Fig. 7.6 show the various measurement schemes that we applied in this study. We first explain the Transmission Line Method (TLM) before explaining the other measurement schemes. The TLM method [1, 2] is a very accurate method for measuring the values of pristine 2DEG square resistance and ohmic-contact resistance, and is widely used in research on ohmic contacts. Fig. 7.5 shows how the TLM method works. The contacts are made on a 2DEG strip with an increasing distance between pairs of adjacent contacts (Fig. 7.5a). The width of the contact and channel is labeled as W . For resistance measurements a four point current-biased scheme is used (Fig. 7.5a). This measurement is carried out for all the consecutive contact pairs. Fig. 7.5b shows a schematic of a side view on one of the contacts and the resistance contributions that play a role. The resistance contributions are R_p (probe resistance), R_{pc} (probe-to-contact resistance), R_c (actual contact resistance between probe and 2DEG) and R_{ch} (2DEG resistance of the channel between the contacts). Fig. 7.5c shows the corresponding circuit diagram for the complete four-probe scheme. Since the probe (R_p) and the probe-to-contact resistances (R_{pc}) are negligible as compared to the input resistance of the voltmeter they can be neglected. The total resistance measured between pairs of consecutive contacts is then

$$R_{total} = 2R_c + R_{ch} = V/I, \quad (7.1)$$

The plot in Fig. 7.5d illustrates how to extract the contact and 2DEG square resistance values from the TLM data. The R_{total} values are plotted as a function of the channel length. The resistance contribution R_{ch} increases linearly with increasing channel length and R_{total} shows a linear dependence with an offset from zero that is equal to $2R_c$. A linear fit to the data points can thus be used to obtain R_c . In addition, the slope of the R_{total} provides an accurate measure for the square resistance R_{\square} of pristine 2DEG (2DEG between contacts). Using that $R_{ch} = R_{\square}L_i/W$ this can be expressed as $R_{\square} = R_cW/L_T$, where the transfer length L_T is defined using the intercept at zero resistance for the linear trend (see Fig. 7.5d). Our experiment indeed only gave results with a linear dependence of R_{total} on L_i for $L_i \geq 260\mu\text{m}$ (no significant deviations). While data for $L_i = 40\mu\text{m}$ is candidate for showing deviations from the linear trend (which can give insight in the resistance distribution inside a contact), this data was discarded for the TLM analysis since it showed large fluctuations (because it is more sensitive to the exact alignment of the contact edges).

We used an extended TLM scheme with first measurements that used bonding on the metal side pads (not shown in Fig. 7.5) and subsequently measurements that used bonding directly on top of the ohmic contacts (as in Fig. 7.5) to investigate the influence of pressing a bonding wire on an ohmic contact. Columns 6 and 7 in Table 7.1 show the resistance values measured by the TLM method with bonding wires on metal side pads and ohmic contacts respectively. While TLM gives accurate results for R_c , it is not possible to use it for measuring the 2DEG resistance under an ohmic. It also does not give information on where inside a contact the contributions to contact resistance arise, while such information is required for detailed understanding of the annealing mechanism.

We now discuss other measurement schemes that we applied for determining the various resistance contributions. For a first round of measurement (this order was carried out in parallel with the TLM measurements) bonding wires are pressed on the side ohmic contacts. Two ohmic contacts on top of the 2DEG channel are used for injecting current into the channel (Fig. 7.6a,b). The voltage drop across a known length of pristine 2DEG channel or 2DEG under an ohmic contacts can then be measured with the voltage probes. The measured values R_{\square} (square resistance of pristine 2DEG, no significant deviations from the TLM values) and $R_{\square, \text{below}C}$ (square resistance of 2DEG below an ohmic contact) are shown in column 2 and 3 of the Table 7.1, respectively.

For a second round of measurements, two bonding wires are pressed onto each metal side pad that connects to the metal layer of an ohmic contact on top of the

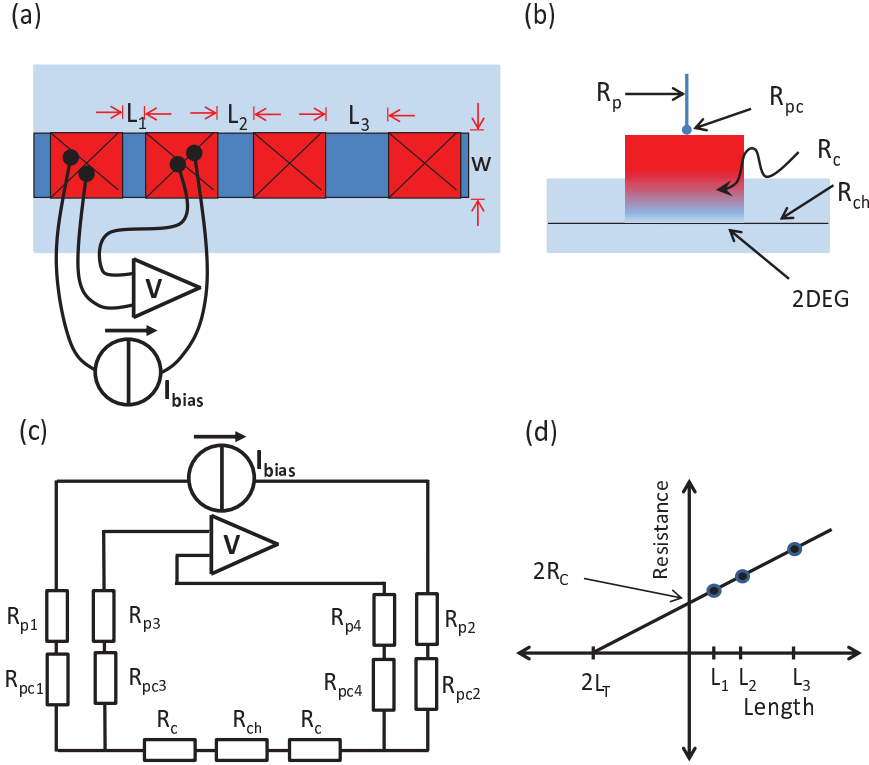


Figure 7.5: Transmission Line Method (TLM) measurement scheme. **(a)** Ohmic contacts are made over the full width of a 2DEG strip with increasing distance L_i between adjacent contacts. A 4-point measurement is used for determining the resistance R_{total} for each segment. **(b)** A side view on a contact showing the various resistance contributions (see main text for details). **(c)** A circuit diagram for the 4-point scheme with the resistance contributions from panel (b). **(d)** A schematic plot of TLM measurement results (see main text for details).

channel (Fig. 7.6c). The resistance contributions from the metal side pads and metal inter-connects (measured on each sample, typically 10Ω) are measured separately and are subtracted. This measurement scheme directly gives values for the total contact resistance of contacts, which are denoted as $R_{c,3p-pad}$ and are shown in column 4 of Table 7.1.

A third round of measurements was carried out as in Fig. 7.6d. This scheme gives directly a value for the total contact resistance of contacts with the bonding wires pressed directly on top of the contact that is measured. The results are denoted as $R_{c,3p-ohm}$ and are shown in column 5 of Table 7.1.

All the resistance values measured with various schemes are thus collected in Table 7.1 for different annealing times. The reported values are average of

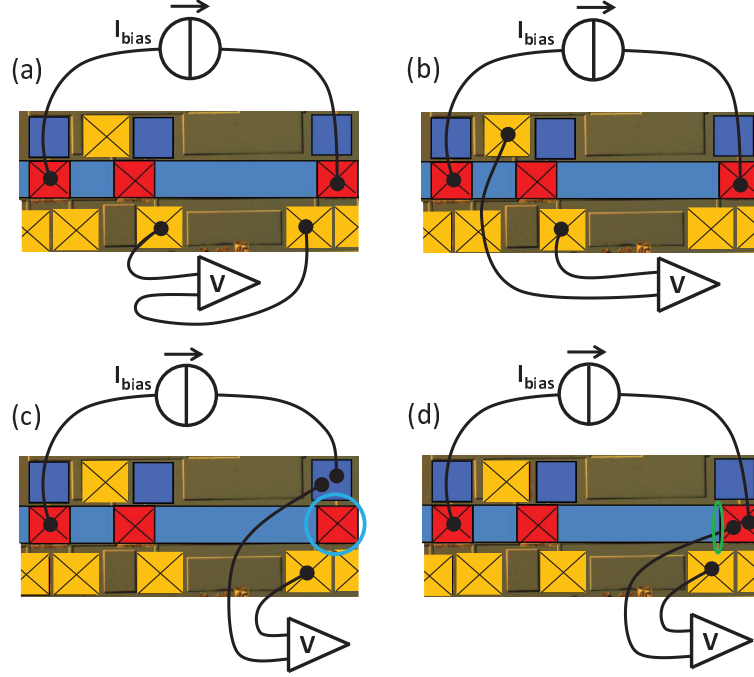


Figure 7.6: Various measurement schemes illustrated with colored contacts as in Fig. 7.4. **(a)** The scheme to measure the pristine 2DEG resistance. **(b)** The scheme to measure the 2DEG resistance under an ohmic contact. **(c)** The 3-point measurement scheme for measuring the resistance of an ohmic contact without a bonding wire directly on top of the measured contact (circled in this case). The bonding wire is here on a metal side pad that is connected to the surface metallization of the measured ohmic contact via a narrow metal inter-connect. **(d)** The 3-point measurement scheme for measuring the resistance of an ohmic contact with bonding directly on top of the measured contact.

(in most cases) 5 contacts. The reported error margins for column 2 to 5 are the standard deviations of these results. For column 6 and 7, the standard error values obtained from fitting the linear trend are shown.

7.4 Results and discussions

Table 7.1 thus lists all the measured resistance values that were introduced. We used in total 4 bonding steps on each device to perform the subsequent measurements (in part because of a limited number of measurement wires in the setup). The order of the measurements was the following: *(i)* Column 2 and 3; *(ii)* Column 6; *(iii)* Column 4; *(iv)* Column 5 and 7.

1	2	3	4	5	6	7
$t_A(sec)$	$R_{\square}(\Omega)$	$R_{\square,belowC}(\Omega)$	$R_{c,3p-pad}(\Omega)$	$R_{c,3p-ohm}(\Omega)$	$R_{c,TLM-pad}(\Omega)$	$R_{c,TLM-ohm}(\Omega)$
—	Fig. 7.6a	Fig. 7.6b	Fig. 7.6c	Fig. 7.6d	Fig. 7.5	Fig. 7.5
20	19.91 ± 1.07	2.25 ± 1.18	8.60 ± 0.75	4.49 ± 0.36	9.18 ± 4.5	0.41 ± 3.4
50	19.61 ± 1.56	3.00 ± 0.30	5.29 ± 1.19	4.00 ± 0.28	6.28 ± 2.86	1.24 ± 1.13
100	19.50 ± 0.60	3.17 ± 1.55	9.04 ± 0.62	4.47 ± 0.45	9.77 ± 0.80	2.38 ± 0.41
350	20.77 ± 0.39	3.78 ± 0.38	7.76 ± 1.02	4.44 ± 0.37	not measured	2.30 ± 0.30

Table 7.1: The different resistance values for different annealing times. Row 3 lists the figure with the corresponding measurement scheme. Column 2 and 3 are for the 2DEG square resistance and 2DEG square resistance under the contacts, respectively. Column 4 and 5 are for the contact resistance measured by the 3-point method with the bonding wires on side pads and the ohmic contacts, respectively. Column 6 and 7 report the contact resistance as determined with the TLM method, with the bonding wires on side pads and the ohmic contacts, respectively.

The 2DEG resistance under the ohmic contacts is by about a factor 6 lower than the resistance of the pristine 2DEG (columns 2 and 3). This occurs for all annealing times. A previous study on ohmic contacts by G. Sai Saravanan *et al.* [4] and our results in *Chapter 6* show that upon annealing Germanium diffuses from the surface towards 2DEG, and this increases n -doping near the 2DEG. While this can reduce the mobility in this region, the effective 2DEG square resistance apparently decrease due to the higher doping level. The resistance values are almost constant for all the annealing times that we studied (20 to 350 sec). This suggests that Ge diffuses to 2DEG region already for short annealing times and that the Ge concentration does not change significantly anymore for longer annealing times.

Columns 4 to 7 in Table 7.1 show the contact resistance values as measured with different measurement schemes. The results show significant differences, that we can partly explain and which provide some insight in the different contributions to the contact resistance. As a starting point of the discussion we use the values in column 7, which is the TLM result for directly bonding on the ohmic contacts. This is the most unambiguous number for the contact resistance. Column 5 lists the contact resistance values measured with the 3-point method with bonding directly on the ohmic contact. Column 5 has values that are typically 3 Ω higher than the values in column 7. This can be explained by the fact that the result of column 5 contains a series resistance contribution from a 30 μm wide region of pristine 2DEG (from the distance between the ohmic contact and the 2DEG voltage probe, this 2DEG part is encircled in green in Fig. 7.6d). The

expected resistance contribution of this part is indeed $\sim 3\Omega$ (using R_{\square} of column 2). This effect was also used for correcting the values of $R_{\square, below C}$ in column 3.

Column 6 shows resistance values from the TLM method with bonding on the side pad (note that 2 side pads are involved) and these results are about $2 \times 3\Omega$ higher than the values in column 7. Similarly, the results of column 4 (3-point, bonding on pad, note that only 1 side pad is involved) is about $1 \times 3\Omega$ higher than the values in column 5 (3-point, bonding on ohmic). Here we must consider two possible explanations. The first is that the act of pressing a bond wire on top of the ohmic contact results in a lowering of the effective contact resistance by about 3Ω . The second possibility is that it results from the fact that the metal side pads are only connected to the surface metal of the ohmic-contact at one narrow point. This can yield that on average the spreading resistance inside the contact gives a contribution that is about 3Ω higher for the cases with bonding on the side pads. Given that all our measurement results and the various contributions are on the scale of only a few Ω , we can not distinguish these cases (we could rule out that it was not due to series resistance inside the metal side pad and its inter-connect).

Our results do not allow for more detailed conclusions on the various contributions to the contact resistance or on the annealing mechanism. The reason is that the measured resistance values were all much lower than expected (given the earlier work of *Chapter 6*) and that the results showed, surprisingly, almost no dependence on the annealing time. In addition, the possible effects of spreading resistance and small series-resistance contributions are all on the scale of a few Ω , and these values are close to the total contact resistance values and their statistical variation. This rules out that further analysis of our present results can give sufficient accuracy for answering the questions that we aimed to study.

At the same time, it is an interesting result that we find very low contact resistance values, and that the values do almost not change when changing the annealing time by a factor 18. In addition, these contact resistance values rank among the lowest reported values [3]. Table 7.2 provides different representations of the resistance values that we obtained. These values are useful for a comparison to values in the literature where authors present values of contact resistance in various ways. When comparing the literature one also needs to account for a dependence on the depth of the 2DEG and the thickness of the buffer layer. Our results on the wafer with the 2DEG at 180 nm depth (instead of 60 nm) show indeed slightly higher values, with for $R_{c, 3p-pad} \approx 15\Omega$. Also these samples

showed almost no dependence on annealing time (similar results for 30 sec and 550 sec).

We have at this stage little insight why the fabrication method that we used gives such low contact resistance values, while also being very robust against a variation in annealing time. We have some initial results that point out that the variation of annealing profile of the temperature as a function of time is important. For the experiments on the samples with the 2DEG at 180 nm depth we compared results of annealing for 550 and 600 sec annealing times with 5 sec RTA ramp time, to results for 550 sec annealing time that started after a 120 sec RTA ramp time (similar to the glass-tube oven). The samples of the latter batch had contact resistance values that were twice as high. A second important difference with the work of *Chapter 6* is that the glass-tube oven heats the sample in a gas flow, while the RTA heats the sample by radiation. This can influence the exact way the surface metallization gets heated, and thereby have an influence on the annealing mechanism. Finally, there is possibly a role for having a suitable very clean N₂ flow during annealing, and a very clean sample surface before fabrication is started (samples that appeared dirty upon inspection did not yield good results with low contact resistance values).

1	2	3	4	5
t_A (sec)	$R_{c,TLM-ohm}(\Omega)$	$R'_c (\Omega mm)$	$R_c (\Omega cm^2)$	$\rho_{bulk} (\Omega m)$
20	0.41 ± 3.4	0.082 ± 0.68	$1.64 \times 10^{-4} \pm 1.36 \times 10^{-3}$	0.27 ± 2.26
50	1.24 ± 1.13	0.248 ± 0.226	$4.96 \times 10^{-4} \pm 4.52 \times 10^{-4}$	0.83 ± 0.75
100	2.38 ± 0.41	0.476 ± 0.82	$9.52 \times 10^{-4} \pm 1.64 \times 10^{-4}$	1.59 ± 0.27
350	2.30 ± 0.30	0.46 ± 0.06	$9.2 \times 10^{-4} \pm 1.2 \times 10^{-4}$	1.53 ± 0.2

Table 7.2: The contact resistance values as measured by the TLM method (column 7 in Table 7.1) represented in various forms. Column 2 shows the measured value of the contact resistance. Columns 3, 4 and 5 show the same resistance values but converted to a value that is normalized to contact to width (column 3), a value for the specific contact resistance per contact area (column 4), and a bulk resistivity value for the material in the volume between the surface metallization and the 2DEG layer.

7.5 Conclusions

We developed a dedicated device to study and unravel the various contributions to the resistance values of an ohmic contact. We could show that the 2DEG

resistance under an ohmic contact gets lower upon annealing, and that pressing a bonding wire onto an ohmic contact either has little influence or only lowers it by a few Ω . However, we could not fully exploit the measurement possibilities of our device design because we obtained very low contact resistance values that showed no clear dependence on annealing times that were varied from 20 to 350 sec. Preliminary measurements show that these results can be obtained with rapid heating (5 sec ramp time) during annealing, and that slower ramp times cause higher contact resistance values. A comparison with the work of *Chapter 6* also suggests that heating by radiation gives lower contact resistance values than heating samples in a hot gas flow.

Bibliography

- [1] H. H. Berger, Solid-State Electron. **15**, 145 (1972).
- [2] G. K. Reeves and H. B. Harrison, IEEE Electron Device Lett. **3**, 111 (1982).
- [3] Y. Jin, Solid-State Electron. **34**, 117 (1991).
- [4] G. Sai Saravanan *et al.*, Semicond. Sci. Technol. **23**, 025019 (2008).

Appendix A

Wafer inventory

In this Appendix we present the various heterostructures used in this thesis. All values for density and mobility were measured at 4.2 K unless mentioned with samples cooled down in the dark. We present the layer structure from top down.

A.1 WSUMI301611

This wafer was purchased from Sumitomo Electric Industries, Ltd. Devices from this wafer were used for studies on ohmic contact formation to a 2DEG in Chapter 7.

- 2DEG depth: 60 nm
- Density: $4.60 \times 10^{15} \text{ m}^{-2}$ at 77 K.
- Mobility: $18.9 \text{ m}^2/\text{Vs}$ at 77 K.
- Layer structure:
 - 5 nm n -GaAs
 - 40 nm $\text{Al}_{0.27}\text{Ga}_{0.73}\text{As}$ (n-doped with Si at $2 \times 10^{18} \text{ cm}^{-3}$)
 - 15 nm $\text{Al}_{0.27}\text{Ga}_{0.73}\text{As}$
 - 800 nm GaAs

A.2 WSUMI301612

This wafer was purchased from Sumitomo Electric Industries, Ltd. Devices from this wafer were used for studies on ohmic contact formation to a 2DEG in Chapter 6.

- 2DEG depth: 75 nm
- Density: $2.78 \times 10^{15} \text{ m}^{-2}$
- Mobility: $19.5 \text{ m}^2/\text{Vs}$
- Layer structure:
 - 5 nm n -GaAs
 - 40 nm $\text{Al}_{0.27}\text{Ga}_{0.73}\text{As}$ (n-doped with Si at $2 \times 10^{18} \text{ cm}^{-3}$)
 - 30 nm $\text{Al}_{0.27}\text{Ga}_{0.73}\text{As}$
 - 800 nm GaAs

A.3 WREUT1098

This wafer was grown in the group of D. Reuter and A. D. Wieck at the Ruhr-Universität in Bochum, Germany. Devices from this wafer were used for experiments on quantum point contacts in Chapters 3, 4 and 5, and for studies on ohmic contact formation to a 2DEG in Chapter 6.

- 2DEG Depth: 114 nm
- Density: $1.5 \times 10^{15} \text{ m}^{-2}$
- Mobility: $159 \text{ m}^2/\text{Vs}$
- Layer structure:
 - 5.5 nm n -GaAs
 - 71.9 nm $\text{Al}_{0.32}\text{Ga}_{0.68}\text{As}$ (n-doped with Si at $\sim 1 \times 10^{18} \text{ cm}^{-3}$)
 - 36.8 nm $\text{Al}_{0.32}\text{Ga}_{0.68}\text{As}$
 - 933 nm GaAs

A.4 WREUT1588

This wafer was grown in the group of D. Reuter and A. D. Wieck at the Ruhr-Universität in Bochum, Germany. Devices from this wafer were used for experiments on quantum point contacts in Chapters 3, 4 and 5.

- 2DEG Depth: 110 nm
- Density: $1.6 \times 10^{15} \text{ m}^{-2}$
- Mobility: $118 \text{ m}^2/\text{Vs}$
- Layer structure:
 - 5 nm n -GaAs
 - 60 nm $\text{Al}_{0.35}\text{Ga}_{0.65}\text{As}$ (n-doped with Si at $\sim 1 \times 10^{18} \text{ cm}^{-3}$)
 - 45 nm $\text{Al}_{0.35}\text{Ga}_{0.65}\text{As}$
 - 649 nm GaAs

A.5 WREUT12570

This wafer was grown in the group of D. Reuter and A. D. Wieck at the Ruhr-Universität in Bochum, Germany. Devices from this wafer were used only for studies on ohmic contact formation to a 2DEG in Chapter 6 and 7.

- 2DEG Depth: 180 nm
- Density: $4.54 \times 10^{15} \text{ m}^{-2}$
- Mobility: $22.9 \text{ m}^2/\text{Vs}$
- Layer structure:
 - 5 nm n -GaAs
 - 70 nm $\text{Al}_{0.35}\text{Ga}_{0.65}\text{As}$
 - 70 nm $\text{Al}_{0.35}\text{Ga}_{0.65}\text{As}$ (n-doped with Si at $\sim 1 \times 10^{18} \text{ cm}^{-3}$)
 - 35 nm $\text{Al}_{0.35}\text{Ga}_{0.65}\text{As}$
 - 650 nm GaAs

Appendix B

Device fabrication

In this Appendix we will describe the fabrication procedure for the devices that were used in this thesis.

B.1 Alignment markers

- Preparation:
 - Clean in boiling acetone (10')
 - Rinse in IPA (30")
 - Spin dry
- Resist:
 - Spin 250 nm 950K PMMA (4% in Chlorobenzene) - 4000 rpm (50")
 - Bake at 180 °C (15')
- Exposure:
 - Beam voltage: 10 keV
 - Aperture: 10 μm
 - Working area: 200 x 200 μm
 - E-beam dose: 200 $\mu\text{C}/\text{cm}^2$
- Developing:
 - Develop in 1:3 MIBK / IPA (60")
 - Rinse in IPA (30")

- Spin dry
- Evaporation:
 - 5 nm Ti
 - 50 nm Au
- Lift-off:
 - Lift-off in acetone (several hours) / acetone spray
 - Rinse in IPA (30")
 - Spin dry

B.2 Mesa etching

- Preparation:
 - Clean in boiling acetone (10')
 - Ultrasonic rinsing for couple of minutes to remove dirt at low power (need to be careful here as high ultrasonic power can break the sample as it is very brittle).
 - Rinse in IPA (30")
 - Spin dry
 - Bake at 180 °C (15')
- Resist:
 - Spin 70 nm 950K PMMA (2% in Chlorobenzene) - 4000 rpm (50")
 - Bake at 180 °C (2 hours)
- Exposure:
 - Beam voltage: 10 keV
 - Aperture: 120 μm
 - Working area: 2000 x 2000 μm
 - E-beam dose: 150 $\mu\text{C}/\text{cm}^2$
- Developing:

- Develop in 1:3 MIBK / IPA (35’)
 - Rinse in IPA (30’)
 - Spin dry
 - Bake at 180 °C (20’)
- Etching:
 - Etch in a 1:1:50 solution of H_2SO_4 / H_2O_2 / H_2O (50’). The etching rate is approximately 2 nm/s
 - Rinse in H_2O (30’)
 - Spin dry
- Cleaning:
 - Clean in boiling acetone (10’)
 - Rinse in IPA (30’)
 - Spin dry

B.3 Ohmic contacts

- Preparation:
 - Clean in boiling acetone (10’)
 - Rinse in IPA (30’)
 - Spin dry
- Resist:
 - Spin 400 nm 50K PMMA (9% in Ethyl lactate) - 4000 rpm (50’)
 - Bake at 180 °C (15’)
 - Spin 70 nm 950K PMMA (2% in Chlorobenzene) - 4000 rpm (50’)
 - Bake at 180 °C (15’)
- Exposure:
 - Beam voltage: 10 keV
 - Aperture: 120 μm

- Working area: 2000 x 2000 μm
 - E-beam dose: 200 $\mu\text{C}/\text{cm}^2$
- Developing:
 - Develop in 1:3 MIBK / IPA (60")
 - Rinse in IPA (30")
 - Spin dry
- Evaporation:
 - 120 nm AuGe
 - 30 nm Ni
 - 20 nm Au
- Lift-off:
 - Lift-off in acetone (several hours) / acetone spray
 - Rinse in IPA (30")
 - Spin dry
- Annealing:
 - Anneal in N_2 atmosphere (50 ml/s) in the oven at 450 °C for typically 5 minutes (see *Chapter 6 and Chapter 7* for more details)

B.4 Fine gates

- Preparation:
 - Clean in boiling acetone (10')
 - Rinse in IPA (30")
 - Spin dry
- Resist:
 - Spin 70 nm 950K PMMA (2% in Chlorobenzene) - 4000 rpm (50")
 - Bake at 180 °C (15')

- Exposure:
 - Beam voltage: 30 keV
 - Aperture: 10 μm
 - Working area: 200 x 200 μm
 - E-beam dose: 450 $\mu\text{C}/\text{cm}^2$
- Developing:
 - Develop in 1:3 MIBK / IPA (35")
 - Rinse in IPA (30")
 - Spin dry
- Evaporation:
 - 5 nm Ti
 - 15 nm Au
- Lift-off:
 - Lift-off in acetone (overnight) / acetone spray
 - Rinse in IPA (30")
 - Spin dry

B.5 Large gates

- Preparation:
 - Clean in boiling acetone (10')
 - Rinse in IPA (30")
 - Spin dry
- Resist:
 - Spin 400 nm 50K PMMA (9% in Ethyl lactate) - 4000 rpm (50")
 - Bake at 180 °C (15')
 - Spin 70 nm 950K PMMA (2% in Chlorobenzene) - 4000 rpm (50")

- Bake at 180 °C (15')
- Exposure:
 - Beam voltage: 10 keV
 - Aperture: 120 μm
 - Working area: 2000 x 2000 μm
 - E-beam dose: 200 $\mu\text{C}/\text{cm}^2$
- Developing:
 - Develop in 1:3 MIBK / IPA (60")
 - Rinse in IPA (30")
 - Spin dry
- Evaporation:
 - 5 nm Ti
 - 150 nm Au
- Lift-off:
 - Lift-off in acetone (several hours) / acetone spray
 - Rinse in IPA (30")
 - Spin dry

Appendix C

Biased cool down

Applying a positive voltage to the gates, while grounding the 2DEG by the ohmic contacts during cooling down the devices (here termed biased cool down), significantly reduces the switching (telegraph) noise in the electrical measurements on QPCs. This noise is caused by the tunneling of electrons from the gates through the Schottky-barrier and getting trapped near the 2DEG layer that can then de-trap and eventually influence the effective gating in a noisy manner [3].

To achieve the best results, it is important that the applied bias is constant throughout the cooling process. The devices should also be protected against any excessive current during the bias cool-down that can damage the device. We decided to apply a bias $+0.3$ V, as this proved to be optimal in similar experiments [1, 2, 3].

The breakdown voltage of the Schottky barrier is in our case $\sim +0.5$ V at 4.2 K, but only in the range $+0.1$ to $+0.2$ V at room temperature. At room temperature there will thus be a significant leakage current for $+0.3$ V. It is important to limit this leakage current as it can permanently damage the device. This can be implemented by adding series resistance in the wires to the gates. We aimed at making sure that leakage currents were always below $5 \mu\text{A}$ per gate.

Figure C.1 shows three methods of applying the positive bias to our devices, the methods will be discussed below. We cool down the devices to 4.2 K very slowly (~ 24 hours) as slow cooling reduces noise significantly as compared to faster cool downs [4].

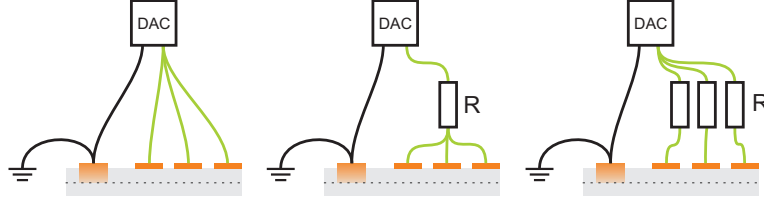


Figure C.1: Three wiring schemes for biased cool down that were considered. In all cases the voltage bias is supplied by a computer controlled DAC. Left: no protection, the bias is directly applied to the gates. Center: all the gates share a single current-limiting resistor. Right: every gate has its own current-limiting resistor.

Case one: no protection (left in Fig. C.1)

- Pros
 1. Easy to set up, especially compared to case three.
 2. Constant bias voltage is guaranteed throughout the cool down.
- Cons
 1. At higher temperatures, all the gates will leak at $+0.3$ V. Because the resistance of the Schottky barrier, even at room temperature, is around $7\text{ M}\Omega$ for a typical gate area as in our devices, the gates are not at risk. But in the case of imperfections that cause some local spots below a gate with a reduced Schottky barrier resistance, one runs the risk of destroying a gate.

Case two: One series resistor for several gates in parallel (center in Fig. C.1)

We had 36 gates per wafer piece, with one such wafer piece mounted and bonded on a single chip carrier.

- Pros
 1. Pretty easy to set up.
 2. The voltage across the device is relatively constant during cool down. In the case of an $100\text{ k}\Omega$ resistor (chosen because of its value is $\frac{1}{2}$ of 36 gates of $7\text{ M}\Omega$ each in parallel), there is an initial voltage drop of ≈ 0.2 V across the gate. This increases rapidly to the value $+0.3$ V set by the DAC source as the Schottky barrier resistance increases during cool down. Of course, the initial voltage drop can be increased by selecting a resistor of lower value, but this reduces the protection.

- Cons

1. Offers some, but no absolute protection for each individual gate. Although the current is limited by the resistor, it might still be large enough to damage one particular gate.
2. In the case of a single gate failure (break down), the voltage drop across the other gates will decrease.

Case three: One resistor per gate in series (right in Fig. C.1)

- Pros

1. When a single gate fails, the other gates are not affected.
2. Very constant bias voltage during cool down. In the case of a 100 k Ω resistor, $> 98\%$ of the voltage will drop across the gate ($\frac{100 \text{ k}\Omega}{7 \text{ M}\Omega} = 0.014 < 2\%$).

- Cons

1. Tedious to set up.
2. Offers some, but no absolute protection. Although the current is limited by the resistor, it might still be large enough to damage a particular gate.

We chose for case two applied to sets of 36 gates (and 4 of such sets controlled separately per cool down). The ease of setup was the decisive factor. We observed indeed much more quiet conductance levels in QPCs as a function of time (less telegraph noise) as compared to devices where the biased cool down was not applied.

Bibliography

- [1] M. Pioro-Ladriere *et al.*, Phys. Rev. B **101**, 226603 (2005).
- [2] A. R. Long *et al.*, Physica E: Low-dim. Sys. and Nanostruc. **34**, 553 (2006).
- [3] C. Buizert *et al.*, Phys. Rev. Lett. **72**, 115331 (2008).
- [4] Duncan R. Stewart, Ph.D. thesis, Stanford University (1999).

Summary

Electron Many-Body Effects in Quantum Point Contacts

This thesis presents experimental research into electron many-body effects that have a significant influence on the electrical current in nanoscale conductors. The electronic device that was central in this study was the Quantum Point Contact (QPC). A QPC is a short and narrow channel that provides a conducting path between two much larger conducting regions. We used QPC devices that were fabricated with very clean semiconducting materials (GaAs/AlGaAs heterostructures), and studied them at very low temperatures. Under these conditions, the distance between scatter events for electrons (the mean free path) is much larger than the dimensions of the QPC channel, such that transport in the channel is ballistic. In addition, the fact that conduction electrons in materials behave quantum mechanically and move as propagating waves is visible in the electrical conductance of a QPC. Its conductance as a function of the width of the channel shows a stepwise increase, showing that its conductance is quantized in fundamental units of $2e^2/h$ (where e the electron charge and h the Planck constant). This can be understood with theory that considers the electrons as non-interacting particles. The observation of quantized conductance shows that one is in control over electron transport, in the ultimate limit of the nanoscale and clean quantum behavior.

However, nearly all studies on such QPCs show significant deviations from pure quantized conductance. This includes the observation of the 0.7 anomaly: an additional plateau at the level of about 0.7 conductance quanta ($0.7 \times 2e^2/h$) in quantized-conductance traces. These deviations have been observed and extensively studied since the discovery of quantized conductance in 1988, but understanding is still far from complete. There is only consensus that these effects can only be understood with theory that includes interactions between the electrons. That is, the deviations result from electron many-body effects in the QPC.

Understanding these effects is important. The QPC is the most simple, clean, and most controlled device in which we can study and utilize electron transport at

the nanoscale. Hence, lack of understanding here precludes reliable understanding of more complex device structures. In addition, QPCs are the basic building blocks for a wide class of nano-engineered electronic circuits. They play a central role in several proposed devices for future information processing. Examples are devices for quantum computing and spintronic devices.

The research on many-body effects in QPCs that is presented in this thesis started with extending earlier observations from our team on a large set of QPCs with varying width and length of the transport channel. The results of this study showed that the parameters for describing the quantized conductance had a very regular dependence on the QPC geometry. The parameters for describing the many-body effects, however, showed strong fluctuations from device to device, in a random manner that lacked correlations with the device geometry. This showed that the many-body effects occur very generally, but that the parameters to describe them are exponentially sensitive to weak static fluctuations on the electrostatic potential that forms the QPC channel. These fluctuations are most likely present due to remote defects and impurities in the material, and small device-to-device variations that are inevitable in the nanofabrication process of the QPC channels. We could reproduce these results in a much larger set of devices. In addition, the new results showed for the first time signatures of many-body effects that were predicted, but up to that point not observed. In particular, the many-body effects also manifest themselves as a peak in the conductance as a function of bias voltage, near zero bias (known as Zero-Bias Anomaly, ZBA). Before, such ZBAs were commonly observed with a single peak. In our experiments, on the other hand, many devices showed ZBAs with a double peak. However, drawing definite conclusions about the underlying many-body physics was prohibited by the device-to-device fluctuations. This motivated us to develop a new type of QPC device. Conventional QPCs have a channel with tunable width, but with a fixed channel length. We successfully fabricated QPCs for which both the width and the length of the channel can be tuned *in situ*.

These length-tunable QPCs also showed clear 0.7 anomalies and ZBAs. Interestingly, the strength of the 0.7 anomaly appeared to change in a periodic fashion as a function of channel length. At the same time, the ZBAs changed their appearance from single-peak to double-peak as a function of channel length, and this had a clear correlation with the modulation of the 0.7 anomaly. Analysis of this data provides a strong indication about the many-body physics that is at play, and it can be linked to state-of-the-art theory work on this topic. The picture that emerges is that oscillations in the charge density (Friedel oscillations)

in the channel are enhanced by electron-electron interactions, which results in the formation of a single or a few localized states in the QPC channel. Each of these states contain about one electron. In turn, with such localized states near a large electron reservoir the Kondo effect will often play a role in the formation of the many-body state. The localization results in a suppression of the QPC conductance from $1 \times 2e^2/h$ down to values of about $0.7 \times 2e^2/h$. The Kondo effect, however, can restore the conductance back towards $1 \times 2e^2/h$, and the ZBAs are the fingerprint of this effect. Further analysis towards more definite conclusions is in progress at the time of this writing.

This thesis also presents results from research that aimed to improve technological aspects of operating QPC and similar devices. Specifically, the final two chapters report on investigations into so-called ohmic contacts for devices that are based on GaAs/AlGaAs material with a two-dimensional electron gas (2DEG) in a quantum well. Such a quantum well is below an insulating layer at a certain depth in these materials, and ohmic contacts are a local modification to the material that results in a well conducting path between the 2DEG and metal connection pads on the wafer surface. A widely used recipe for such ohmic contact is based on depositing a stack of thin metal layers on the wafer surface (typically a AuGe/Ni/Au sequence). In a subsequent annealing step (bringing the wafer to a few hundred degrees Celsius for a few minutes) these materials diffuse into the wafer and realize a low-resistance contact between the metal on the surface and the 2DEG below the surface, with ohmic transport characteristics. However, despite being applied for a few decades already, microscopic understanding of the mechanisms at play during the annealing step is incomplete. Such understanding is desirable for optimizing contacts with low resistance values, while they can be realized with minimal annealing times and temperatures. This is important for minimizing unwanted changes during the annealing step in other parts of a device structure. In addition, such insight can open up avenues for developing new types of ohmic contacts, as for example spin-preserving ohmic contacts that can inject spin-polarized electrons from a ferromagnetic metal into the 2DEG.

We studied ohmic contacts that were realized with a wide range of annealing parameters, and with a varying depth for the layer with the 2DEG. We studied their functioning with electrical transport measurements and the diffusion of materials into the wafer with high-resolution transmission electron microscope imaging (TEM). The results allowed for identifying the annealing mechanism and proposing a model that can predict optimal annealing parameters for a certain material. Further studies in this direction aimed to confirm and apply this model.

For this work the fabrication had to be moved to more advanced instrumentation for the annealing step. As a result of this, the ohmic contacts obtained much lower resistance values than in the initial study. While this is an interesting and useful result, the resistance values were now too low for accurate measurement of their values, which prohibited further testing of the proposed model. The results show that the annealing mechanism is also dependent on the type heating that is used for annealing (radiation versus gas flow), and that this needs to be included in a generally valid model for the annealing mechanism. The very low contact resistance values also allow for looking into the role of spreading resistance inside the contacts.

Muhammad Javaid Iqbal, Groningen, June 2012

Samenvatting

Elektron-Wisselwerking Effecten in Kwantum Puntcontacten

Dit proefschrift beschrijft experimenteel onderzoek naar elektron-wisselwerking effecten die een significante invloed hebben op de elektrische stroom in geleiders op de nanoschaal. Het elektronische device dat centraal stond in dit onderzoek was het kwantum puntcontact (QPC, Quantum Point Contact in het Engels). Een QPC is een kort en nauw geleidingskanaal tussen twee veel grotere geleidende gebieden. Onze QPC's zijn gefabriceerd met zeer zuiver halfgeleidermateriaal (GaAs/AlGaAs heterostructuren) en we hebben ze bestudeerd bij zeer lage temperaturen. Onder deze omstandigheden is de afstand waarover elektronen zich zonder botsingen verplaatsen (de zogeheten vrije weglengte) vele malen groter dan de afmetingen van het QPC kanaal, waardoor het elektronentransport ballistisch is. Bovendien is het kwantummechanische karakter van de geleidings-elektronen en het feit dat ze zich als golven voortbewegen zichtbaar in de elektrische geleiding van een QPC. De geleiding als functie van de breedte van het kanaal is gekwantiseerd en groeit stapsgewijs met stappen van $2e^2/h$ (waarbij e de elektronlading is en h de constante van Planck). Dit effect kan worden verklaard met theorieën waarin elektronen als niet-wisselwerkende deeltjes worden beschouwd. De waarneming van gekwantiseerde geleiding laat zien dat men de controle heeft over elektrontransport in de ultieme limiet van afmetingen op de nanoschaal en zuiver kwantumgedrag.

Bijna alle studies naar dergelijke QPC's laten echter significante afwijkingen van pure gekwantiseerde geleiding zien. De waarneming van de zogeheten 0.7 anomalie is hier een prominent voorbeeld van: een extra geleidingsplateau met de waarde van 0.7 geleidingskwanta ($0.7 \times 2e^2/h$) in experimenten die gekwantiseerde geleiding zichtbaar maken. Deze afwijkingen zijn waargenomen en uitgebreid bestudeerd sinds de ontdekking van gekwantiseerde geleiding in 1988, maar nog steeds is het begrip ervan verre van compleet. Het enige punt waar consensus over bestaat is dat voor een correcte uitleg de wisselwerking tussen elektronen

meegenomen dient te worden. Oftewel, de afwijkingen komen voort uit elektron-wisselwerking effecten.

Begrip van deze effecten is belangrijk. De QPC is het simpelste, schoonste en best controleerbare device waarin we elektronentransport op de nanoschaal kunnen bestuderen en toepassen. Daarom belet gebrek aan begrip op dit punt een betrouwbaar inzicht in het gedrag van complexere elektronische structuren. Bovendien zijn QPC's de bouwstenen voor een brede categorie van nanogefabriceerde elektrische circuits, en ze spelen een centrale rol in verscheidene devices die zijn voorgesteld voor toekomstige informatieverwerking. Voorbeelden zijn devices voor kwantumberekeningen en spintronica devices.

Het onderzoek naar elektron-wisselwerking effecten in QPC's voor dit promotiewerk begon met het uitbreiden van eerdere waarnemingen van ons team aan een grote set QPC's met variërende breedte en lengte van het geleidingskanaal. De resultaten van dit onderzoek toonden regelmatig gedrag voor de manier waarop gekwantiseerde geleiding afhangt van de QPC geometrie. De parameters voor het beschrijven van elektron-wisselwerking effecten lieten echter sterke willekeurige fluctuaties zien tussen devices, die geen correlatie hadden met de QPC geometrie. Dit liet zien dat elektron-wisselwerking effecten zeer algemeen optreden, maar dat de parameters die hun sterkte beschrijven extreem gevoelig zijn voor zwakke elektrostatistische fluctuaties in de potentiaal die het geleidingskanaal vormt. Deze fluctuaties treden waarschijnlijk op door kristaldefecten en onzuiverheden in het materiaal in de buurt van het QPC kanaal en kleine variaties die onvermijdelijk zijn in het fabricageproces. We konden deze resultaten reproduceren in een veel grotere set devices. Bovendien lieten de nieuwe resultaten voor het eerst sporen van elektron-wisselwerking effecten zien die wel waren voorspeld maar tot op dat moment niet waren waargenomen. Het gaat hierbij om de elektron-wisselwerking effecten die zich uiten als een piek in de geleiding als functie van de elektrische spanning over het kanaal, rond een spanning van nul volt (bekend als de Zero-Bias Anomaly, ZBA). Eerder werden dergelijke ZBA's waargenomen met een enkele piek. In onze experimenten, daarentegen, lieten veel devices een ZBA met een dubbele piek zien. De fluctuaties tussen de devices verhinderden echter om harde conclusies te trekken over de onderliggende fysica. Dit motiveerde ons om een nieuw type QPC te ontwerpen. Conventionele QPC's hebben een kanaal met een instelbare breedte, maar met een lengte die vastligt. Wij hebben met succes QPC's gefabriceerd waarin zowel de breedte als de lengte *in situ* gevarieerd kunnen worden.

Deze lengte-instelbare QPC's lieten duidelijke 0.7 anomalieën en ZBA's zien.

Interessant is dat de sterkte van de 0.7 anomalie periodiek blijkt te veranderen als functie van de lengte van het geleidingskanaal. Tegelijkertijd verandert de verschijning van de ZBA tussen enkele piek en dubbele piek als functie van kanaallengte en dit is duidelijk gecorreleerd met de periodieke variatie van de 0.7 anomalie. Analyse van deze data levert een sterke indicatie voor de elektron-wisselwerking fysica die een rol speelt en dit kan ook gerelateerd worden aan recent theoretisch werk op dit onderwerp. Het fysische beeld dat naar voren komt is dat oscillaties in de ladingsdichtheid (Friedel oscillaties) in het kanaal versterkt worden door de elektron-elektron wisselwerking en dit resulteert in de formatie van één of enkele gelokaliseerde toestanden in het QPC kanaal. Ieder van deze toestanden bevat ongeveer één elektron. Met dergelijke gelokaliseerde toestanden in de buurt van een groot elektronenreservoir is het goed mogelijk dat ook het Kondo-effect een rol speelt bij de formatie van een kwantumtoestand van vele wisselwerkende elektronen tezamen. De lokalisatie zorgt voor een onderdrukking van de QPC geleiding van $1 \times 2e^2/h$ tot waarden van ongeveer $0.7 \times 2e^2/h$. Het Kondo-effect kan de geleiding terugbrengen tot $1 \times 2e^2/h$, waarvan de ZBA's de karakteristieke manifestatie zijn. Tijdens het schrijven van dit proefschrift wordt er nog doorlopend gewerkt aan verdere analyse richting duidelijkere conclusies.

Dit proefschrift presenteert tevens resultaten van onderzoek naar het verbeteren van technologische aspecten van het controleren van QPC's en soortgelijke devices. De laatste twee hoofdstukken presenteren onderzoek naar zogeheten ohmse contacten voor devices in GaAs/AlGaAs-materialen met een tweedimensionaal elektron gas (2DEG) in een kwantum put. Deze kwantum put bevindt zich onder een isolerende laag op een zekere diepte in het materiaal en ohmse contacten zijn een plaatselijke aanpassing in deze isolerende laag waardoor een goed geleidend pad ontstaat tussen het 2DEG en metalen contacten op het oppervlak. Een veelgebruikt recept voor zulke ohmse contacten is gebaseerd op het aanbrengen van een stapeling van dunne metalen lagen op het oppervlak (typisch in de volgorde AuGe/Ni/Au). In een volgende verhittingsstap (het sample wordt een aantal minuten verhit tot een paar honderd graden Celsius) diffunderen deze materialen het substraat in, waar ze een contact met lage weerstand vormen tussen het substraattooppervlak en het 2DEG, met ohmse transporteigenschappen. Hoewel deze techniek al een paar decennia wordt toegepast, is het microscopische begrip van de verhittingsstap incompleet. Zulke kennis is gewenst om contacten met een zo laag mogelijke weerstand bij een zo laag mogelijke verhittingstijd en -temperatuur te verwezenlijken. Dit is van belang om ongewenste veranderingen elders in het device tijdens de verhitting te minimaliseren. Bovendien kan der-

gelijk inzicht mogelijkheden openen voor nieuwe varianten van ohmse contacten, bijvoorbeeld spin-behoudende ohmse contacten die spin-gepolariseerde elektronen van een ferromagneet in het 2DEG kunnen injecteren.

We hebben ohmse contacten bestudeerd die zijn gemaakt bij een grote variëteit aan verhittingsparameters en voor een variëteit aan 2DEG dieptes. We hebben hun functioneren gekarakteriseerd door middel van elektrische transportmetingen en hebben de diffusie van de materialen in het substraat bekeken met behulp van hoge-resolutie transmissie elektronenmicroscopie (TEM). Uit de resultaten kon het microscopische mechanisme achter de verhittingsstap in kaart worden gebracht en een model worden geformuleerd dat voor een materiaal voorspelt wat de optimale verhittingsparameters zijn. Verder onderzoek in deze richting had als doel dit model toe te passen en te verifiëren. Hiervoor werd de verhittingsstap met meer geavanceerde apparatuur uitgevoerd dan voorheen. Het resultaat was dat de ohmse contacten een veel lagere weerstand hadden dan bij het eerdere onderzoek. Hoewel dit een interessant resultaat is, was de weerstand nu te laag om deze precies te kunnen meten, en dit maakte het verder testen van ons model onmogelijk. De resultaten laten zien dat de aard van de verhittingsstap tevens afhankelijk is van de manier van verhitten (straling versus convectie via gas) en dat dit meegenomen moet worden in een geldig model voor de verhittingsstap. De hele lage contactweerstand gaf wel interessante mogelijkheden om de rol van verspreidingsweerstand in de contacten te onderzoeken.

Muhammad Javaid Iqbal, Groningen, juni 2012

Acknowledgements

The work presented in this thesis was carried out in the group of Physics of Nanodevices at the University of Groningen, the Netherlands, between November 2007 and November 2011. Now that I have accomplished this work, I would like to thank many people who helped me to reach this stage.

First of all I would like to acknowledge my supervisor and promotor Caspar van der Wal for his supervision and guidance throughout my PhD research work. During all the measurements, you showed special interest not only in the scientific (physics part) aspect but also technical things. Unlike many other supervisors you come to the labs to see the running experiments. I still remember the day when I was measuring on QPC to search for the double-peak ZBA in conventional quantum point contacts, you came to the lab at around 21:00 hours and you were really excited to know that I had found a QPC that showed the trend we were looking for. It was very special to me that you have been coming to the labs to discuss the circuit schemes, measurement issues and dilution fridge related problems. Many of the hands-on sessions that I had with you during my work on writing skills, presentations, plotting, physics and technical issues have been very useful for me and I will definitely profit from it in my future as well. You have not only been supportive in science but also in personal life. I learned a lot from you by observing how well organized you are. I have learned a lot while working with you and feel that I'm at much better place than four years ago. For all that I owe you a very special thanks.

I would like to thank Bart van Wees. During my talks in the group meetings, your critical observation and questioning has been a driving force for me to improve the things. Your thinking is very original and it is justified by many of your papers based on original pioneering ideas. I have learned a lot by working and observing closely how you conduct your research.

I would like to thank Tamalika Banerjee for discussions in general and particularly on career orientation. It is nice to see that your BEEM team has already started producing nice results. I wish you much more success in the years to

come. Special thank to the members of the reading committee A.D. Wieck, D.M. Zumbühl and W.G. van der Wiel for accepting this responsibility. I would also like to thank Y. Meir and R. Aguado, D. Reuter and A.D. Wieck for collaborative work. Y. Meir, it was a really fruitful discussion with you when you visited the University of Groningen in 2009. It was the discussion with you that led us to make length-tunable quantum point contacts.

When I joined the Physics of Nanodevices group in 2007, I had the opportunity to work with my predecessor E.J. Koop. I really owe you a lot of thanks for teaching me the basics of fabrication, clean room and measurement techniques. You also made sure that Bernard and me could operate the dilution fridge once you left the group. The work presented in this thesis would not have been possible without the help from our very experienced and talented group technicians (late) Siemon Bakker, Bernard Wolfs, Johan Holstein and Martijn de Roos. Bernard, I still remember when water circulation for turbo pumps failed and you was there within half an hour at midnight to fix that. Special thanks for that. Johan thanks for the help in clean room usage. Special thanks for fixing the turbo pump quickly during my measurements when my samples were cooled in the dilution fridge. Without that it would have been quite bad for my devices and measurements. Thanks to Martijn as well for all the help during long dilution fridge measurements.

I would like to thank my paranympths Aisha Aqeel and Jakko de Jong for taking on this responsibility. You both and two other students (Jasper and Jordi) worked during your student projects with me and contributed significantly to the research. In the situation where I was working alone on the project, it was really great to have you all during my long measurements. Aisha best wishes for your pursuit of a Ph.D. position of your interest. Here I would also like to thank our former and current group secretaries Sonja and Anna for their help in the paper work. Anna, I always find you on top of your job.

I would like to say thanks to my office mates (former and current), Niko, Eek, Sander Onur, Olger and Thorsten for the nice time that I spent with them during my stay. Thanks for all the discussions related to physics and non-physics issues. It was really nice to have people from the same region. Alok, Gaurav, Subir and Saurabh it was good to have you guys around. The sweets and other desi food that you have been bringing every time on your return from India has been very yummy and memory-refreshing. Thomas thanks for helping me in designing my thesis cover. Frank and Alina best wishes for finishing last bit of your Ph.D. work and then finding a new job. Niko, Ivan and Eek best

wishes for a smooth journey (although it is not always very smooth) for your carrier in academia. I would also like to thank all the other group members as I must have learnt a lot from them during their group talks and in personal communications, as well as for their support in one way or the other: Csaba, Ji Liu, Bram, Vincent, Arramel, Thomas, Paul, Magda, Joost, Fasil, Jasper, Sander Kamerbeek, Nynke, Rob, Hilbert, Eline, Rianne, Roald, Dirk, Niek, Ewout, Hiva, Siva, Zorione, Csaba, Maksym, Sergii, Marius, Jorir, Anatoliy, Morten and all the others I do not remember at this moment. Linstra and Johan thanks for constant Helium and Nitrogen supply during my experiments. Jonker thanks for your help with the measurement equipments especially with "IVVI meetkast" during my research here. For funding and organizational support, I would like to thank Higher Education Commission (HEC) Pakistan and dutch NUFFIC. I would also like to thank my former teacher and friend Atif Shahbaz for all the support and motivation that he provided over the years. Naureen it was nice to discuss physics and non-physics issues with you over the period I spent here. Best wishes for finishing your Ph.D.

For all the fun that I had playing squash and table tennis, thanks to Sulman, Afzal, Irfan, Atta, Saleem and Waqas. Cricket is one of the seasonal sport in the Netherlands that I really enjoyed playing. Although I broke my fingers couple of times while fielding but you know it is hard to leave a sport that you really love. Yousuf and Sulman thanks for your help during the injury. I owe lot of thanks to my friend Sulman for his help in rehabilitation process after the thumb surgery. I really enjoyed traveling and playing with the cricket fellows, many of them I can recall here: Sulman Shafique, Yousuf Siddique, Raj Thummer, Gopi Krishnan, Afzal Rana, Atta ur Rehman, Sanger, Suleman Khan, Gerard, Sarfraz bhai, Summon Paul, Shiva, Sunil Manden, Naveen Manden, Yash Pal, Savneet and many others I can not recall at the time of writing this piece. Best wishes for all the HEC fellows here in Groningen for finishing their PhD and finding new jobs: Sulman, Atta, Bilal, Ali, Ijaz, Ehsan, Zia, Afzal, Rashid, Rana Irfan, Rana Afzal, Umer, Omer, Shafiq, Irfan, Tanveer, Ghufrana, Nazia and Nadia.

At the last but not least I would like to acknowledge the support of my family back in Pakistan. Their prayers, best wishes and all the unconditional support that they provided me in all sort of circumstances have helped me to move forward. And yes Abu g (my dear father) you are not here to see me at this occasion but I have fulfilled my last promise that I made... I know you would have been the happiest person to see me graduating... All I can do just remember the good days and memories! This thesis is dedicated to you!

Curriculum vitae

Muhammad Javaid Iqbal

- 1 Jan. 1982 Born in Punjab, Pakistan.
- 1992-1997 High school, Narowal, Pakistan.
- 1997-2000 F.Sc. at Science College, Lahore, Pakistan.
- 2000-2002 B.Sc. in Physics and Mathematics at Punjab University,
Lahore, Pakistan.
- 2002-2006 M.Sc. in Physics at G. C. University
and Punjab University, Lahore, Pakistan.
- 2007-2012 Ph.D. research at the Zernike Institute for Advanced Materials,
University of Groningen, The Netherlands
under the supervision of prof. dr. ir. C. H. van der Wal.
Subject: Electron Many-body Effects in Quantum Point Contacts.

List of publications

1. *Signatures of self-consistent two-impurity localized states in quantum point contacts*
M. J. Iqbal, E. J. Koop, D. Reuter, A. D. Wieck and C. H. van der Wal
In preparation for Phys. Rev. B.
2. *Emergent impurity states from many-body physics in clean quantum point contacts*
M. J. Iqbal, E. J. Koop, J. B. Dekker, J. H. M. van der Velde, J. P. de Jong, D. Reuter, A. D. Wieck, R. Aguado, Y. Meir and C. H. van der Wal
In preparation for Science.
3. *Split-gate quantum point contacts with tunable channel length*
M. J. Iqbal, J. P. de Jong, D. Reuter, A. D. Wieck and C. H. van der Wal,
Submitted to J. Appl. Phys.
4. *The annealing mechanism of AuGe/Ni/Au ohmic contacts to a two-dimensional electron gas in GaAs/AlGaAs heterostructures*
E. J. Koop, M. J. Iqbal, F. Limbach, M. Boute, B. J. van Wees, D. Reuter, A. D. Wieck, B. J. Kooi, and C. H. van der Wal,
Submitted to Sem. Sci. Tech.
5. *Robust recipe for low-resistance ohmic contacts to a two-dimensional electron gas in a GaAs/AlGaAs heterostructure*
M. J. Iqbal, D. Reuter, A. D. Wieck and C. H. van der Wal,
In preparation.